1991

Modelling weld microstructure development in resistance welded crossed bars.

Rong. Pan
University of Windsor

NOTICE

The quality of this microform is heavily dependent upon the quality of the original thesis submitted for microfilming. Every effort has been made to ensure the highest quality of reproduction possible.

If pages are missing, contact the university which granted the degree.

Some pages may have indistinct print especially if the original pages were typed with a poor typewriter ribbon or if the university sent us an inferior photocopy.

Reproduction in full or in part of this microform is governed by the Canadian Copyright Act, R.S.C. 1970, c. C-30, and subsequent amendments.

AVIS

La qualité de cette microforme dépend grandement de la qualité de la thèse soumise au microfilmage. Nous avons tout fait pour assurer une qualité supérieure de reproduction.

S'il manque des pages, veuillez communiquer avec l'université qui a conféré le grade.

La qualité d'impression de certaines pages peut laisser à désirer, surtout si les pages originales ont été dactylographiées à l'aide d'un ruban usé ou si l'université nous a fait parvenir une photocopie de qualité inférieure.

La reproduction, même partielle, de cette microforme est soumise à la Loi canadienne sur le droit d'auteur, SRC 1970, c. C-30, et ses amendements subséquents.

MODELLING WELD MICROSTRUCTURE DEVELOPMENT IN RESISTANCE WELDED CROSSED BARS

By
Rong Pan

A thesis
Submitted to the Faculty of Graduate Studies and Research
Through the Engineering Materials Program in the
Department of Mechanical Engineering
In Partial Fulfilment of the Requirements for
the Degree of Master of Applied Science
in Engineering Materials at the
University of Windsor

Windsor, Ontario, Canada
October, 1991

ISBN 0-315-72794-2

ABSTRACT

In the present work, a two dimensional numerical model was established for resistance welded crossed bars which include a heat-affected zone. A post-weld heating algorithm was developed to predict the thermal history of the heat-affected zone during the cooling stage. The heat diffusion equation was solved using an explicit finite-difference method. Temperature dependent thermal conductivity, heat capacities, and electrical resistivity were considered. An empirical grain growth equation was derived from Jominy test to predict the initial temperature contour in the heat-affected zone at the end of welding current input. An algorithm based on the hardenability work of Kirkaldy and coworkers has been modified to fit the resistance welded high carbon plain carbon steel bars. Isothermal transformation diagrams were also computed. Using the time-temperature history at each node in the weld region, and the modified kinetics algorithm, the rate and extent of the decomposition of austenite into its daughter products ferrite, pearlite, bainite and martensite in the welded bars were calculated. The austenite grain size incorporated into the modified kinetics algorithm changed with the position in the heat-affected zone. Experimental observation of microstructures in the welded bars was carried out. The algorithm was found to be in agreement with experimental results.

ACKNOWLEDGEMENT

The author wishes to express her sincere gratitude to Dr. D. F. Watt for his invaluable guidance, supervision and suggestions as well as his encouragements throughout all parts of this project.

She would like to express her thanks to Coschell Inc. for the help of experiment works, and faculty technician Mr. J. Robinson for his technical advice and aid.

She would also like to express her special thanks to her parents for their encouragement and confidence throughout her education.

TABLE OF CONTENTS

TABLES

FIGURES

CHAPTER I

INTRODUCTION

1.1. Aspects of Resistance Welding

1.1.1. The Resistance Welding Process

Resistance welding is where very high electric currents are passed through the two parts to be welded. Since the largest resistance is at the interface between the two parts, the greatest heat (I^2R) is produced at this interface. This causes the interface to melt, and as the liquid is expelled, the two parts sink into each other. When the current is stopped, the colder base metal rapidly cools the material, and a solid weld is formed. The currents are extremely high, with current densities of 10^5 amps/cm^2 order of magnitude being typical. These currents are applied for only a short duration, commonly from a fraction of a second to as long as a few seconds, depending on the welding process. Pressure is applied by the welding machine through the electrodes at some stage in the operation, so as to ensure close contact of the parts at the weld. This electrode force is supplied either by air or oil pressure through cylinders, or mechanically by cams. The force is often great enough to cause some deformation in the hot metal next to interface, increasing the interpenetration at the two parts.

1.1.2. Resistance welding machine

All types of resistance-welding machines have the three following fundamental

components in common:[1-1]

i. A mechanical system in which the work pieces are held and the electrode or platen force is applied.

ii. An electrical circuit which consists of a transformer, a means for regulating current and a secondary circuit to conduct the welding current.

iii. A control system which may be a simple weld timing device or a combination of mechanical action sequencing and weld timing devices, or the digitally controlled SCR high current switches..

These three components regulate the three principal variables in resistance welding, namely, force, current and the time of current flow.

1.1.3. Welding cycles

General speaking, a complete welding cycle in resistance welding is composed of the preheating cycle, the heat input (welding current) and the post-heating cycle[1-2]. The application of supplementary heat is intended to lower the cooling rate after welding so that the mechanical properties of a weld can be improved.

In making a weld, the pieces of material to be joined are held between two water chilled copper electrodes. The current is passed from one electrode through the base metal to the other electrode[1-1]. During passage, the current encounters seven separate resistance zones as shown Fig. [1-1]. The workpiece itself is the high resistance element of the welding circuit. The greater heating effects can be found at the surfaces of the work pieces because of contact resistance. Since two contacting surfaces do not facilitate the flow of current as efficiently as a solid member, the electrical resistance at this

interface will be higher. The heat is constrained about the welding centerline (or faying surface) by both the water chilled electrodes and the relatively high faying surface resistance. The thermal changes encountered by the metal during the welding process are usually sufficient to result in melting along the faying surface and cause metallurgical changes to the microstructure of the weld nugget.

1.1.4. Resistance Welded Wire Meshes

In the present work, the welding process was carried out at Coschell Inc. of Niagara Falls, New York. The standard welding cycle used by Coschell Inc. in resistance welding is shown in Fig. [1-2]. The material used by Coschell Inc. in resistance welding is a high carbon plain carbon steel rod, 15.3 mm (0.625 inch) in diameter. The rods are first cut to a certain length. Then, they are welded in perpendicularly to each other (Fig.[1-3]) by high amperage and low voltage current in a special resistance welding machine to form wire mesh as shown in Fig. [1-3] and Fig.[1-4]. The welding machine Coschell built is to utilize a patent which they hold for this process. The machine functions are controlled by computer programs. The control system and power supply used in the weld by machine are state-of-the art for high current welding. The size of rods and the mesh spacing can be adjusted flexibly according to the purpose of the application. The extent to which fusion takes place in the pieces being in joined will vary with the welding cycle (Fig.[1-4]). Different processes impose a wide range of conditions of temperature, time and pressure upon the metal.

1.2. Historical Review

Resistance welding has been with us for over a hundred years. As early as 1857[1-3],

James Prescott Joule demonstrated the possibility of producing metal joints by means of resistance heating. But it was another twenty years before Elihu Thompson carried out, in 1877, the successful experiments that led later on to the development of resistance welding. It was the Russian scientist Nikolaievich Benardos who developed the idea of joining iron plates by means of resistance welding. Two patents were granted tc him, in 1887 and 1888 for resistance spot welding using carbon electrodes. Approximately ten years later, Kleinschmidt improved the technique decisively by substituting copper electrodes for the carbon ones used up till then.[1-3]

1.3. Metallurgical Phenomena in Resistance Welding

In resistance welding, the quality of a weld is mainly controlled by the final microstructures in the Heat-Affected Zone (HAZ). The HAZ, which forms adjacent to the weld puddle within the metal, is a region where the welding process employed has not created a temperature high enough to produce molten material but the temperature has been raised to a magnitude which is sufficient to cause metallurgical changes as shown in Fig.[1-5], typically in a zone 1 mm to 1 cm wide. In arc welded steels, the molten weld puddles are much larger and the cooling times are much longer than in resistance welds. The HAZ is comprised of a number of sub-zones (depending on the material being welded): (a) the fusion zone; (b) the coarse grained zone, immediately adjacent to the fusion zone where the temperature reached is high enough to allow the formation of the large austenite grains; (c) the fine grained zone; (d) the partially transformed zone and zone of spheroidized carbides; (e) the unchanged base metal zone.[1-4]

During the welding process, the HAZ will suffer a series of complex metallurgical transformations. On heating, sufficiently high local temperatures (Peak temperature above A_{e3}) are attained to fully austenitize much of the base metal. On cooling, austenitized metal will experience a decomposition into any of a series of its daughter products: ferrite, pearlite, bainite and martensite. Each sub-zone undergoes a different thermal history depending on the local temperature reached and its position in the HAZ. Therefore, each sub-zone has a different type of microstructure and, perhaps more importantly, each structure type is likely to posses different mechanical properties.[1-4]

It is in the HAZ that the most common weld failures are initiated and propagate. These failures are often related directly to the microstructure. The cracks are most often initiated and propagate in the least reliable area of the weld, the coarse-grained region, where the larger grain size increases the susceptibility to cracking[1,5,6]. The most likely weld fracture is due to the brittle nature of the microstructure, martensite, formed by a rapid cooling rate. The structure type, its sub-zone width and the desired properties of the welded metal are mainly determined by the welding thermal cycle and steel composition. Thus, in order to obtain a reasonable understanding of the HAZ, it is necessary to consider how the microstructures of the base metal react to the complete thermal cycle and its effect on phase transformations. It is desirable to avoid, to the extent possible, the formation of martensite.

1.4. Objective of Present Work

The complexity of the local time-temperature histories, and the general nonlinearity of the kinetics of the metallurgical reactions makes an analytical prediction of HAZ

microstructures intractable. It is, however, an interesting challenge for numerical modelling. The main purpose of this work is to develop a computer program using numerical method for a post-weld heating schedule to accurately simulate the cooling time-temperature history of the weld zone and its environs, and to predict the extent of, and microstructure formed in, the HAZ of a welded steel crossed bars for a range of steel chemical composition, as a function of the weld process input parameters. Consequently, a desirable post-weld heating schedule applied for resistance welding can be forecasted by examining the modelling results.

In this work, the finite difference method has been adapted to develop the algorithm for two-dimensional conductive heat transfer in post-weld heating calculations. Combined with an algorithm for the decomposition of austenite into its daughter phases, the algorithm can be used to simulate the temperature histories and model the development of microstructures as a function of temperature. It is known that the type and volume fraction of transformation product in a welding process depends on several factors, including austenite grain size, peak temperature, cooling rate, and alloying elements present. In order to map the microstructure development as a function of the temperature in the HAZ , the temperature distribution in the HAZ at the end of the weld cycle in resistance welding must be determined. But in fact, it is very difficult to obtain an exact temperature distribution because of the very short period of heat input. Therefore, an empirical grain growth equation as a function of austenizing temperature, based on the experimental results of Jominy tests, has been developed. Compared with the austenite grain size obtained from the HAZ of the actual weld, a corresponding

temperature distribution at the end of welding part of the cycle can be estimated by using this empirical grain growth equation.

On the other hand, the high carbon equivalent of the base metal in this case increases the risk of forming martensite and the propensity to crack. The difficult part of alleviating the problem of martensite formation and cracking in resistance welding is to know how much post-weld heating current is required (Fig.[1-2]), and for what period of time it should be applied to coax the weld bead into forming a normalized, rather than a quenched microstructure. To implement the program, we are attempting essentially to use the computer to overlay the cooling curves to be experienced by the weld bead onto the Continuous Cooling Transformations (CCT) diagram appropriate for the steel being welded. To do this, it is necessary to develop a algorithm based on Kirkaldy's theory[1-7] to model the Isothermal Transformation (IT) Diagraim for a given steel. Then, the algorithm is used to predict the cooling rate in the actual resistance welding process, and combine this with the metallurgical part of the algorithm to determine the welding cycle. If the cooling rate of the weld can be slowed down at a controlled rate, it should be possible to reduce the formation of martensite greatly and thereby obtain a product which yields the desired properties. To estimate the accuracy of the modelling results, the computed results of microstructure predicted in the HAZ based upon these models are compared with experimentally obtained ones for the actual case of resistance welding done at Coschell Inc. Thus, the whole algorithm is composed of the modelling of the heat transfer history, isothermal transformation diagrams, and the metallurgical reactions.

CHAPTER 2

LITERATURE REVIEW

2.1. Weldable Metals[2-1]

In a resistance welding process, the weldability of a metal is determined by three physical properties: (1) electrical resistivity, (2) thermal conductivity, and (3) melting temperature. A formula[2-1] combining these three properties for weldability W and which provides an indication of the ease of welding a metal is:

$$W = \frac{R}{FK} \times 100 \qquad (1)$$

with R resistivity, F melting temperature of the metal in °C, and K relative thermal conductivity with copper equal to 1.00. If W is below 0.25, weldability is poor. For W between 0.25 and 0.75, weldability is fair. Between 0.75 and 2.0, weldability is good. Above 2.0 weldability is excellent. A metal with a high resistance to current flow, a low thermal conductivity, and a relatively low melting temperature is easily weldable. Ferrous metals all fall into this category. Metals that have a lower resistivity but a higher thermal conductivity will be more difficult to weld.

2.2. Numerical Methods in Modelling Welding Process

2.2.1. Numerical Analysis in Welding

During the past few years there has been a tremendous growth in research efforts

aimed at the mathematical modelling of welding processes to understand the heat transfer during welding. Geometric shape, microstructures, thermal stresses, heat losses, and material properties all significantly affect the weld quality and productivity. Essentially, two approaches have been used to analyze the heat flow in welding. The first method consists of obtaining closed form solutions of the governing partial differential equations, while the second approach employs numerical methods such as finite difference, or finite element techniques.[2-2]

The governing partial differential equation for the quasi-stationary temperature distribution around either a moving point or a line heat source in the arc weld problems was first proposed by Rosenthal.[2-3, 4] In spite of recent progress in computer technology and numerical methods, it appears that the classical models by Rosenthal are still highly competitive by virtue of their analytical nature and are therefore frequently used in the modelling of arc welding process[2-5-9]. However, in many real weld situations, the assumption of thin plate or thick plate heat flow inherent in the Rosenthal equation is not always met because of variable temperature gradients in the through-thickness direction of the plate[2-9].

Following the classical analysis of temperature variations by Rosenthal, a number of studies[2-(10-15)] in arc welding by finite difference or finite element methods have added realistic effects such as temperature dependent fluid properties and radiative and convective boundary conditions on the workpiece surface so that the temperature histories, geometry of a weld shape and microstructure development can be evaluated numerically. Also, instead of the idealized point and line source variation, closer

approximations to the heat input, including Gaussian and more complex profiles have been examined.[2-10-14]

A survey of the literature on resistance welding (Refs 2-15-24) reveals that most of the thermal models for the heat transfer phenomenon in resistance spot welding process can be solved by using two or three dimensional finite difference or finite element techniques, or these can be combined with other numerical methods such as the successive overrelaxation method[2-20]. In these models, an axisymmetric distribution of temperature through the thickness and along the interface where the two sheet pieces meet is supposed. The current density is assumed to be uniform within the sheet, and the maximum heat is generated in the contact area of the workpieces. Consequently, all of these models are available to predict the temperature and voltage distributions during the nugget formation in the resistance spot welding process, incorporating the thermoelectric interaction at the interface in the weldment and the nugget growth[2-17-21]. Han et al.[2-22] models the temperature distribution using an explicit finite difference method, in which a cylindrical coordinate system was selected with radial as well as vertical variations in temperature. One important feature of the model is that it accounted for the temperature dependence of the physical properties of the base metal. They obtain very good simulation results for temperature distribution, which is in excellent agreement with that measured from actual welds.

The resistance welding process in Coschell Inc. has some similarity with spot resistance welding but there are also differences from the spot welding process. The heat-affected zone and nugget at the Coschell resistance welding is much larger than that

of spot welding. As well, the geometric shape of the HAZ in resistance welding is elliptic as shown in Fig.[1-5], and is a function of welding current and electrode force. Thus, the geometry is more complex than that in the spot welding. So far, none of extant literature is immediately applicable to our resistance welding process, which is not surprising in view of the unique nature of the welding machine.

2.2.2. Finite-Difference Analysis of Heat Transfer

The finite-difference method is an important and practical numerical analysis technique that allows the determination of approximate values of the desired numerical solution for many engineering problems. Also, its generality and relative simplicity make it easy to adapt to computer programming.[2-25-27]

Applying this method to the heat transfer phenomenon, a numerical solution enables the determination of the temperature at discrete points only. The essence of the method involves substitution, for the differential operators in the initial differential equations, of approximate values expressed in terms of differences of the functions at discrete points of the differencing grid.[2-25].

The first step in this method is to subdivide the medium of interest into a number of small regions and assign to each region a reference point at its centre.[2-26]. The reference point is frequently termed a nodal point, and the aggregate of points is termed a nodal network or mesh. It is important to note that each node represents its defined region, and its temperature is a measure of the average temperature of the region. The selection of nodal points is arbitrary, and depends on material properties, geometric convenience and the accuracy desired.

The numerical accuracy of calculation depends strongly on the number of designated nodal points for the selected region.[2-26]. The choice of the grid should satisfy the stability criteria which prevents temperature oscillation and gives a stable solution for finite-difference analysis. The stability criteria requires the choice of an appropriate Fourier number. The determination of Fourier number in finite-difference method is based on the criteria given below

$$F_{o_{1-D}} = \frac{\alpha \Delta t}{\Delta x^2} \leq \frac{1}{2}$$
$$F_{o_{2-D}} = \frac{\alpha \Delta t}{\Delta x^2} \leq \frac{1}{4} \qquad (2)$$

where F_o is the Fourier number for one dimensional or two dimensional grids respectively, α is the thermal diffusivity of the material, Δt is the time step size and Δx is the internodal spacing. At a given Fourier number, both the grid spacing and time step size are adjustable. Certainly, to obtain greater accuracy in numerical calculations, a small mesh spacing is preferable but the computation time will increase.

2.3. Kinetics of Metallurgical Transformations in welding

In welding processes, a complicated metallurgical process is involved which affects the quality of the welded metal. This will be discussed further in the remainder of this chapter.

2.3.1. Phase Transformations in Welding

2.3.1.1. On heating

As mentioned before, when weld metal experiences a current input in a resistance

welding process, the weld metal will undergo complex metallurgical transformations. On heating, it will fully austenize in a very short time once the temperature is over A_{c1}, above which the austenite is stable. Like any metal composed of a solid solution, austenite exists in the form of polyhedral grains. In microstructure composed of ferrite and sphereoidized cementite phases, austenite nucleates first at the interface between the carbide and the ferrite[2-27-30]. The cementite particles are enveloped by austenite[2-28], and subsequent austenite formation depends on carbon diffusion through the austenite as the carbides dissolve. The mechanism of austenite formation appears to be volume diffusion controlled[2-27]. In any type of cementite-ferrite aggregate, the growth of austenite consists in the conversion of the aggregate to the γ phase at the interface of the growing austenite nodule. The nucleation rate increases with the increase in the ferrite-cementite interfacial area. It would be expected that the growth rate would be greater the smaller the distance between the carbide particles or the smaller the interlamellar spacing in pearlite[2-28]. In any case, the transformation to austenite is very fast, generally less than one second.[2-31]

2.3.1.2. On cooling

On cooling, however, the austenitized areas that lie in the HAZ undergo a diffusional decomposition reaction from austenite into a series of its daughter products as the temperature decreases below A_{e3}. The cooling path and critical temperature[2-32] are represented by the line path drawn on the Fe/C phase diagram in Fig.[2-1a]. The corresponding thermal cycle is shown in Fig.[2-1b][2-32]. On slow cooling the ferrite forms in region 5 and continues into the pearlite start formation temperature. Ferrite,

containing a small amount of carbon in solid solution, develops by nucleation at austenite grain boundaries and growth into the austenite grains. The growth rate is controlled by long-range diffusion of carbon. The morphology of the proeutectoid ferrite can be generally categorized as either platelike or chunky[2-33].

Pearlite forms in region 6 until the bainite start temperature (region 7) is reached. Pearlite is composed of a laminated eutectoid mixture of ferrite and cementite. The first stage in the formation of pearlite is the nucleation of either cementite or ferrite on an austenite grain boundary[2-34]. The nucleation rate strongly depends on the undercooling rate below the critical temperature A_{e1}. The rate of diffusion of carbon plays an important role in determining the growth rate and growth morphology. Pearlite nodules nucleate at grain boundaries and grow into one or both austenite grains at a roughly constant radial velocity, thus forming spheres or hemispheres on the boundary[2-35,36].

Bainite nucleation essentially occurs at pearlite sites and, therefore, the pearlite appears as bainite with respect to the development of the algorithm for the reaction kinetics governing the transformation[2-37-40]. Bainite formation continues until the martensite start temperature (point 8) where it is assumed that all remaining austenite decomposes to martensite. The transformation and structure of bainite are similar to both pearlite at higher temperatures and martensite at lower temperatures. Like pearlite, bainite is a mixture of a non-lamellar aggregates of roughly lath-or plate-shape ferrite grains with carbide precipitated either within the ferrite or formed directly from austenite in the inter-lath regions. The difference between the pearlite and bainite lies in their crystallography. In the case of pearlite the cementite and ferrite have no specific

orientation relationship to the austenite grain in which they are growing, whereas the cementite and ferrite in bainite do have an orientation relationship with the grain in which they are growing. Rapid cooling depresses the temperature at which the γ to α transformation takes place.[2-37] As the transformation temperature falls the distance over which carbon atoms can diffuse is reduced, and there is a tendency to form structures involving progressively shorter movements of atoms. Thus, the well delineated lamellar pearlitic layers degenerated into the feather, upper bainite forms, and at lower temperature into the fine closely spaced islands of carbide in ferrites which define lower bainite. The mechanism of bainite formation involves shear as well as diffusion[2-39].

At even lower temperatures (Ms), the diffusional transformations are completely suppressed. Here only martensite is formed by a shear movement of the austenite lattice, the carbon being retained without diffusion in a solid solution of a distorted body-centred cubic lattice.[2-28]

Generally speaking, the higher the carbon content, the lower the transformation temperature, and the harder and more brittle is the transformation product.

2.3.2. Isothermal Transformation Diagrams

2.3.2.1. What are IT Diagrams?

Diagrams that define the transformation of austenite as a function of time at constant temperature are referred to as isothermal transformation (IT) diagrams or time-temperature-transformation (TTT) diagrams as shown in fig.[2-2]. Davenport and Bain first introduced the isothermal transformation approach, and showed that by studying the reaction isothermally at a series of temperatures below the A_{e1}, characteristic IT curves

can be obtained for each particular steel.[2-41]

In their simplest form, the IT curves have a well-defined 'C' shape. The curves defining the isothermal hold times for the beginning and end of pearlite or bainite formation are the major feature of the diagram. They are indicated by Ps, Pf and Bs, Bf lines.[2-42] Only pearlite forms above the nose of the IT diagram, and only bainite forms below the nose.

2.3.2.2. Relationship between Kinetics and IT Diagram

The IT diagram indicates that the kinetical driving force can be represented by the undercooling force[2-42]—ΔT, (the difference between A_{c1} and the isothermal hold temperature). At small undercooling ΔT, the driving force for the transformation is small and the time required to start and finish the decomposition is very long. As ΔT is increased, the driving force also increases for nucleation. Using Kirkaldy equations (Chapter 5), the growth rates of the pearlite will also increase, so that the time to start and finish the transformation decreases, until the maximum rate is reached at the nose of the C-curve with a minimum time for transformation to start and to finish, which is roughly at 550 °C. Below this temperature, the driving force for the reaction continues to increase, but the reaction is impeded by the sluggishness of the diffusion of the rate controlling element, which in plain carbon steels will be carbon.

Given a cooling rate with longer holding times in the diffusional transformation temperature range, more of the austenite will transform to ferrite, pearlite or bainite, and the less of austenite will be left to quench to martensite as the weld cools to room temperature[2-28].

2.3.3. Effect of Alloying Elements on Phase Transformation

The primary purpose of adding alloying elements to steel is to delay the time required for austenite decomposition into ferrite and pearlite. The alloying elements can be classified as ferrite formers (e.g., Cr, Mo, Si) or as austenite formers (e.g., Mn, Ni, Cu).[2-43] Austenite formers can depress the A_{e1} temperature, while ferrite formers raise it.[2-44] All of these elements are substitutionally dissolved in the austenite and ferrite. Most of them have a profound effect on the rate of nucleation and growth of pearlite and bainite.

In its simplest form, the effect of alloying elements on the growth kinetics is explained as follows.[2-45] Initially the alloying elements are homogeneously distributed throughout the austenite. However, if equilibrium is attained after the transformation, any given alloying element will have a higher concentration in either the carbide or ferrite phase. The partitioning of these substitutional alloying elements requires long-range diffusion. The substitutional elements diffuse slowly at the transformation temperatures. If the alloying elements remain uniformly distributed in the pearlite after the transformation, the ferrite-carbide mixture is not in its lowest-free-energy, partitioned state, but is metastable. If the austenite were to decompose to ferrite plus carbide in which the alloying element has its equilibrium inhomogeneous distribution, the bulk free energy ΔG_v is larger but the transformation can proceed only as fast as the substitutional alloying elements diffuse. If the austenite were to decompose to ferrite plus carbide in which the alloying element has its metastable, homogeneous distribution, the free energy available to drive the transformation is markedly reduced. Thus, the reaction is slowed

down by the addition of alloying elements, whichever reaction mechanism is followed. For example, the presence of manganese lowers the $A_{c3} \rightarrow A_{c1}$ critical range and makes the transformation of austenite very sluggish, by a solute-drag effect on the moving γ/α interface.[2-43]

2.3.4. Modelling of IT Diagrams

The classical models to describe the nucleation and growth transformation process were presented by Avrami[2-46], Johnson and Mehl.[2-47]

In the Avrami[2-46] model, a mathematical expression to describe a sigmoidal-shaped, isothermal transformation-time event is given as:

$$X = 1 - \exp(-bt^n) \qquad (3)$$

where X is the fraction transformed, b and n are constants, determined from isothermal-transformation "start" and "end" curves, and t is the duration of transformation (i.e., the time). The sigmoidal shape is considered to reflect the relative effects of a combined nucleation and growth transformation process as are characteristics of the austenite-to-pearlite transformation in eutectoid steels.

Later, Kirkaldy et al.[2-48-50] developed a reasonably accurate metallurgical kinetics algorithm based on rigorous thermodynamics and approximate isothermal phase transformation kinetic equations for ferrite, pearlite and bainite. The algorithm can be used to predict the IT diagrams, microstructure and hardenability of most hardenability steels. The algorithm has a general Avrami type form;

$$\frac{dX}{dt} = B(G,T,X)\,X^m(1-X)^p \qquad (4)$$

The IT diagram is then given by

$$\tau(X,T) = \int_0^X \frac{dX}{B(G,T,X)\,X^m(1-X)^p} \qquad (5)$$

where X is the volume fraction of daughter product, B is an effective rate coefficient, G is the austenite grain size, and m and p are semiempirical coefficients set to less than one to assure convergence in a form that is derived from a point nucleation and impingement growth model.[2-51] The rate coefficient includes the effect of grain size on the density of eligible nucleation site. It also includes the amount of austenite supercooling, and the effect of alloying element and temperature on diffusion. It[2-49] assumes from thermodynamics that the effective eutectoid temperature is a function of composition, and from nucleation theory that the incubation time (TTT start curves) is a function of undercooling and composition. The model can give a good semiempirical prediction of concentration-dependent TTT curves, and of pearlite growth velocity as a function of composition and temperature for low alloy steels. The Kirkaldy model does not have a separate nucleation stage. It is a growth rate function based on equation [4].

Bhadeshia[2-52] also proposed a model based on thermodynamic method and Russell[2-53,54] theory to predict the IT diagrams for low alloy steels. It assumes the applicability of classical nucleation theory, and neglects strain energy. The incubation periods τ_s for a variety of grain boundary nucleation situations are calculated as a function of temperature, volume free energy, and diffusion coefficient and chemical

composition. The method[2-52] involves the calculation of two separate "C" curves, one representing diffusional polygonal ferrite and pearlite transformation, and the other representing the displacive the Widmanstätten ferrite and bainite reactions transformations respectively. The position of the curves in the time/temperature domain is determined using a semi-empirical thermodynamic approach capable of taking account of C, Mn, Si, Cr, Mo, Ni, in any combination for a low-alloy steel. However, the model does not allow for austenite grain size variations which will affect the accuracy of modelling results because the larger austenite grain size does have a significant effect on transformation time. It will shift the IT curves to a longer reaction time.

2.3.5. Modelling Microstructure Development in Welds

Generally speaking, the final properties of a weld are determined by the microstructures present in the HAZ. Microstructure modelling overlaps the difficult subjects of welding and phase transformation theory. The purpose of microstructure modelling is to obtain a reasonable estimate of the influence of variables such as chemical composition, welding parameters, and thermal history on the weld metal characteristics.

Although considerable effort has been put into numerical modelling of the welding process as we mentioned before, the main focus has been on the size and shape of the weld puddle, and on thermal history of the weldment and its environs. Publications coupled to reaction kinetic theories to predict microstructural development of the HAZ are relatively limited. To date, the models developed have only dealt with arc welding processes.

In the early 1980's, Ashby and Easterling[2-55,56] developed a theoretical model of fusion welding. and were able to predict the temperature distribution and the microstructural changes in the HAZ of the fusion weld. The phenomena included in the model during heating and cooling of the weld thermal cycle are dissolution and coarsening of carbonitrides, phase transformation and grain growth. In this model[2-56], the temperature distribution near the weld is assumed to obey a modified version of the analytical Rosenthal equation[2-3,4], and a simplified kinetic equation is used to calculate the austenite grain growth. Approximate transformation rates for ferrite, pearlite, bainite and martensite are calculated using the carbon equivalent index. The calculation relies heavily on experimental data gathered from a wide range of steels, to which empirical equations have been fitted and combined with classic phase growth theory. The modelling results are presented as microstructural HAZ diagrams with axes of cooling time from 800 to 500°C, Δt (which measures the time constant of the weld process and is related to the energy input of the weld), and T_p, peak temperature reached at a given point in the HAZ. In the diagram, the austenite grain size and the amount of martensite formed can be read directly off a map in cooling time-T_p space. The diagrams give a tolerably good description of the microstructural and property change occurring in the HAZ during welding.

Watt and Coon[2-57,58] have also established a model based on the hardenability algorithms developed by Kirkaldy et al.[2-48,-50] to forecast the transient microstructural changes in the HAZ of arc welding. The algorithm[2-30] can be used to isolate the individual effects of weld process parameters or of metallurgical kinetic factors. In

particular, they were able to use their algorithm to highlight the profound effect that austenite grain size has on the HAZ microstructure. In this model, a starting size and shape of molten weld puddle is assumed. Using standard heat transfer equations, the time-temperature history at each node is calculated by an explicit finite difference method. According to thermal history and kinetic algorithm by Kirkaldy[2-48], the rate and extent of the decomposition of austenite into its daughter products; ferrite, pearlite, bainite, and martensite can be estimated. The general applicability of the model[2-58] is limited because of the use of a rather restrictive one-dimensional finite difference heat transfer algorithm. However, the model[2-57,58] has been coupled to the FEM heat transfer models established by Goldak[2-32] to predict HAZ microstructure changes in arc welding for a low alloy steel. The system is supported by comparing microstructure computations to some of the HAZ experimental measurements for a low carbon microalloy structural steel. They obtained good agreement with experiment data.

Bhadeshia[2-59] proposed another approach to model microstructure for low-alloy steel in arc welding. This model is constructed in terms of adaptations of phase transformation theory, combined with experimental information obtained from a systematic series of low-alloy steel deposits and is capable of predicting approximately the microstructure of the fusion zone of low-alloy steel weld deposits. The model[2-59] requires an input of austenite grain size, chemical composition and the cooling curve of the fusion zone. Allotriomorphic ferrite growth is assumed to occur by a para-equilibrium transformation mechanism. Its formation is found to determine the volume fraction development of both Widmanstätten and acicular ferrite. The theory is found

to be in good agreement with experimental results.

In the above algorithms of modelling microstructure development, the austenite grain size is assumed a constant. In our resistance welding investigation, we find that it will be more reasonable to assume the austenite grain size is a function of temperature and position from the fusion line in the HAZ. Therefore, in the present work, one of the purposes is to model the microstructural changes in the heat-affected zone by using a map of varying austenite grain size as one of the inputs in resistance welding.

2.4. Grain Growth

2.4.1. Grain growth in Welding

Grain growth is the process by which the mean grain size of an aggregate of crystals increases. The driving force for this results from the decrease in free energy which accompanies reduction in total grain boundary area.[2-60]

In the welding process, when a weld experiences a weld thermal cycle, rapid grain growth in the HAZ occurs. The grain growth occurs under non-isothermal conditions, and is dependent on the thermal cycle. At the same time, the possible influences of particle pinning and impurity drag are factors to be considered.[2-61] The larger grains will grow at the expense of smaller grains to decrease the free energy which is available in the structure at any condition that represents a surface or an interface. The grain boundary movement is assumed to be a diffusional process. Since the metal structure is aspiring to gain a form which is thermodynamically stable, it would find this state of minimum internal energy when in the form of a single crystal or grain and with minimal surface area. The rate of grain boundary movement, or in other words, the extent of

grain growth, will depend upon the metal, its prior condition, and the environment to which it is exposed.

2.4.2. Kinetic Equations of Grain Growth

It has been well recognized that mechanical properties of materials are strongly related with the microstructure, especially its grain size. The control of the grain size of the transformation product is increasingly important. There are many models available to describe the grain growth in materials. The one used most commonly in metal is the parabolic grain growth equation deduced by Burke and Turnbull[2-62] from consideration of the driving forces on an isolated section of grain boundary. They modelled migration of a boundary as occurring by atom transport across the boundary under a pressure due to surface curvature. The boundary tends to migrate away from its centre of curvature as this reduces the area of boundary and hence the energy associated with it. Thus, the grain growth formula is

$$R_t^2 - R_o^2 = Kt \qquad (6)$$

where R_t is the mean grain size at time t, R_o is the initial mean grain size and K a constant. This equation is valid for both 3-D and 2-D geometries.

An alternative form of the above equation was presented by Feltham.[2-63] Assuming diffusion of atoms across a grain boundary to be an activated process, then the constant K in the above equation can expressed by

$$K = K_o e^{-\frac{Q}{RT}} \qquad (7)$$

where Q is an empirical heat of activation for the process, T temperature, K_o a constant, and R is the international gas constant. The grain growth equation is[2-63]

$$D^2 - D_o^2 = K_o t e^{-\frac{Q}{RT}} \qquad (8)$$

From above equation, it is obvious that the grain growth is a function of both temperature and time.

2.4.3. Factors Affecting the Grain Growth; Temperature and Time

When the metal is heated to a very high temperature, little free energy is required to stimulate grain growth, and the small amount of energy required always can be found somewhere in the structure. Both temperature and time determine the grain size. Consequently, if metal is heated to an excessive temperature for the purpose of welding, it may display abnormally large grains, particularly when exposure at the high temperature is of long duration. The temperature level at which this grain coarsening takes on significant proportions depends a great deal upon the metal or alloy. Steels tend to be separable into two classes. Some steels undergo exaggerated grain growth at temperatures above 1200(K), while others are quite resistant to grain growth at temperatures up to approximately 1422(K)[2-26].

For steels in the temperature range between the upper critical temperature and somewhere about 1473(K), the austenite grains form and grow relatively slowly, but above a specific point (the grain coarsening temperature) the rate of growth increases

sharply. Below the grain coarsening temperature, grain boundary movement is impeded by the presence of certain particles such as carbides. Grain growth occurs where the peak temperature of the weld thermal cycle exceeds the grain coarsening temperature. Below this temperature, the thermal cycle will usually produce a grain size that is smaller than that of the parent metal.

The type of microstructure developed in the coarse region on cooling depends on the carbon and alloy content of the steel, on the grain size and on the cooling rate.

CHAPTER 3

MODELLING OF HEAT TRANSFER IN RESISTANCE WELDING

3.1. Creation of the Model

Ideally, to model the welding process, it would be desirable to include the preheat, and the welding stage as well as the post-weld annealing parts of the weld cycle. However, a major difficulty with this ideal is that it is very difficult to model the welding stage because the geometry changes in a complex fashion during the extremely short period of welding current input (1-2 seconds). The temperature changes very rapidly while the welding current is applied. The geometry change of the weld is a function of the electrode force, the contact resistance and welding current. The central objective of this entire study is to determine what post-weld current profile will produce a non-martensitic HAZ. Therefore, to solve the problem, we set the model time=0 at end of the welding stage, using the fixed geometry of the welded sample.

It is well known that real heat transfer processes take place in three-dimensional space, and that this should be accounted for as much as possible in the analysis of heat-conduction problems. However, the solution of three-dimensional problems generally requires a tremendous amount of computational work, both in terms of programming, and computer time and memory. In practice, cases may be encountered in which

quantities change minimally with respect to one of the dimensions. Then, the three-dimensional problem may be reduced to a two-dimensional problem whose solution is much simpler. Therefore, a two-dimensional finite-difference model has been used instead of three-dimensions to calculate the heat transfer in this resistance welding project.

In order to model the heat transfer and microstructure development in the HAZ, we first set up a geometric model. A joint located in the welded wire meshes as shown in Fig.1-4 is chosen for modelling purpose, assuming the joint is cut along the centreline and has a profile as shown in Fig. 1-5.

The two-dimensional nodal network model created for cross welded bars is depicted in Fig.[3-1]. The model is composed of two bars welded perpendicularly with a HAZ along their junction. The pattern of the HAZ in the model is determined by measuring the HAZ of the real weld sample, because it is very difficult to predict an accurate size of the HAZ after a very short time welding current input, as discussed above. The contact area is not a constant at the period of welding current input which very quickly varies with current input and electrode force. Thus, the only way to approximate the HAZ contour in this geometric model is to use that of the real weld sample.

This model is reduced to two dimensions for purposes of heat flow as follows. The weld line (faying surface) between the two bars is assumed to be horizontal in Fig.[3-1]. If the bars are cut apart mathematically along this assumed horizontal weld line, then that because of symmetry, no heat passes across this weld line (i.e. $dT/dy = 0$ at the weld line). Therefore, only the bottom bar needs to be analyzed. The geometry of the

bottom bars has mirror symmetry along the centre plane perpendicular to the weld. So, only half of the bottom bar in the algorithm is needed for analysis. The model is then divided equally into a grid of 18 x 18 nodes. The spatial distance of the nodes is dependent on the thickness of wire being welded. For any given nodal region, there is an equal grid spacing in the x and y directions, that is $\Delta x = \Delta y$. The element grid is numbered as indicated in Fig.[3-1]. Each grid location represents a nodal point. The internal nodal points are designated by a numbering scheme for a two-dimensional system indicated in Fig.[3-1].

In modelling the resistance welding process, several other boundary conditions and physical phenomena must be considered. For purposes of simplifying this thermal model still further, the following assumptions and boundary conditions are specified.

1). There is no heat loss by radiation or convection to the environment. In the short duration of the weld and post-weld heating, this loss is insignificant and negligible compared with conductive heat transfer. The heat conduction losses are to the electrodes and to the surrounding base metal. These losses are directly proportional to local temperature differentials.

2). Because the greatest changes in temperature are in the vertical, rather than the horizontal direction, the current flow is assumed to be uniform throughout the regime in which it flows. The current path is restricted to the zone between the two dashed lines. This current path has been estimated according to measurements of the maximum contact area between the two workpieces. This means that the current flow only passes through the grids with x value between 10 and 18 in this model. The current flows

vertically across the contact area of the electrodes and workpieces, but no current flow is permitted along the lateral surfaces or vertical centreline.

3). No heat flow occurs across the centreline (dT/dx = 0 at centreline) nor along the contact faying surface of the workpieces because of symmetry assumed.

4). Elements at x=1 remain at 293(K) because of the high conductivity and thermal mass of the rest of the cold bar. The water cooled electrodes keep the lower surface (y=18) at 293(K). Along the uppersurface (y=1), there is no heat loss in the upward direction; convective and radiative losses are assumed to be negligible.

5). A unit thickness is assumed everywhere in the z-direction, and there is no heat flow towards the front and back surface (dT/dz = 0 everywhere).

6). The thermophysical properties and electrical properties are functions of the temperature.

7). The initial temperature distribution in this model is estimated from the measured austenite grain size as discussed in chapter 4.

3.2. Determination of the Physical Parameters

Both specific heat and thermal conductivity are considered to be variable with temperature. The equation for the thermal conductivity k (W/m. K) of the high carbon steel varies with temperature as follows[3-1]:

$$k = 27.83 \qquad T > 973\ (^{o}K) \qquad (9)$$

$$k = 52.0 - 0.031T \qquad T < 973\ (^{o}K) \qquad (10)$$

For ferrite steels, the specific heat has a steep peak at the Curie temperature.[3-2] The

specific heat can be represented by two simple functions as noted below:[3-3]

for T < 1000 (K)

$$C_p = \frac{1.117\times10^6}{(1010-T)^2} + \frac{12622}{1010-T} + 0.3485T + 355.6 \qquad (11)$$

and for T > 1000 (K)

$$C_p = \frac{1.225\times10^8}{(T-990)^4} + 0.1381T + 585.7 \qquad (12)$$

where C_p in J/kg K. The variation of specific heat is shown in Fig.[3-2], which also represents an average empirical fit to the data in Ref.[3-2]

In resistance welding, electric current flow creates heat. The amount of heat generated depends on the three factors: (1) the amount of current flowing, (2) the resistance of the conductor, and (3) the time of current flow. The heat generated is expressed in the formula[3-4]

$$Q_{(gen)} = I^2Rt \qquad (13)$$

$$R = \frac{\varphi x}{A} \qquad (14)$$

where $Q_{(gen)}$ is the heat generated within the element in Joules, I is the electric current passing through the welded pieces, R is the resistance of the material in ohms, t is the time of current flow in seconds, x is the distance which the current travels through the materials, A is the cross-sectional area perpendicular to current flow, φ is the resistivity (ohm.m). The resistivity is a function of the temperature. The variation of resistance

with temperature for the high carbon steel used in our resistance welding[3-1] is shown in Fig. [3-3]. The change in resistivity with temperature (K) has been divided into three separate linear approximations which are expressed as follows:

$$\varphi_I = 7.13\times10^{-4}T - 3.07\times10^{-2} \qquad 293 < T < 473\,(K) \qquad (15)$$

$$\varphi_{II} = 1.35\times10^{-4}T - 3.71\times10^{-1} \qquad 473 < T < 1073\ (K) \qquad (16)$$

$$\varphi_{III} = 2.31\times10^{-4}T + 8.9\times10^{-1} \qquad T > 1073\ \ (K) \qquad (17)$$

Equation 3-13 shows that the heat generated is proportional to the square of the welding current and directly proportional to the resistance and the time. The total heat generated during welding is partly used to heat the bars to the weld temperature and is partly lost to the surrounding metal. The greatest heat is generated at the point of contact between the two pieces being welded. This heat causes fusion and a change in the geometry of the bars as the hottest metal softens. However, the contact resistance exists until the element representing the point of contact between the two bars is completely melted. When melting occurs at the interface, it is reasonable to assume that the value of the contact resistance drops to zero.[3-5] From this point on, uniform heat generation due to resistance welding is assumed throughout the base metal. However, the resistance, and the local heat generated depends on the local temperature.

In the present work, the model is used to predict the post-weld heating and cooling history of the welded bars. Therefore, we assume the melting has already occurred at

the interface of the two weld bars. When the post-weld heating current is applied to weld bars, the heat generation is due to the resistance of metal itself which changes locally with temperature. Each element node has a different time-temperature history so that the resistance will vary with nodal point. The amount of heat production is dependent on how much and how long the post-weld heating current is applied.

Since the tip surface of the copper electrodes are easily deformed, and are also polished before welding, the electrode/bar interface resistance is assumed to be negligible. The water cooling in the electrode prevents them from heating significantly.

3.3. Heat Analysis

An energy balance is utilized for a given nodal network point at a given time step according to the first law of thermodynamics as follows:[3-6]

$$q_{inflow} - q_{outflow} + q_{generate} = q_{stored} \qquad (18)$$

This means that the rate at which thermal and mechanical energy enter a control volume (q_{inflow})plus the rate at which energy is generated within that volume ($q_{generate}$) minus the rate at which thermal and mechanical energies leave the control volume ($q_{outflow}$) must equal the rate of which energy is stored inside this volume (q_{stored}). The $q_{generate}$ is the heat generated by post-weld heating current in the resistance welding. The net heat change, q_{stored} is:

$$q_{(stored)} = \rho C_p V \frac{\partial T}{\partial t} \qquad (19)$$

where $\rho C_p \partial T/\partial t$ *is the time rate of change of the internal energy stored by the medium*

per unit volume, ρ *is the density,* C_p *the specific heat at constant pressure and V is unit volume (dxdydz).* For a solid element, with solid elements on either side, both q_{inflow} and $q_{outflow}$ are

$$q_x = -kA\frac{\partial T}{\partial x} \tag{20}$$

$$q_y = -kA\frac{\partial T}{\partial y} \tag{21}$$

where k is the thermal conductivity, A is the cross-section area which is normal to the heat flow. The simplest differential operator, ∂T/∂x, may be replaced with any of the following expressions (difference operators)[3-6];

$$\left.\frac{\partial T}{\partial x}\right|_{m-1/2,n} \approx \frac{T_{m,n} - T_{m-1,n}}{\Delta x} \tag{22}$$

$$\left.\frac{\partial T}{\partial x}\right|_{m+1/2,n} \approx \frac{T_{m+1,n} - T_{m,n}}{\Delta x} \tag{23}$$

for the y-direction ∂T/∂y there is a similar expression.

$$\left.\frac{\partial T}{\partial y}\right|_{m,n-1/2} \approx \frac{T_{m,n} - T_{m,n-1}}{\Delta y} \tag{24}$$

$$\left.\frac{\partial T}{\partial y}\right|_{m,n+1/2} \approx \frac{T_{m,n+1} - T_{m,n}}{\Delta y} \tag{25}$$

A finite-difference form of the time derivative is

$$\left.\frac{\partial T}{\partial t}\right|_{m,n} \approx \frac{T_{m,n}^{i+1} - T_{m,n}^{i}}{\Delta t} \tag{26}$$

where the superscript i is the time step. For the two-dimensional system, the energy conservation requirement can be performed on each of the nodes at a given time increment. The energy balance between an interior nodal point (m,n) and its four neighbouring nodes is described in Fig. [3-4]. Assuming all the heat flow into the node (m,n) by conduction under transient conditions with constant properties and no internal heat generation, the energy balance give

$$\sum_{j=1}^{4} q_{(j)-(m,n)} = 0 \qquad (27)$$

where the index j refers to the neighbouring nodes and $q_{(j)-(m,n)}$ is the conduction rate between the nodes which can be expressed as a simplified forms of Fourier's law as described in equations [20] and [21]. For example, the rate at which energy is transferred by conduction from node m-1,n to m,n is

$$\begin{aligned} q_x = q_{(m-1,n)-(m,n)} &= -kA\frac{\partial T}{\partial x} \\ &= k(\Delta y.1)\frac{(T^i_{m-1,n} - T^i_{m,n})}{\Delta x} \end{aligned} \qquad (28)$$

The quantity (Δy.1) is the heat transfer area A, where unit depth is assumed and Δx = Δy. The term $(T_{m-1,n}{}^i - T_{m,n}{}^i)/\Delta x$ is the approximate temperature gradient $\partial T/\partial x$ at the boundary between the two nodes. We can get similar heat conduction rate equations for the remaining nodes:

$$\begin{aligned} q_x = q_{(m+1,n)-(m,n)} &= -kA\frac{\partial T}{\partial x} \\ &= k(\Delta y.1)\frac{(T^i_{m+1,n} - T^i_{m,n})}{\Delta x} \end{aligned} \qquad (29)$$

$$q_y = q_{(m,n+1)-(m,n)} = -kA\frac{\partial T}{\partial y} = k(\Delta x.1)\frac{(T^i_{m,n-1} - T^i_{m,n})}{\Delta y} \quad (30)$$

$$q_y = q_{(m,n-1)-(m,n)} = -kA\frac{\partial T}{\partial y} = k(\Delta x.1)\frac{(T^i_{m,n-1} - T^i_{m,n})}{\Delta y} \quad (31)$$

Substituting equations [19],[26] and [28] to [31] into equation [18], we can obtain the solution of the temperature at any given time:

$$T^{i+1}_{m,n} = F_o\left(T^i_{m+1,n}+T^i_{m-1,n}+T^i_{m,n+1}+T^i_{m,n-1}\right) + (1-F_o)\,T^i_{m,n}+q^i_{(generate)\,m,n} \quad (32)$$

where F_o is Fourier number, equal to $\alpha\Delta t/(\Delta x^2)$. For the nodes which are not interior node, we still can apply the same method with obvious modifications to obtain the solution.

CHAPTER 4

DETERMINATION OF INITIAL TEMPERATURE DISTRIBUTION IN THE WELD

4.1. Some Complications with the Crossed Bars Model

In order to model the cooling rate and microstructure development in the HAZ after the end of the welding current, the temperature distribution and austenite grain size are needed input parameters. However, it is difficult to know what the temperature distribution is in the heat-affected zone after welding current has stopped. Furthermore, what value should be put into the program for the austenite grain size required for the metallurgical kinetic calculations at different nodal positions in the HAZ?

The prior austenite grain size is largely a function of the maximum temperature that a given point in the weld structure has reached during the welding process. But the problem is that the austenite is a high temperature phase which decomposes during cooling so that no austenite remains. The original austenite grain size becomes obscured in the low temperature phases which form from the austenite during cooling. The rate at which these low temperature phases form is strongly dependent on the original austenite grain size. It is the rate of these transformations that we are modelling with this algorithm. Therefore, it is very important to know the original austenite grain size in the HAZ. Moreover, if the austenite grain size can be found, then this can be related

to the corresponding temperature which existed at the end of the welding stage at different nodal points in the HAZ. This temperature distribution can then be used as a necessary input parameter in the model.

4.2. Determination of Austenite Grain Size at the End of the Welding Stage

4.2.1. Jominy Test

As mentioned above, it is necessary to establish the relationship between the austenite grain size and temperature for modelling purposes. The Jominy test seems an obvious method which can provide this reference.

The purpose of the Jominy test is to provide austenite grain size data for steel held at different temperatures with different hold times. The result is a set of reference microstructure pictures of austenite grain size as a function of temperature and time. From this experimental data, the relationship of the austenite grain growth with temperature and time can be established. This can then be used to derive an empirical equation of austenite grain growth for our resistance welding case to estimate the local peak temperature distribution in the heat-affected zone at the end of the welding cycle, if the austenite grain size in the HAZ of the real weld sample can be measured. These are obtained by a comparison chart method.

The "Jominy Test" for high carbon plain steel bars is done according to ASTM: A 255-88.[+1] The material used in our resistance welding and Jominy test investigation is a high carbon plain carbon steel. The composition of the steel is shown below:

Element	Carbon	Mn	Si	P
wt%	0.63	0.83	0.22	0.022

The specimen and the test apparatus is shown in Fig. [4-1]. The test conditions we used were: Austenizing temperature: 1144, 1200, 1255, 1311 and 1367°(K), (i.e. 1600, 1700, 1800, 1900, 2000°F); Hold Time: 30, 90, 180 minutes.

In the Jominy test experiment, the bars are heated up to a known high temperature, and held for different lengths of time to austenitize. The samples are then cooled directionally by squirting a controlled fountain of water against their lower surface. This will produce a spectrum of cooling rates varying from very high at the bottom end to very slow near the top. The samples are then cut at the lower end of the bars, and polished and etched to determine the austenite grain size.

4.2.2. Etching to Reveal Prior Austenite Grains

The austenite grain size is very difficult to reveal, especially in quenched and tempered Fe-C steels. It is somewhat easier in quenched steels. The various techniques available to reveal austenitic grain size, including special etching techniques have been reviewed by MillsopI.[4-2] For quenched or tempered steels, picric acid and Vilella's reagent are most commonly recommended to reveal austenite grain size in martensite.[4-3] A better etching result is to combine picric acid with a wetting agent such as sodium tridecylbenzene sulphonate.[4-4]

However, the author used Sunlight Detergent instead of sodium tridecylbenzene sulphonate because of difficulties in supply. The Sunlight Detergent contains sodium tridecylbenzene sulphonate. So the Sunlight Detergent gave reasonably good results for the development of austenite grain boundaries in our experiments, both for the Jominy tests and welded bars. Specimens etched by Vilella's reagent and saturated picric acid

were not successful, only partially revealing the austenite grain boundaries.

The successful etching solution consists of saturated picric acid in distilled water (100 ml), Sunlight detergent (4 grams) and HCl which is added before etching (about 10 drops). The amount HCl depends on carbon content of the steel. The sample which is ready for etching should have a fresh surface. Immerse the freshly polished sample in etchant with ultrasonic agitation for about 5 minutes. The time is dependent on austenizing conditions. Remove the sample, wash and dry. When observed under the microscope, the outlines of the original austenite grain boundaries are revealed in the structure of the sample. To delineate the boundaries better, very lightly polish samples on 0.05μ alumina wheel until the matrix structure is mostly removed, leaving the austenite grain boundaries. Then, re-etch the samples according to above procedures.

4.2.3. Quantitative Metallography

Many methods for measuring grain sizes in a wide range of materials are described in the literature[4-5]. Their success depends only on the grain boundaries being clearly revealed and being unmistakably austenite boundaries. In measuring the austenite grain size in the resistance welded and the Jominy test specimens, the comparison chart method and the linear intercept method were utilized. The choice of method depends on the appearance of the austenite grain in welded bars and Jominy test samples.

In the comparison chart method, the photographs taken from optical microscope at 200X are matched with standard network charts which correspond to ASTM austenite grain size number from 1 to 8, at 100X. The magnification either higher or lower than 100X can be corrected according to the following relationship[4-5,6]:

$$Q = 2\log_2\left(\frac{M}{M_b}\right)$$
$$= 6.64\log_{10}\left(\frac{M}{M_b}\right)$$

To get the true ASTM grain size number, Q is a correction factor that is added to the apparent grain size of the specimen, as viewed at the magnification, M, instead of at the basic magnification, M_b (75X or 100X). Extra standard network charts were created which represent the grain size number 0, 0.5, 1.5, 2.5, 3.5, 4.5, 5.5, 6.5 and 7.5 by magnifying the standard network charts 1.189 time according to the expression $2^{(n-1)}$, where n is the ASTM grain size number, so that we could estimate grain size more accurately.

In the linear intercept analysis technique[4-5], random lines of known length are superimposed over the micrograph and the number of intercepts are counted. Then, dividing the total length by the total number of the intercepts and the magnification, the average grain size is obtained. This is a useful method when the appearance of all the austenite grain boundaries is clear.

In the weld samples, it is very difficult to determine the grain size. When examining the austenite grain boundaries of the welded bars, the comparison method is more suitable because all the boundaries are not continuous and clear, and because the grain size in the HAZ changes too fast with different position from the fusion line to obtain an accurate calculation.

The grain size (D) and grain size number (n) have a relationship as[4-7]:

$$2^{n-1} = \frac{0.06452}{D^2} \qquad (34)$$

which makes it easy to convert from one to the other.

4.3. Jominy Test Results and Discussion

4.3.1. Jominy Test Results

Figures [4-2a] to [4-2c] display a set of optical photographs, at 200X, for the austenite grains in the quenched martensite microstructure obtained from Jominy test bars from different temperatures and different soaking times. These are taken as reference pictures. The purpose is to estimate the austenite grain size in the heat-affected zone after resistance welding. To do this, these pictures are used as a base for the derivation of relative empirical equations. In these microstructures relating austenite grain size to temperature and time, the martensite grains, light grey, are enveloped by the darker austenite grain boundary lines. Some austenite grain boundaries are blurry or only turn out partially. The austenite grains, of course, no longer exist but their original position is revealed because of impurity atom segregation at original austenite grain boundaries which is retained during the rapid transformation to martensite. It is not surprising that it is difficult to clearly etch up these boundaries.

The results of austenite grain size measured as a function of time, and temperature from Jominy test are reported in table [4-1] and are plotted in Fig.[4-3] and [4-4].

4.3.2. Discussion

The mechanism of austenite grain growth is generally accepted to be diffusion controlled. The release of carbide-pinned austenite boundaries depends on carbon

diffusion through the austenite as the carbides dissolve. This gives the result that the amount of austenite increases quickly after the carbide dissolution temperature is exceeded, then gradually slows down as time increases. This is shown in the Jominy test results. The longer the hold time for austenitizing, the larger the austenite grain size, but the increase in grain size is not as fast as the initial stage (Fig.[4-2]).

At higher temperatures, the diffusion rate increases, and the more rapidly the austenite grains grow. Figures [4-2a,b,c] shows that in our 0.63% carbon steel when the austenitizing temperature was raised from 1144 to 1367°(K), the grain size at the higher temperature is much larger than that at lower temperature. Because of the limits of furnace, we have only short time data (30 minutes) for the highest temperature.

In actuality, some of the islands of austenite grow more rapidly than others; therefore, when a large grain encounters a small one, the small one is forced to shift its orientation, layer by layer, thus losing its identity while being absorbed into the larger grain.

Non-ferrous carbides which do not dissolve until temperatures are well above A_{e3} also inhibit grain growth, because they provide low energy sites for themselves in the austenite boundaries. Movement of the boundaries away from the carbides will increase the free energy of the entire system. An interesting effect of these so-called "grain-growth inhibitors"[4-6] is that when they finally become ineffective at some elevated temperature, as a result either of solution or of coalescence, the amount of grain growth is then likely to be greater than in a steel that is free from such a restraint. Such steels retain a fine grain almost unchanged during heating at successively higher temperatures

until abruptly, here and there, a single large grain forms from as many as 100 or more former small grains.[4-6] Prolonged heating, or a rise in temperature, will ordinarily convert the remaining fine grains to the same type of large grain as first formed upon reaching the coarsening temperature. This is evident in the microstructures of Fig.[4-2], where the rate of grain size change decreases as the hold time increases.

It should be remembered that the persistence of carbide and attendant retention of small grains is often a matter not of equilibrium but of rate of solution, and carbides frequently remain undissolved for 30 minutes or more in eutectoid steel heated well into the austenite temperature range. Therefore, the uniform austenizing according to ASTM specification for the Jominy test requires that the sample be kept at a given temperature not less than 30 minutes in the oven.

4.4. Derivation of Empirical Formula for Grain Growth

The purpose of development of an empirical austenite grain growth equation is to find a relationship between grain size vs temperature and time based on the Jominy test data so that it can be used to map the temperature in the weld. For a given measured weld grain size and time, the related temperature in the HAZ can be estimated at the end of the weld cycle.

According to widely accepted parabolic grain growth kinetics,[2-62] the grain growth equation by Feltham is[2-63]

$$D^2 - D_o^2 = K_o t e^{-\frac{Q}{RT}} \qquad (35)$$

or

$$D^2 = D_o^2 + K\ t \exp\left(-\frac{Q_i}{RT}\right) \qquad (36)$$

where D is the current grain size, D_o is the initial grain size, K is an empirical constant, Q_i is an empirical heat of activation for the process, t is time in seconds, T is temperature in degrees Kelvin, R is the international gas constant.

To derive an empirical austenite grain growth equation from the experimental results of the Jominy tests shown in Fig.[4-3], the equation [36] is used as a core. First, the set of equations for the grain size vs time relationship at a given temperature are obtained by regression on the experimental data as shown in table [4-2]. The different intercepts represented by D_o are extrapolated from the test data back to Y-axis at zero or very short times. It is obvious that the D_o in Fig. [4-3], based on Jominy test results does not have a single value. It is noticed that at lower temperatures, the difference of the D_o is small. It increases as the temperature increases. It will be even farther away from the origin when austenizing is at higher temperatures where austenite is coarsening very fast. Theory demands a single D_o value. But the use of a fixed D_o will not predict the experiment data. Based on Jominy test results, D_o therefore is assumed to be a function of temperature, which is expressed as:

$$D_o^2 = M_A \exp\left(-\frac{Q_A}{RT}\right) \qquad (37)$$

where, M_A is constant, Q_A is activation energy, Then, the derived equation for D_o is represented as follows:

$$D_o^2 = 2.2471 \times 10^5 \exp\left(-\frac{28965}{T}\right) \qquad (38)$$

As a shorthand in equation [36], we set:

$$B = K \exp\left(-\frac{Q_i}{RT}\right) \tag{39}$$

so that

$$D^2 = D_o^2 + Bt \tag{40}$$

where B represents the slope which is obtained from above regression equation. The alternative expression for equation [39] is:

$$\ln B = \ln K - \frac{Q_i}{RT} \tag{41}$$

As we substitute the data obtained for Jominy test into equation [41], the unknown variables Q_i and K can be solved. The final equation for grain growth derived from the above assumptions becomes:

$$D^2 = D_o^2 + K\,t \exp\left(-\frac{Q_i}{RT}\right)$$
$$= 2.247 \times 10^5 \exp\left(-\frac{28966}{T}\right) + 0.427 \exp\left(-\frac{21892}{T}\right) t \tag{42}$$

Then, the grain size variation with time and temperature is calculated with this equation. The computed results are compared with data acquired from the experiments and with the results using other equations derived from different D_o assumptions. The standard deviation comparing calculations of grain growth results using different derived equations with the data obtained from Jominy test are shown in Table 4-3. The calculation results for different methods are shown in Tables [4-4] to [4-6]. The comparison of calculation data with experimental data at different test temperatures is

plotted in Figs. [4-5a,b,c,d].

4.5. Empirical Grain Growth Equation Applied to Resistance Welding

The empirical grain growth equation [42] obtained from results of Jominy tests describes a relationship between grain size vs temperature and time. The grain size and grain size number can be converted to each other using Equation [34]. It is practical to assume that D_o is a function of temperature instead of a constant. We can see that the standard deviation is the smallest when assuming a temperature dependent D_o. There is no theoretical basis for assuming that D_o varies in an Arrhenius type manner. However, assuming this it does produce a good fit with the experimental results, and in view of the preceding discussion about the irregular nature of carbide inhibited grain growth, the extrapolation of long term (minutes) grain size measured in the Jominy test back to short time (seconds) weld HAZ has a very shaky basis. On the other hand, the common parabolic grain growth equation clearly does not apply, and even approximate short-time experimental data (15 seconds or less) is not obtainable. Therefore, a quadratic grain growth function, where D_o varies in an Arrhenius manner, has been used in the present model. Equation [42] has a smaller value of standard deviation for the Jominy data, so we use it to predict grain growth in the heat-affected zone of resistance welding. The calculation of grain size and grain size number vs temperature at one second using the empirical equation is shown in Fig. [4-5] which fairly reflects the tendency of grain size development in resistance welding in such a short time heat input. Lacking a better approach, we assume that equation [42] can give a satisfactory delineation of grain growth in the heat-affected zone of resistance welding, especially for grain growth in

a very short period of time when the work piece metal suffers a superheating thermal cycle.

4.6. The Predicted Temperature distribution in the HAZ at the End of Welding Current

The strip on the left hand side of Figures [4-7] is a photograph, originally at 200X, of a part of the austenite grain map in the HAZ along centre line taken from resistance welding samples where no post-weld heating is applied. The HAZ in resistance welding has a elliptical shape. The width of the HAZ is about 6 to 8 mm, depended on welding conditions. The fusion zone is very thin so that it only shows as a dark line in our resistance welds. The microstructure in this HAZ is mainly quenched martensite. The austenite grain boundaries which have been etched up reflect the prior austenite grain size. The measurement of austenite grain size along the centreline of the HAZ is shown in table [4-7]. Next, the temperature distribution in this specimen is predicted using the empirical equation [42], according to the results from the measured austenite grain size. The temperature distribution and grain size change along the centre line of heat-affected zone at the end of welding current are plotted in Figs.[4-8]. The prediction of temperature and grain size contour are shown in Figs.[4-9] and [4-10]. The peak of the curves represents the position of the fusion line.

From the photographs of the austenite grain size in the HAZ, we can see that the austenite grain size varies extremely quickly from fusion line (dark line) to base metal after the short time welding current is applied. By definition, the temperature reached is high enough to cause austenization in the heat-affected zone. Grain growth will occur

where the peak temperature of the weld thermal cycle exceeds the grain coarsening temperature. The greatest austenite grain coarsening is just adjacent to fusion line where it experiences considerable superheating, in a strip which is about 2mm wide.

The grain size is governed by the nature of the weld current input and the grain coarsening temperature of the steel.[4-8] For any given steel, the greater the heat input rate, the longer the time spent above the grain coarsening temperature, and the coarser the grain (Fig.[4-7]). Also, for any given weld thermal cycle, the higher the grain coarsening temperature the shorter the time for grain growth. The type of post-weld microstructures developed in the coarse-grained zone depends on the carbon and alloy content of the steel, on the austenite grain size and on the cooling rate. In the steel used in the present study, no ferrite is formed.

Also, a coarser austenitic grain size will produce the formation of harder microstructures than would result from the transformation of a finer-grained material. From the predicted IT diagram (Fig.[6-12]) discussed in the next chapter, we can see that increasing the austenite grain size has the effect of shifting the C-curves to a longer transformation time. This increases the opportunity to form brittle martensite. It is very hard to explain the very fast austenite grain coarsening in such a short time (1 second). However, in the austenite range, thermal movement of the atoms is rapid enough to cause grain growth, so that extended time and high temperature in the austenite range are capable of greatly increasing the size of the initial austenite grains[4-9]. The predicted temperature gives a very good description of this tendency to sudden change.

Cracking develops frequently in the area of coarsened grain zone.[4-10] In fact, all the

samples welded with this schedule in experimental set were cracked in the coarse grained zone near the weld line as shown in Fig.[4-11]. The cracks began at the edge of the flashing expelled during welding. So, if the size of coarse grained zone can reduced so as to increase the fine grain zone, the toughness of the weld in the HAZ may be greatly improved. Otherwise, a post-weld heating schedule must be devised which will reduce the thermal stresses created to a bearable level until the austenite diffusional decomposition processes can occur.

CHAPTER 5

THEORETICAL BASIS FOR MODELLING OF MICROSTRUCTURE DEVELOPMENT IN RESISTANCE WELDING

In developing the algorithm for metallurgical kinetics to model the austenite decomposition into its daughter products in the post-weld cooling stage of resistance welding, the hardenability algorithm developed by Kirkaldy and co-workers is used as the core for our developing an algorithm of microstructure development.

5.1. Determination of Transformation Temperatures

To predict the microstructure development in the algorithm, the temperatures of transformation points of austenite daughter products should first be determined.

The calculation of A_{e3} temperature is based on the work by Kirkaldy and Baganis[5-1], which gives an equation as follows where the compositions are in wt%.

$$\begin{aligned} A_{e3}(^{\circ}C) = {} & 912 - 203\sqrt{C} - 30Mn + 44.7Si - 15.2Ni \\ & - 11Cr + 31.5Mo - 20Cu + 104V + 13.1W \\ & + 700P + 400Al + 120As + 400Ti \end{aligned} \qquad (43)$$

The pearlite start temperature or eutectoid is taken from Grange's early work[5-2]. The bainite start temperature is from ref[5-3], and finally, the martensite start temperature adapted from Steven and Haynes[5-4]. These equations are described below:

$$P_s(°C) = 723-13.9Mn-14.4Ni+22.2Si+23.3Cr \quad (44)$$ [52]

$$B_s(°C) = 656-58C-35Mn-75Si-15Ni-34Cr-41Mo \quad (45)$$

$$M_s(°C) = 561-474C-33Mn-17Ni-17Cr-21Mo \quad (46)$$

These equations [44] to [46] have been shown to be used to predict, with good accuracy, isothermal transformation diagrams for plain carbon steels and low alloy steels[5-2,3,4].

5.2. Modelling the Decomposition of Austenite

As discussed above, austenite will undergo a decomposition reaction into any of its daughter products in resistance welding, depending on the undercooling rate. The transformation reactions of austenite on cooling are modelled using an Avrami type equation given by Kirkaldy and Venugoplan[5-(3,5,6)]. These equations assume that a single continuous function can describe both the nucleation and subsequent growth for each of the austenite daughter phases. For each reaction, the general reaction rate is characterized as

$$\frac{dX}{dt} = B(G,T)X^m(1-X)^p \quad (47)$$

where X is the volume fraction of the daughter product, B is an effective rate coefficient related to the carbon diffusion activation energy, G is the austenite grain size, T is the temperature and m and p are semiempirical coefficients set to less than one to assure convergence in a form that is derived from a point nucleation and impingement growth model[5-7], which can expressed as:

$$m = F(1-X);$$
$$p = SX;$$

F and S are chosen arbitrarily. In Kirkaldy's algorithm, both F and S are set to 2/3.

To use Kirkaldy's expressions in the present resistance welding problem, the amount of daughter product calculated in any time step Δt is given as:

$$\Delta X = B(G,T)X^m(1-X)^p\Delta t \qquad (49)$$

The rate coefficient B includes the effect of grain size on the density of eligible nucleation sites. It also includes the magnitude of austenite supercooling and the effect of alloying elements and temperature on diffusion, which yields an expression:

$$B \approx \alpha(G)D\Delta T^q \qquad (50)$$

where q is an empirical exponent determined by the effective diffusion mechanism (for pearlite, q = 2 for volume diffusion and q = 3 for boundary diffusion[5-8]). ΔT is supercooling, D is an effective coefficient to take into account the diffusional resistance of the reaction based on Fe-C. This can be represented as the general form

$$\frac{1}{D} = \frac{1}{D_c} + \sum_{i=2}^{n}\frac{k_i C_i}{D_i} \qquad (51)$$

where D_c diffusion coefficient for carbon; and D_i is the grain boundary diffusion coefficient for the other ith alloying elements which have the concentration C_i. The matrix k_i are empirical constants. The empirical grain size factor $\alpha(G)$ is given as

$$\alpha = \beta . 2^{\frac{(G-1)}{2}} \tag{52}$$

and ß is commonly about 1. For the austenite to ferrite reaction rate, Kirkaldy prescribed

$$\frac{dX}{dt} = \frac{2^{\frac{(G-1)}{2}} \Delta T^3 X^{f(1-X)} (1-X)^{sX}}{59.6\%Mn+1.45\%Ni+67.7\%Cr+244\%Mo} \tag{53}$$

where dX/dt is in units of volume fraction per second; G is the ASTM gain size number for the austenite; $\Delta T = A_{e3} - T$ is the undercooling; X is amount of existing daughter product volume fraction. Ferrite which forms during an incremental time step and is added to the previous amount of ferrite at each individual node.

As the temperature falls below the eutectoid temperature, the second daughter product of austenite, namely pearlite, begins to nucleate. It is assumed that pearlite does not, at first, interfere with the formation of ferrite, thus ferrite continues to form until the pearlite content reaches 1%. The rate of pearlite growth is governed by an equation similar to equation described above and is given by:

$$\frac{dX}{dt} = \frac{2^{\frac{(G-1)}{2}} \Delta T^3 D\, X^{f(1-X)} (1-X)^{sX}}{1.79+5.42(\%Cr+\%Mo+4\%Mo\%Ni)} \tag{54}$$

where D is evaluated as

$$\frac{1}{D} = \frac{1}{\exp(-27,500/RT)} + \frac{0.01\%Cr+0.52\%Mo}{\exp(-37,000/RT)} \tag{55}$$

and $\Delta T = Ps - T$, the degree of the pearlite undercooling. At the onset of pearlite formation, the amount of unreacted austenite will be $(1-X_F)$, then the appropriate value for amount of pearlite formation is $X = Xp/(1-X_F)$.

When the temperature drops to below the bainite start temperature, it is supposed that pearlite growth degenerates to bainite formation. The rate of the bainite reaction is controlled by the following equation:

$$\frac{dX}{dt} = \frac{2^{2}\,(\Delta T)^{2}\exp\left(-\frac{27,500}{RT}\right)X^{f(1-X)}(1-X)^{sX}}{(2.34+10.1\%C+3.8\%Cr+19\%Mo)\,10^{-4}f(X,C_i)} \qquad (56)$$

where

$$f(X,C_i) = \exp[X^{2}(1.9\%C+2.5\%Mn+0.9\%Ni+1.7\%Cr+4\%Mo-2.6)] \qquad (57)$$

where ΔT = Bs - T, the cooling rate of metastable bainite and X is the amount of pearlite and bainite present. It must be noted that $f(X,C_i)$ is set to 1 for all negative values of the exponent in the equation for $f(X, C_i)$.

If pearlite exists when the bainite start temperature is crossed, then it is assumed that the existing pearlite-austenite interface continues to transform, but bainite is the transformation product. Then X in equation [55] is original Xp. If no pearlite exists, then because the bainite reaction is sluggish, X is simply the fraction of bainite formed and it continues to transform until the remaining austenite is consumed or the Ms temperature is reached.

Upon reaching the martensite start temperature , any remnant austenite is assumed to transform to martensite athermally.

5.3. Modelling of Isothermal Transformation Curves

To ensure that the algorithms are appropriate and are working correctly, a simple test is to use them to predict known isothermal transformation diagrams for the

diffusional decomposition of austenite to its daughter products. This may be accomplished numerically for any carbon content with specified austenite grain size, guided by the principle of calculating volume fraction transformation products using Kirkaldy's algorithm. The alternative form of equation [47] can be expressed as:

$$\tau(X,T) = \frac{1}{\alpha(G)D\Delta T^{q}} \int_{0}^{X} \frac{dX}{X^{f(1-X)} \cdot (1-X)^{sX}} \qquad (58)$$

where $\tau(X,T)$ is the time required to form X amount of any transformation products of austenite during an isothermal hold temperature T. Using equation [57], the time and temperature with volume fraction of transformation products relationship can be established. To model the IT Curve, the volume fraction of polycrystalline pearlite (Xp) vs time (t) data arrays must first be computed at a series of different temperatures a few degrees below the pearlite start temperature for any composition with the given carbon content. Other alloy element compositions and austenite grain size can also be calculated for comparison. As explained in detail in chapter 6, these results have been used to alter Kirkaldy's equation to get a better prediction for high carbon steel. Next, by interpolation of the Xp vs time data arrays, a new data array, T vs t (Xp=constant), may be generated where t is the time to achieve a volume fraction Xp under isothermal transformation at specified temperature T. Finally, after a series T vs t data arrays are computed, each at different Xp values, a plot of the results with lines drawn through points representing the same Xp yields the IT diagram. For the above computation, we assume that the transformation of pearlite is still going on even though the bainite start temperature is passed so that the nose of line curve will occur and ferrite transformation

is stopped when its volume fraction reaches 1 percent. So, the algorithm developed will be suitable for prediction of IT diagrams of any Fe-C steel selected.

5.4. Computer Programming Aspects

The algorithm is coded in ANSI standard C. The initial parameters: steel composition, local austenite grain size, welding thermal cycles and starting nodal temperatures, are entered. The transformation temperatures for the given steel composition are computed. Next, the algorithm finds the thermophysical parameters (thermal conductivity k, specific heat C_p, resistance, etc.) according to the temperature reading at each node. The heat balance on each node can now be evaluated at any incremental time step, using the appropriate heat transfer equations, and the new temperature at each node will be found. Depending on the computation of thermal condition (temperature, grain size, and composition), the microstructure evolution for ferrite, pearlite and bainite at each node in heat-affected zone for a given time step and temperature are estimated, using the modified Kirkaldy's kinetic algorithm. The appropriate austenite grain size number for each nodal point can be read from the initial temperature map in the HAZ. It should be noticed that the austenite grain size at each node is different because each node experiences a different austenizing temperature. For modelling the microstructure development, the choice of grain size is important. The programming results are recorded in several data files to produce output. The appropriate post-heat cycles are obtained by analyzing the several coupled calculations. The program is conveniently written to deal with different input conditions. The details of the algorithms and the data file are presented in the appendices.

CHAPTER 6

DEVELOPMENT OF A MORE ACCURATE ALGORITHM FOR MODELLING MICROSTRUCTURE DEVELOPMENT IN RESISTANCE WELDING

6.1. Modification of Kirkaldy's Algorithm to Get A Better Empirical Fit to IT Diagram

The principle of the algorithm developed by Kirkaldy and coworkers for modelling the thermodynamics and kinetics of austenite decomposition was described in the last chapter. This work was based on an extensive study of a few hundred types of plain carbon steels and low alloy machinery steels.

In our investigations, we have found that some aspects of the algorithm could probably be improved for our resistance welding process purpose if we concentrate only on the steels whose composition is within the following ranges:

Carbon:	0.35 to 0.95%
Manganese:	0.15 to 1.3%
Silicon:	< 0.3%
Ni+Mo+Cr:	< 0.2%
All others	< 0.1%

This excludes all the machinery steels with which Kirkaldy was particularly interested,

since his algorithms were mainly for use in heat treating hardenability applications. These types of steels are not suitable for our welding process.

The present work of developing a more accurate algorithm consists of taking nine compositions from the "Atlas of Isothermal Transformations" and adjusting some of the coefficients of equation [47] to achieve a better fit for this narrower range of steels. To data, the diagrams and tabulated the data from these diagrams for a few selected temperatures have been copied. For comparison, the original Kirkaldy algorithms have been run to determine what sorts of systematic errors are observed. In the resistance welding case, it has been found that using Kirkaldy's equation unmodified for the higher carbon and manganese content have a tendency to delay the time of transformation start and finishing, compared with the IT diagrams from "Atlas of Isothermal Transformation Diagrams". In the Π diagram calculated by Kirkaldy's algorithm, the transformation rate part for some higher carbon and Mn steel is too slow for the pearlite start time, or too fast for the pearlite end time. Therefore, we have tried to alter the program to minimize these deviations. As shown in equation [47],[48]:

$$\frac{dX}{dt} = B(G,T)X^{m}(1-X)^{p}$$

and

$$m = F(1-X);$$
$$p = SX;$$

the main approach has been to alter the two exponents in the part of the algorithm that assures that the boundary conditions are met and get a better fit to the experimental

diagrams from "Atlas of Isothermal Transformations". In the equation [48], F and S were determined arbitrarily by Kirkaldy. So they are adjustable for modelling purposes. Both F and S are set to 2/3 in Kirkaldy's algorithm. On a series of trials based on altering the value of the two exponents, it is found that the start time of transformation is controlled by the F value, and the finishing time is controlled by the S value. The influence of the two exponent values are depicted in Figs. [6-1, 2, 3]. Clearly a decrease of the F value to smaller than 2/3 will accelerate the start reaction rate. This moves the "S" shape curves to the left as shown in Fig.[6-2,3]. Meanwhile, an increase of the S value to larger than 2/3 will retard the finishing reaction rate as shown in Fig.[6-1]. In order to get a better fit to the IT diagram for the composition used in this resistance welding, the F was set at around 0.57 to 0.59, and the S value around 0.77 according to the trial computing results.

The final computing results for selected plain carbon steels using the modified algorithm for calculating isothermal transformation curves are depicted in Figs.[6-4] to [6-9], which compare the calculated IT diagrams with Kirkaldy's algorithm and the experimental IT diagrams obtained from "Altas of Isothermal Transformation". For comparison, the effect of changing Mn at fixed carbon content, and changing carbon content at fixed Mn content were evaluated. As well, the effect of changing the austenite grain size on IT diagram was studied. The results are shown in Fig.[6-10] to [6-12].

6.2. Results and Discussion on Modelling of IT Diagrams

6.2.1. Comparison of Calculated IT Diagrams with Kirkaldy's and Experimental IT Diagrams

As delineated in Fig. [6-4] to [6-9], the IT curves calculated using the modified algorithm are composed of three basic C-curves, which represent 1%-curve (transformation start), 50%-curve, and the finishing-curve (transformation end) respectively. Meantime, the calculated IT curves are compared with the IT curves using Kirkaldy's original algorithms and experimental results from "Atlas of Isothermal Transformation". By changing the exponents F from 2/3 to 0.57 and S from 2/3 to 0.77 in Kirkaldy's equation [47],[48]:

$$\frac{dX}{dt} = B(G,T)X^m(1-X)^p$$

and

$$m = F(1-X);$$
$$p = SX;$$

It is exhibited in the figures that the modified algorithm can speed up the time for the formation of the pearlite at 1% and 50% and slow down the time for the end of pearlite formation. This change produces a better fit of the experimental curves taken from "Atlas of Isothermal Transformation and Cooling Transformation Diagrams" than Kirkaldy's algorithm, especially in the case of 1080, 1060 (0.64%C), and 1060 steels as shown in Figs. [6-4,5,6]. These compositions are in the range of our resistance welding composition. For the case of 1566, 1050, 1055 (0.54%C) steels, the fit is either

better for the start curve and 50% curve or the end curve of the pearlite transformation. It is also indicated in Figs. [6-4] to [6-9] that all of the IT curves predicted have a better accuracy in fitting either the start part or the end part of IT curves or both than IT curves assessed by original Kirkaldy's algorithm, for compositions close to these in our welding steels. Therefore, the modified algorithm of kinetic transformation has been used to predict the schedule of post-weld heat applied to control the cooling rate in the resistance welding process and the microstructure development of welded bars.

6.2.2. Effect of the Exponent on the Algorithm

In this investigation, the exponents chosen for the general formula of kinetic transformation play an important role in determining the transformation rate. The reaction kinetics modelled by the algorithm for predicting IT curves are, to some extent, determined by the exponents F and S described in equation [48] and by other factors such as the coefficient for alloying content, the austenite grain size chosen, the amount of alloy elements, etc. Like the Avrami type equation discussed before[2-46],

$$X = 1 - \exp(-bt^n)$$

the sigmoidal shape is considered to reflect the relative effects of a combined nucleation and growth transformation process, as is characteristic of the austenite-to-pearlite transformation in eutectoid steels. In the Avrami equation [3], b and n are constants, which are determined from experimental isothermal-transformation "start" and "end" curves. In the numerical kinetics equation [47], there is a similar effect in that the volume fraction of transformation products vs time gives a sigmoidal shape curve at a

given temperature. The reaction rate of an isothermal transformation is partly determined by the exponents F and S which respectively reflect the relative effects of a combined nucleation and growth transformation. The start of the transformation rate is controlled by F and the end of the transformation rate is controlled by S. A decrease in the value of the exponent (F) will result in increasing of initial reaction rate of pearlite transformation. This shorts a reaction time and moves the 1% and 50% curves towards the left in the IT diagram. An increase in the value of the exponent (S) will slow the reaction rate of transformation products and postpone the finishing time. This moves the finishing curve towards the right. These effects can be shown in Figs.[6-4 to 9]. Therefore, it is necessary to modify the exponents in the Kirkaldy's algorithm to get better modelling results.

6.2.3. Effect of Alloy Elements on Algorithm

The primary feature of adding alloying elements to a steel is to shift the curves on an IT diagram to longer times. Any variable that moves the pearlite transformation line to the right in IT diagrams makes it more possible to obtain the undesirable martensite structure at a slower rate of cooling by slowing down the nucleation and growth of pearlite in the steel. In resistance welding, this allows the steel to be cooled more slowly, but still retain its austenitic structure down to the Ms temperature.

It is shown in the algorithm for predicting IT diagrams that manganese has a strong tendency to move the IT curve towards the right as shown in Fig.[6-11]. As well, it is evident that formation of pearlite and proeutectoid constituents becomes more difficult the higher the carbon content of the steel; increasing carbon content is associated with

an increase in hardenability Fig.[6-10]. The post-weld heat schedule must be applied to avoid the formation martensite so that the toughness of heat-affected zone can be improved.

Basically there are two ways in which carbon and alloying elements can reduce the rate of austenite decomposition.[6-1] They can reduce either the growth rate or the nucleation rate of ferrite, pearlite, or bainite. Firstly, they can alter the A_{e1} and A_{e3} according to equation [43] and [44]. By lowering the A_{e3}[6-1] temperature the austenite stabilizing elements reduce the undercooling for a given isothermal reaction temperature, and hence the driving force for transformation of austenite. The rate of austenite transformation is thereby delayed by diffusion of solutes. Other factors that may delay the transformation are preprecipitation clustering of substitutional and interstitial solutes, and solute drag by the advancing γ-α interface boundary. The slower the time-dependent processes of nucleation and growth, the greater the time available to reach the Ms temperature, for a given cooling rate.

The second means by which alloying elements can delay the decomposition of austenite is as follows. At equilibrium an alloy element M will have different concentrations in cementite and ferrite, i.e., it will partition between the two phases. Carbide-forming elements such as Cr, Mo, Mn will concentrate in the carbide while elements like Si will concentrate in the ferrite. When pearlite forms close to the A_{e1} temperature, the driving force for growth will only be positive if the equilibrium partitioning occurs. Since M will be homogeneously distributed within the austenite, the pearlite will only be able to grow as fast as substitutional diffusion of M allows

partitioning to occur. The most likely diffusion route for substitutional elements is through the γ/α and γ/cementite interfaces. However, it will be much slower than the interstitial diffusion of carbon and so, will reduce the pearlite growth rate.

On the other hand, austenite grain size is a bigger factor in determining the IT-curve. Using the modified Kirkaldy equation, the effect of grain size is shown in Fig.[6-12]. A small austenite grain size can promote the isothermal transformation reaction to finish in a short time but as the grain size is increased, a longer time is needed to complete the reaction. This shifts the C-curve to the right and means the rate of transformation is slowed down. This means if the austenite grain size in a steel is coarse, fewer nucleation sites of pearlite are available and diffusion-controlled transformation of the austenite is retarded since it takes a longer time for the carbon rejected from the ferrite to reach the centres of the grain.

CHAPTER 7

EXPERIMENTAL OBSERVATION

In order to demonstrate the accuracy in prediction of the microstructural development, some experimental work on different post-weld heat schedules was carried out at Coschell Inc. Consequently, the microstructure changes in the real welded samples were observed and photographed and these are used as a reference to evaluate the modelling results of microstructural development.

7.1. Trials in Real Resistance Welding Process

To determine an optimum post-weld heating parameter that provides a desirable normalized microstructure in the welded metal, and to compare the computed results with real weld pieces, a set of weld samples has been prepared with varying post-weld heat inputs. This was carried out on the welding machine at Coschell Inc.. As shown in Fig.[1-2], the post-weld heating cycle can be composed of either one part (only a horizontal line) or multiple parts (a sloping line and a horizontal line). The welding current used for our tests was 3183 Amps per weld. The power factor is 79, and the frequency was 60 (Hz). The welding current time was 80 cycles. The post-weld heats applied with different percentages of welding current input and hold time, are shown in table [7-1]. All of the welded joint samples for different post-weld heat were used for microstructural observation.

The weld samples at different post-weld conditions were cut along the centreline of

the joint, then mounted, polished, and etched. The specimens were etched by Vilella's reagent which can bring out pearlite, bainite and martensite very well. The etching time, varying with the specimen welded condition, is about 10 to 20 seconds. The microstructures were examined using optical microscopes and a scanning electron microscope. For the latter method, the samples must be coated to get better conduction. The object of microstructural examination is to find out whether the microstructures of pearlite, bainite and martensite or their mixtures are present or not. The relative amount that the microstructures change is to be compared with the various post-weld heating schedules.

7.2. Microstructure Observation on the Weld Specimens

The photographs in Fig. [7-1] to [7-8], taken from optical microscopes and the scanning electron microscope are microstructures of actual welded specimens which have undergone different post-weld heating cycles.

Fig.[7-1a,b] show a sample where no post-weld heat was applied. In this case, the microstructure is almost purely martensite as shown in Fig.[7-1b]. The intercritical region is relatively narrow, only about 0.4 mm. Also, the grain size of pearlite and bainite in this region is very fine as shown in Fig.[7-1a] and difficult to distinguish from each other even at a high magnification.

It is apparent in other photographs that the width of the intercritical grained region is increased gradually as the post-weld heating current is increased. The measured results are shown in Table [7-2]. The higher the post-weld current and the longer the post-weld current is applied, the wider the intercritical grained region. On the other hand, the

granular pearlite and bainite are also coarsening and become easy to distinguish from each other. Pearlite nodules nucleate on grain boundaries of austenite and grow with a roughly constant radial velocity into the surrounding austenite grains. From the pictures [7-4],[7-5],[7-6], it can be seen clearly that there is a tendency for the pearlite nodules to cross the corner, or edge of austenite grain boundaries where the pearlite nucleates and grows. At a smaller undercooling, below A_{e1}, the nodules grow as hemispheres or spheres without interfering with each other, as shown in Fig. [7-5] where 15 percent post-heating current was applied, and where the pearlite nodules are approximately spherical.

The higher the post-weld heating current, the slower the cooling, and the more perfect the pearlite which nucleates and develops. This is observed more clearly in the high magnification pictures taken from scanning electron microscopy Fig.[7-8a,b,c]. From Fig.[7-8a] to [7-8c], the post-weld heat is increased so that Fig.[7-8c] displays a clearly defined, although extremely fine grained pearlite microstructure.

There is another phenomenon observed in the pictures taken from heat-affected zone along the fusion line. For a lower post-heat current input, only a few small sawtooth-like bainite sheaves appear in the coarse grained or fine grained zone as shown in Figs.[7-2,3]. But as the post-weld heat is increased, the growth of bainite speeds up so that a more completely developed sawtooth-like bainite can be observed as shown in Fig. [7-5c,d], [7-6b] and [7-7]. Especially in the case of 15 percent of the welding current and in the sample which used the Coschell standard welding cycles, there is a lot of large feather- like bainite occurring around austenite grain boundaries. As we

granular pearlite and bainite are also coarsening and become easy to distinguish from each other. Pearlite nodules nucleate on grain boundaries of austenite and grow with a roughly constant radial velocity into the surrounding austenite grains. From the pictures [7-4],[7-5],[7-6], it can be seen clearly that there is a tendency for the pearlite nodules to cross the corner, or edge of austenite grain boundaries where the pearlite nucleates and grows. At a smaller undercooling, below A_{e1}, the nodules grow as hemispheres or spheres without interfering with each other, as shown in Fig. [7-5] where 15 percent post-heating current was applied, and where the pearlite nodules are approximately spherical.

The higher the post-weld heating current, the slower the cooling, and the more perfect the pearlite which nucleates and develops. This is observed more clearly in the high magnification pictures taken from scanning electron microscopy Fig.[7-8a,b,c]. From Fig.[7-8a] to [7-8c], the post-weld heat is increased so that Fig.[7-8c] displays a clearly defined, although extremely fine grained pearlite microstructure.

There is another phenomena observed in the pictures taken from heat-affected zone along the fusion line. For a lower post-heat current input, only few small sawtooth- like bainite sheaves appear in the coarse grained or fine grained zone as shown in Figs.[7-2,3]. But as the post-weld heat is increased, the growth of bainite speeds up so that a more completely developed sawtooth-like bainite can be observed as shown in Fig. [7-5c,d], [7-6b] and [7-7]. Especially in the case of 15 percent of the welding current and in the sample which used the Coschell standard welding cycles, there is a lot of large feather- like bainite occurring around austenite grain boundaries. As we know, the

know, the bainite formation closely resembles finely spaced Widmanstätten side-plates at the higher temperatures as shown in specimen Fig.[7-5c,d]. The grain boundary allotrimorphs nucleate at grain boundaries in the matrix phase and grow preferentially, and more or less smoothly, along these boundaries[7-1]. Widmanstätten sideplates (or sideneedles) are plate- or needle-shaped crystals which develop into the interior of a matrix grain from the vicinity of the matrix grain boundaries. Primary sideplates grow directly from grain boundaries in the matrix phase. Secondary sideplates develop from crystals of another morphology (but of the same phase), usually from grain boundary allotrimorphs[7-1].

From viewing of the microstructure shown in Fig.[7-7] obtained from the Coschell standard welding cycle, it is shown that the microstructure is mainly a mixture of bainite and pearlite, and there is almost no martensite present. This means that the undercooling rate is slowed down when the post-weld heat is applied. This condition is favourable for the nucleation of pearlite and bainite to form a normalized microstructure instead of quenched martensite.

CHAPTER 8

RESULTS AND DISCUSSION ABOUT MODELLING MICROSTRUCTURE DEVELOPMENT IN RESISTANCE WELDING

8.1. Predicted IT Diagram for Steel Used in Resistance Welding Process

The IT diagram predicted by the modified Kirkaldy algorithm for the steel used in resistance welding process by Coschell Inc. is depicted in Fig. [8-1]. Fig.[8-2] corresponds to Fig. [8-1] but it delineates the volume fraction of isothermal transformation pearlite at different isothermal temperatures. These two figures give an approximate reference for cooling rates and metallurgical transformations. The dashed straight line which is tangent line of the start C-curve (1%) predicts the approximate cooling rate needed to avoid the formation of martensite.

8.2. Effect of Post-weld Heating on Temperature Distribution and Microstructure Development

To find a best post-weld heat condition, a series of post-weld heat schedules to study the effect of different post-weld heats on the temperature distribution and microstructure development in the HAZ was set up. The post-weld heat applied to the weld includes two aspects: (a) Comparing the algorithm predictions of microstructure development with the results obtained from the actual experimental observation from the Coschell runs (Table 7-1), the reliability of the computer modelling can be assessed.

(b) Inventing various new trial conditions; a set of 16 different possible post-heat weld currents schedules was designed as shown in the Table [8-1]. From running these results, a suitable post-weld heat schedule can be developed.

8.2.1. Effect of Post-weld heating on Temperature Histories

The effect of post-weld heating on temperature is dependent on the magnitude of the post-weld heating current and how long it is applied. The modelling results focus on a few selected nodes. Fig.8-3 shows the nodal positions and symbols of the selected nodes in the HAZ of the geometric model. The results of modelling the temperature histories on cooling for selected nodes with different applied post-weld heats are shown in part (a) of the Figs. [8-4] to [8-25]. These figures describe the cooling curves over certain temperature ranges. As mentioned before, the purpose of supplemental post-weld heat is to slow down the cooling rate in the HAZ to promote austenite decomposition into more pearlite and bainite. This means that the temperature should be kept in the temperature range between the pearlite start temperature P_s (986.8 K) and martensite start temperature M_s(508.0 K) long enough for all the austenite to decompose.

From the results of temperature distribution for selected nodes in Fig.[8-4] to [8-25], we can see that the profile of the cooling curves strongly depends on the post-heating input schedule and peak temperature reached in the HAZ of the weld. At a lower post-weld heat input, 10% and 15% of welding current, the temperature profiles show that the cooling curve becomes more flat, compared with no post-weld heat. As the length of time of the post-weld heat application increases, the change of the cooling curve profile becomes more obvious. This indicates that the cooling rate between the P_s and

M_s is reduced; the time during which the temperature stays in this range is increased. At a higher level of post-weld heat input, 20%, or 30% of the welding current, it is noticed that there is an early temperature increase creating a peak in the cooling profiles. When the post-weld heat is 20% of welding current, the peaked curve is lower. As the post-weld current is increased, the peaked curve is increased and widened significantly. The corresponding temperature is extremely high. The weld is overheating and will cause some of the austenite grains to coarsen. This is not desirable because the increase of austenite grain size will move the C-curves towards longer transformation time, and make it more difficult to avoid the formation of martensite.

Returning to the set of calculations done parallel with real weld samples, it has been observed that 5% of welding current as the post-weld heat input is too low, so that the temperature profiles are almost same as the no post-weld heating.

For the case of the Coschell standard welding cycle, the computer simulation suggests that the post-weld heat is a little high, since there exists a small peak in the curve. As well, the simulation predicts that the interior HAZ nodes will be martensite, although the micrographs show that these are, in fact, a pearlite-bainite mixture.

In finding an optimum post-weld heat schedule, it is important to remember that each node has a different thermal history so that the influence of post-weld heat on each node will be different as shown in these cooling profiles The temperature for the nodes near the centre part of the HAZ such as [2,16], [3,16], [4,16] and [5,18] are higher than others so that they experience a higher undercooling rate in the P_s-M_s range. Also, the austenite grain size for these nodes are bigger than others so that it is more difficult for

these nodes to form pearlite or bainite structures. During overheating, the maximum temperature is located at these nodes.

From computer modelling results, we can conclude that the post-weld heat should be carefully controlled, and lower and longer post-weld current input is preferred. Significant post-weld temperature increase should be prevented, especially on the nodes near the central part of the HAZ. Therefore, the suitable post-weld heat condition for this resistance welding is chosen to be around 10%-15% of the welding current and the preferred time of application is 700-750 cycles.

8.2.2. Effect of Post-weld Heating on Austenite Decomposition

The results of modelling microstructure development on the cooling stage are shown Figs.(b) and (c) of [8-4] to [8-25]. These curves represent the volume fraction transformed of pearlite or bainite at selected nodes with different post-weld heat conditions. The reaction rate is related to thermal histories. It is noted that each node in the HAZ experiences a different temperature history. The main thermodynamical reaction of austenite decomposition happens when any of the temperature profiles drops down below the pearlite start temperature and it stops when the martensite start temperature is reached. Because of different thermal histories, while some nodes are undergoing an austenite decomposition reaction, others will still be in the austenitizing temperature range. Thus, in this modelling algorithm, the ratio of each volume fraction of transformed products is changed at each node as the cooling time in this temperature range is changed, depending on post-weld heat conditions. At higher cooling rates, the nucleation of pearlite or bainite are suppressed and martensite dominates the HAZ.

As the post-weld heating current or time is increased, the cooling time is kept in this temperature range longer so that the amount of pearlite and bainite increases and martensite decreases at different nodes. This happens in the case of lower post-weld current input (10%, 15% of welding current). In the case of higher post-weld current inputs (20%, 30% of welding current), increasing the post-weld heat only postpones the austenite decomposition time but the amount of pearlite or bainite transformed will not increase. If the near fusion-line nodes are still austenite at or near the end of the post-weld heat cycles, then they will quench to martensite.

Figs.[8-26] to [8-30] and Figs. [8-31] to [8-35] delineate the contour of modelling results of the pearlite and bainite distribution for the nodal points in the HAZ at the end of welding respectively. The pearlite and bainite are nucleated along the edge of the HAZ with base metal(the bottom and top of these maps). When post-weld heat is applied, the microstructural change happens around these nodes, and amount of pearlite and bainite is increased around the HAZ edge nodal points. Some nodes show an obvious change but some are only changed a little. The modelling results show that the microstructure in the centre part of the HAZ is martensite even though the post-weld heat is applied. When the post-weld heat applied is 10% and 15% of welding current for 720 cycles, there is some pearlite and bainite transformed near the centre part. It is known that the pearlite and bainite are very hard to nucleate and develop near the fusion line and centre part of the HAZ because the highest temperatures occur around fusion line due to the high contact resistance between the faying surfaces of the weld. The high temperature causes the greatest grain growth so that the austenite grain size around

centre part and fusion line is larger than other nodal points. Also, the higher temperature means that this region has a higher electrical resistance, so more heat will be generated here when the post-weld current is applied. Also, none of the diffusional reactions start until the metal cools below A_{e3}. So this region is not eligible to transform for the first part of the post-weld cycle. All this increases the difficulty of promoting austenite decomposition into pearlite and bainite in this region. Comparing the modelling results with those obtained from observation of microstructure for actual welding samples, they reflect almost the same tendency of microstructure development. Also, the chemical composition of the steel affects the formation of austenite decomposition products because they change the critical temperatures, and the inhibition of the diffusional reactions.

The results indicate that the algorithm gives a reasonable estimate of microstructural development. The accuracy is influenced by various parameters such as chemical composition, post-weld heating input, and grain size. The modelling results can be used as a reference for the design of a welding procedure. An appropriate post-weld heat schedule can be decided with the aid of a predicted IT diagram for the steel composition, modelling results, and an analysis of the grain size distribution in the martensite with no post-weld heat.

The computer simulation failed to predict the rather successful experimental results of the Coschell standard welding cycle. The reasons for this important microstructure are not known. As Coschell has gone out of business, it is no longer practicable to do more experimental work to find the causes of failure of the model for this case.

CHAPTER 9

CONCLUSIONS AND FUTURE WORK

9.1. Conclusions

The following conclusions can be presented from the present work on the modelling of microstructure development in resistance welding:

1). The austenite decomposition kinetics algorithm developed by Kirkaldy and coworkers for hardenability calculations have provided the basis for a method to predict weld HAZ microstructure development.

2). It has been shown in the present work that the transformation rate is partially controlled by the exponent part of the Kirkaldy's algorithm. By modifying the exponential part of Kirkaldy's algorithm, it has been made more suitable for modelling high carbon plain carbon steels. Using IT diagrams for a family of high carbon plain carbon steels given in the "Atlas of Isothermal Transformation Diagrams" has provided a good reference for the prediction of the behaviour of the steel used by Coschell Inc. This has allowed the most appropriate exponents for Kirkaldy's equation to be found.

3). This work demonstrates that the austenite grain size has a profound effect on the austenite decomposition into its daughter products in the heat-affected zone; the larger austenite grain size moves the IT curve towards the right so that transformation reactions will be postponed. The present work shows that the austenite grain size input

for the calculation of kinetic reaction must change with nodal position in the HAZ of our geometric model due to the different austenitizing temperatures reached.

4). Empirical equations derived from Jominy tests give a fairly good fit for the austenite grain growth rate as a function of temperature and time. These results have been applied to the HAZ obtained from the real weld samples to predict the initial temperature distribution in the HAZ at the end of welding current input stage.

5). To verify the modelling results, a series of experiments on microstructural observation were performed at Coschell and the same welding schedules were modelled in the simulation. Both sets of results are generally in agreement with each other.

6). Making use of the finite-difference method, the model is able to predict the temperature distribution, as well as microstructure development in the HAZ of resistance welded crossed bars for the type of steel used by Coschell Inc. These simulation results suggest that a lower post-weld current (about 10 to 15% of welding current) held for a longer time is preferable in the design of a post-weld heat schedule. Higher post-weld current can result in the reaustenitization of the HAZ.

9.2. Suggestions for future work

In order to achieve the optimum modelling results for microstructure development, the following study is recommend:

1). The accuracy of the kinetic algorithm can be improved further if we can set the exponent part in the algorithm that is a function of manganese content and other alloying elements.

2). More experiments on austenization have to be carried out to obtain austenite

austenitizing temperature (higher than 1367 K) in order to evaluate the general applicability of the empirical equation derived from the Jominy tests. Ideally, these experiments would be carried out in a salt bath on very thin samples.

3). An analysis of the thermal stresses developed due to differential expansions and contractions, as well as transformational volume changes, would provide more insight into the cracking problem.

REFERENCES

Chapter 1

1-1. AWS: **Resistance Welding -- Theory and Use**,Chapman & Hall, Ltd., London, pp.29, (1956).

1-2. Obering, Lorenz Preifer, Frankfurt/Main, *"Resistance Welding-A: Well-tried Method for a Wide Variety of Applications"*, **Welding and Cutting**, Jan, pp.E6, (1986).

1-3. G. E. Linnert, **Welding Metallurgy**, Vol. 2, pp.141, American Welding Society, N.Y., (1967).

1-4. K. Easterling, **Introduction to the Physical Metallurgy of Welding**, pp.104, Butterworths & Co(Publishers) Ltd.,(1983).

1-5. R. M. Denys, *"Fracture Control and Local Brittle Zones, A General Appraisal"*, **Welding Failure**, London, England, Nov. 21-24, (1988).

1-6. A.M Jorsfield and J. L P. Hilkes, *"Weld metal Cracking-Some Suggested Causes and Cures"*, **Welding Failure**, London, England, Nov. 21-24, (1988).

1-7. J. S. Kirkaldy and D. Venugopalan, *"Prediction of Microstructure and Hardenability in Low Alloy Steel"*, **Phase Transformations in Ferrous Alloys**, (edited by A. R. Marder and J. I. Goldenstein), Am. Inst. Min. Engrs, Philadelphia, pp 125-148, (1984).

Chapter 2.

2-1. H. B. Cary, **Modern Welding Technology**, Chapter 8, pp. 241, 2nd Edition, Prentice Hall, Englewood cliffs, New Jersey 07632, (1989).

2-2. H. A. Nied, "*Weld Pool Geometry Predictions Using A Two-dimensional Heat Flow Model*", **Advances in Welding Society and Technology**, pp. 21, (1986).

2-3. D. Rosenthal, "*Mathematical Theory of Heat Distribution During Welding And Cutting*", **Welding Journal**, pp. 220, (1941).

2-4. D. Rosenthal, "*The Theory of Moving Source of Heat and Its Application to Metal Treatments*", **ASME Trans.**, Vol. 11, pp 849-866, (1946).

2-5. V. Pavelic, R. Tanbakuchi, O. A. Uyehara, and P. S. Myers, "*Experimental and Computed Temperature Histories in Gas Tungsten-Arc Welding of Thin Plates*", **Welding Journal**, Vol 48, PP 295s-305s, 1969.

2-6. C. L. Tsai, "*Finite Source Theory*", **Proceedings 1983 Engineering Conference: Modelling of Casting and Welding Process**, Mew England College, Henniker, NH, pp. 329, (1983).

2-7. C. C. Doumanidis, M. Hale and D.Hardt, "*Multi-variable Control of Arc Welding Process*", **Advances in Welding Society and Technology**", **TWR'86, Procedding of an international Conference on Trends in Welding Research**, Gatlinburg, Tennessee, pp 449-460, (1986).

2-8. C. C. Doumanidis and D. E. Hardt, "*A Model for In-Process control of Thermal Properties During Welding*", **Transaction of the ASME**, Vol. 111, pp. 40-50, (1989).

2-9. O. R. Myhr and O. Grong, "*Dimensionless Maps for Heat Flow Analysis in Fusion Welding*", **Acta Metall.**, Vol. 38, No.3, pp 449-460, (1990).

2-10. J. Mckelliget and J. Szkely, "*Heat Transfer and Fluid in the Welding Arc*",

Metall. Trans., Vol. 17a, pp. 1139-1148, (1986).

2-11. M. Salcudean, M. Cho and R. Greif, "*A Study of Heat Transfer During Arc Welding*", Int. J. **Heat Mass Transfer**, Vol. 29, No. 2, pp. 215-225, (1986).

2-12. R. Ule and Y. Joshi, "*Three dimensional Transient Heat Transfer Computations of Autogenous Arc Welding*", **National Heat Transfer Conference, HTD-Vol. 113, Heat Transfer in Manufacturing and Materials Processing**, pp. 131-141, (1989).

2-13. L. Goldak, M. Mcdill, A Oddy, R. House, X Chi, M. Bibby, "*Computational Heat Transfer for Weld Mechanics*", **Advances in Welding Society and Technology", TWR'86, Proceeding of an international Conference on Trends in Welding Research**, Gatlinburg,Tennessee, pp 15-20, (1986).

2-14. E. K. Asibu and N. Kikuchi, "*Experimental Finite Element Analysis of Temperature Distribution During Arc Welding*", **Sensors and Controls for Manufacturing 1988**, pp 1-15, (1988).

2-15. G. R. Archer, "*Calculations for Temperature Response in Spot Welds*", **Welding J.**, 39 (8), pp. 327s-330s, (1960).

2-16. J. A. Greenwood, "*Temperature in Spot Welding*", **Brit. Welding J.**, H.6,S., pp 316-322, (1961).

2-17. J. G. Kaiser, G. J. Dunn and T. W. Eagar, "*The Effect of Electrical Resistance on Nugget Formation During Spot Welding*", **Welding J.**, June, pp. 169s-174s, (1982).

2-18. J. E. Gould and P. H. Chang, "*Thermal Modelling of Spot Welds*", **Metals J.**, May, pp. 39-42, (1986).

2-19. J. E. Gould, "*An Examination of Nugget Development During Spot Welding, Using Both Experimental and Analytical Techniques*", **Welding J.**, Jan., pp. 1s-10s, (1987).

2-20. H. S. Cho and Y. J. Cho, " *A Study of the Thermal Behaviour in Resistance Spot Welds*", **Welding J.**, June, pp 236s-244s, (1989).

2-21. C. L. Tsai and D. Dickinson, "*Study of Nugget Formation in Resistance Spot Welding Using Finite Element Method*", **Recent Development Trend in Welding**, pp. 43, (1989).

2-22. Z. Han, J. Orozco, J. E. Indacochea and C. H. Chen, "*Resistance Spot Welding: A Heat Transfer Study*", **Welding J.**, Sept. pp 363s-371s, (1989).

2-23. G. P. Reddy, "*Simulation of the Spot Welding Process*", **Recent Development Trend in Welding**, pp. 59, (1989).

2-24. H. A. Nied, "*The Finite Element Modelling of the Resistance Spot Welding Process*", **Welding J.**, April, pp 122s-132s, (1984).

2-25. E. F. Nogotov, **Application of Numerical heat Transfer**, Hemisphere Publishing Corporation, Washington, London, (1978).

2-26. P. I. Frank and P. D. David, **Fundamentals of Heat Transfer**, John Wiley & Sons, Inc, (1981).

2-27. G. Krauss, **Principles of Heat Treatment of Steel**, pp 85, ASM, Metals Park, Ohio 44073, (1980).

2-28. G. R. Speich and A.Szirmae, "*Formation of Austenite from Ferrite and Ferrite-Carbide Aggregate*", **Trans TMS AME**, Vol 245, pp 1063-1074, (1969).

2-29. R. R. Judd and H. W. Paxton, "*Kinetics of Austenite Formation forma Spheroidized Ferrite-Carbide Aggregates*", **Trans. TMS-AIME**, Vol 242, pp. 206-215, (1968).

2-30. U. R. Lenel, "*TTT Curves for The Formation of Austenite*", **Scripta Metall.**, Vol. 17, pp. 471-474, (1983).

2-31. R. F. Mehl, and W. C. Hagel: Progress in Metal Physics, pp. 74-134, (1956).

2-32. C. Henwood, M. Bibby, Joldak, D. Watt, "*Coupled Transient Heat Transfer Microstructure Weld Computations*", **Acta Metal.**, Vol. 36, (1988).

2-33. H. Aaronson, "*The Proeutectoid Ferrite and the Proeutectoid Cementite Reaction*", **Decomposition of Austenite by Diffusional Process**, Edited by V. Zackay and H. Aaronson, PP. 387, Interscience Publisher, Inc., New York, (1962).

2-34. D. A. Porter and K. E. Easterling, "**Phase Transformation in Metals and Alloys**", Van Nostrand Reinhold (UK) Co. Ltd., pp. 326, (1984).

2-35. J.W. Cahn and W. C. Hagel, "*Theory of the Pearlite Reaction*", **Decomposition of Austenite by Diffusional Processes**, Edited by H. I. Aaronson, pp. 131, (1962).

2-36. M. Hillert, "*The Formation of Pearlite*", **Decomposition of Austenite by Diffusional Processes**, Edited by H. I. Aaronson, pp. 197, (1962).

2-37. J. F. Lancaster, **Metallurgy of Welding**, Third Edition, pp. 119. George Allen & Unwin Ltd., 40 Museum Street, London, (1980).

2-38. J. W. Christian, **The Theory of Transformation in Metals and Alloys**, Pergamon Press Oxford, London, Edinburgh, New York, (1975).

2-39. H. K. D. H. Bhadeshia and D. V. Edmonds, "*The Mechanism of Bainite Formation in Steels*", **Acta Metall.**, Vol. 28, pp. 1265-1273, (1980).

2-40. G. R. Purdy and M. Hillert, "*On the Nature of the Bainite Transformation in Steels*", **Acta Metall.**, Vol. 32, PP. 823, (1984).

2-41. P. G. Shewmon, **Transformations in Metals**, pp. 240, McGraw-Hill Book Company, (1969).

2-42. R. W. K. Honeycombe, **Steels; Microstructure and Properties**, pp 34, Edward Arnold Ltd., (1981).

2-43. G. E. Linnert, "**Welding Metallurgy; Carbon and Alloy Steels**", Vol. 1, pp. 350, AWS, (1965).

2-44. D. A. Porter and K. E. Easterling, "**Phase Transformation in Metals and Alloys**", Van Nostrand Reinhold (UK) Co. Ltd., pp. 334, (1984).

2-45. H. I. Aaronson and H. A. Domian, "*Partition of Alloying Elements Between Austenite and Proeutectoid or Bainite*", **Trans. AIME**, Vol. 236, pp. 781, (1966).

2-46. M Avrami, J. Chem. Phys., vol. 7, pp. 1103-12, (1939), and Vol. 8, pp. 212-24, (1940).

2-47. W. A. Johnson and R.F. Mehl, **Trans. AIME**, Vol. 135, pp. 416, (1939).

2-48. J. S. Kirkaldy and D. Venugopalan, "*Prediction of Microstructure and Hardenability in Low Alloy Steel*",**Phase Transformations in Ferrous Alloys**, (edited by A. R. Marder and J. I. Goldenstein), Am. Inst. Min. Engrs, Philadelphia, pp. 125-148, (1984).

2-49. J. S. Kirkaldy, "*Prediction of Alloy Hardenability from Thermodynamic and Kinetic Data*", **Metall. Trans.**, Vol 4, Oct., pp. 2327-2333, (1973).

2-50. J. S. Kirkaldy and R. C. Sharma, "*A New Phenomenology for Steel IT and CCT*

Curves", **Scripta Metall.**, Vol. 16, pp. 1193, (1982).

2-51. J. W. Cahn, "*Transformation Kinetics During Continuous Cooling*", **Acta Metall.**, Vol. 4, pp. 572-575, (1956).

2-52. H. K. D. H. Bhadeshia, "*Thermodynamic Analysis of Isothermal Transformation Diagrams*", **Metal Science**, Vol. 16, PP. 159-165, (1982).

2-53. K. C. Russell, "*Linked Flux Analysis of Nucleation in Condensed Phases*", **Acta Metall.**, Vol. 16, pp. 761, (1968).

2-54. K. C. Russell, "*Grain Boundary Nucleation Kinetics*", **Acta Metall.**, Vol. 17, pp. 1123, (1969).

2-55. M. F. Ashby and K. E. Easterling, "*A First Report on Diagrams for Grain Growth in Welds*", **Acta Metall.**, Vol. 30, pp. 1969-1978, (1982).

2-56. J. C. Ion, K. E. Easterling and M. F. Ashby, "*A Second Report on Diagrams of Microstructure and Hardness for Heat-Affected Zones in Welds*", **Acta Metall.**, Vol. 32, pp. 1949-1962, (1982).

2-57. L. Coon and D. F. Watt, "*Simulation of Weld HAZ Microstructural Development*", **Computer Modelling of Fabrication Processes and Constitutive Behaviour of Metal**, (Edited by J. Too), pp. 467-486, CANMET, Ottawa, (1987).

2-58. D. F. Watt, L. Coon, M. Bibby, J. Goldak and C. HenWood, "*An Algorithm for Modelling Microstructural Development in Weld Heat-Affected Zones: (Part A) Reaction Kinetics*", **Acta Metall.**, Vol. 36, (1988).

2-59. H. K. D. H. Bhadeshia, "*A Model for the Development of Microstructure in Low-alloy Steel(Fe-Mn-Si-C) Weld Deposits*", **Acta Metall.**, Vol. 33, pp. 1271-1283,

(1985).

2-60. H. V. Atkinson, "*Theories of Normal Grain Growth in Pure Single Phase Systems*", **Acta Metall.**, Vol. 36, pp. 469-491, (1988).

2-61. See reference 1-4.

2-62. J. E. Burke and D. Turnbull, **Prog. Metal Phys.**, Vol. 3, pp. 220, (1952).

2-63. P. Feltham and G. J. Copley, "*Grain Growth in α-Brasses*", **Acta Metall.**, Vol. 6, pp. 539-542, (1958).

Chapter 3

3-1. AMS, "*Physical Properties*", **Metal Handbook**, 9th Edition, pp.151, (1988).

3-2. The British Iron and Steel Research Association, "*Physical Constant of Some Commercial Steels at Elevated Temperatures*", Butterworths, London, (1963).

3-3. L. Coon and D. F. Watt, "*Simulation of Weld HAZ Microstructure Development in Computer Modelling of Fabrication Processes and Constitutive Behaviour of Material*", (edited by J. Too), pp. 467-468 CANMET, Ottawa, 1987.

3-4. AWS, **Welding Handbook:** *Resistance and solid-State Welding and Other Joining Processes*, 7th Edition, Vol. 3, pp. 3, (1980).

3-5. See reference 2-27, pp. 71.

3-6. F. Kreith and M. S. Bohn, **Principles of Heat Transfer**, 4th Edition, Harper & Row, Publishers, New York, pp. 56, (1986).

Chapter 4

4-1. ASTM: " *Standard Method for End-Quench Test for Hardenability of Steel*", Designation: A255-88.

4-2. R. Millsop, "*A Survey of Austenite Grain Size Measurements*", **Hardenability Concepts with Applications to Steels**, TMS-AIME, Warrendale, Pa., pp. 316-333, (1978).

4-3. ASM, "*Metallographic Technique for Carbon and Alloy Steels*", **Metal Handbook**: Vol.9, p.61, (1988).

4-4. G. A Dreyer, D.E. Austin an W. D. Smith, "*New Etchant Brings out Grain Boundaries in Martensite Steels*", **Metal Progress**, Vol. 86, p. 116-117, (1964).

4-5. ASTM, "*Standard Test Methods for Determining Average Grain Size of Metals*", Designation E112-88, (1988).

4-6. E. C. Bain and J. R. Vilella, "*Austenite Grain Size in Steel*", pp. 399.

4-7. G. E. Dieter, **Mechanical Metallurgy**, 3rd Edition, pp. 191, McGraw-Hill Book Company, (1986).

4-8. See reference 2-37, pp. 121.

4-9. R. E. Reed-Hill, **Physical Metallurgy Principles**, 2nd Edition, pp. 711, D Van Nostrand Company, (1973).

4-10. H. G. Pisarski and P. L. Harrison, "*Influence of Post-weld Treatment on the HAZ Fracture Tougness of Two Structural Grade Carbon Manganese Steels*". **7th International Conference on Offshore Mechanics and Arctic Engineering**, Houston, Texas, Feb. 7-12, pp. 199-206, (1988).

Chapter 5

5-1. J. S Kirkaldy and E. A. Baganis, "*Thermodynamic Prediction of the A_{r_3} Temperature of Steels with Addtions of Mn, Si, Ni, Cr, Mo, Cu*", **Metall. Trans.**,

9A, pp. 495, (1978).

5-2. R.A. Grange, "*Estimating Critical Ranges in Heat Treatment of Steels*", **Met. Prog.**, (April), pp. 73-75. (1961).

5-3. J. S. Kirkaldy and D. Venugopalan, See reference 2-48.

5-4. W. Steven and A. G. Haynes, "*The Temperature of Formation of Martensite and Bainite in Low-Alloy Steels*", **JISI**, Vol. 183, pp. 349, (1956).

5-5. J. S. Kirkaldy and R. C. Sharma, "*A New Phenomenology for Steel IT and CCT Curves*", **Scripta. Metall.**, Vol. 16, pp. 1193, (1982).

5-6. J. S. Kirkaldy,"*Prediction of Alloy Hardenability from Thermodynamic and Kinetic Data*", **Metal. Trans.**, Vol. 4, pp. 2327, (1973).

5-7. J. W. Cahn, "*Transformation Kinetics During Continuous Cooling*", **Acta metall.**, Vol. 4, p. 572, (1956).

5-8. M.P. Plus and J. S. Kirkaldy, "*The Pearlite Reaction*", **Met. Trans.**, Vol.3, p. 2777, (1972).

Chapter 6

6-1. W.C. Leslie, **The Physical Metallurgy of Steels**, p 257, McGraw-Hill, New York, (1981).

6-2. see ref. 2-34.

Chapter 7

7-1. H. I. Aaronson, "*The Proeutetoid Ferrite and the Proeutectoid Cementite Reaction*", **Decomposition of Austenite by Diffusional Processes**, Edited by V. F. Zackay and H. I. Aaronson,Interscience Publishers, pp. 387, (1962).

Table [4-1] Estimated grain size (GS) from Jominy Test

Temperature (K)	Time (hour)	Reported G.S.#	GS From Table (μm)	Calculated GS (μm)
1144.3	0.5	7.5	27	26.70
	1.5	6.8	34	34.02
	3.0	5.8	48	48.12
1199.8	0.5	6.4	40	39.09
	1.5	4.8	68	68.05
	3.0	4.0	90	89.81
1255.4	0.5	4.9	66	65.74
	1.5	4.2	83	83.79
	3.0	3.3	115	114.46
1310.9	0.5	3.5	105	106.80
	1.5	2.8	135	136.12
	3.0	2.0	180	179.61
1366.5	0.5	3.0	125	127.00

Table [4-2] Regression equation from Jominy Test

Temperature (K)	Regression Equation ($\times 10^{-6}$ cm^2. min)	Y-Intercept ($\times 10^{-6}$cm^2)	Slope
1144.3	$D^2 = 3.19 + 0.1071t$	3.19	0.1071
1199.8	$D^2 = 4.26 + 0.4318t$	4.26	0.4318
1255.4	$D^2 = 22.2 + 0.5925t$	22.2	0.5925
1310.9	$D^2 = 67.3 + 1.401t$	67.3	1.401

Table [4-3] Variations on the Parabolic growth equations

$$D^2 = D_o^2 + k_o \exp\left(-\frac{Q}{RT}\right)t$$

No.	D_o Determined Method	Equation Obtained	Std.
1	D_o=f(T)	$D^2=2.246*10^5\exp\left(-\frac{28966}{T}\right)+0.427\exp\left(-\frac{21892}{T}\right)t \quad (cm^2)$	9.04
2	Omit D_o	$D^2=0.427\exp\left(-\frac{21892}{T}\right)t \quad (cm^2)$	22.00
3	Fix D_o		
	Do=2μm	$D^2=4+2.5995*10^8\exp\left(-\frac{23610}{T}\right)t \quad (\mu m^2)$	13.81
	D_o=4μm	$D^2=16+2.6568*10^8\exp\left(-\frac{23675}{T}\right)t \quad (\mu m^2)$	13.73
	D_o=12μm	$D^2=144+5.1639*10^2\exp\left(-\frac{24553}{T}\right)t \quad (\mu m^2)$	13.37
	D_o=26μm	$D^2=676+3.9796*10^{11}\exp\left(-\frac{33223}{T}\right)t \quad (\mu m^2$	14.92

Table [4-4] Calculated results using parabolic grain growth equation obtained from assumed $D_o = f(T)$:

$$D^2 == D_o^2 + M \exp\left(-\frac{Qi}{RT}\right) t$$

$$where\ D_o^2 = A \exp\left(-\frac{Q_o}{RT}\right)$$

T (°K)	t (min)	D_{cal} (μm)	D_{exp} (μm)	$(D_{cal}-D_{exp})^2$	$D_{cal}-D_{exp}$	$\frac{D_{cal}-D_{exp}}{D_{exp}}$(%)
1144	1/60	15.10				
	30	24.60	26.70	4.41	2.1	7.87
	90	36.95	34.02	8.5849	2.93	8.61
	180	50.05	48.12	5.6644	2.38	4.95
1120	1/60	27.01				
	30	40.62	39.09	2.3409	1.53	3.91
	90	59.08	68.05	80.4609	8.97	13.18
	180	79.08	89.81	115.1328	10.73	11.95
1256	1/60	46.48				
	30	65.09	65.74	0.5329	0.73	1.11
	90	91.60	83.79	60.9961	7.81	9.32
	180	120.9	114.5	41.8609	6.47	5.65
1311	1/60	75.47				
	30	100.0	106.8	46.1041	6.79	6.36
	90	136.6	136.1	0.2304	0.48	0.35
	180	177.8	179.6	3.1329	1.77	0.99
1367	1/60	118.3				
	30	150.1	127.0	532.25	23.05	18.50
	90	199.0				
	180	255.3				
				Σ=898.81		Σ=92.75
				Std.Dev: 9.04		Err_{ave}: 7.13%

Table [4-5] Calculated results using parabolic grain growth Equation obtained by ignoring D_o.

$$D^2 = k_o \exp\left(-\frac{Q}{RT}\right) t$$

T (°K)	t (min)	D_{cal} (μm)	D_{exp} (μm)	$(D_{cal}-D_{exp})^2$	$D_{cal}-D_{exp}$	$\frac{D_{cal}-D_{exp}}{D_{exp}}$(%)
1144	1/60	0.45				
	30	19.49	26.70	51.9841	7.21	27.00
	90	33.76	34.02	0.0676	0.26	0.76
	180	47.75	48.12	0.1369	0.37	0.77
1120	1/60	0.72				
	30	30.34	39.09	76.5625	8.75	23.94
	90	51.96	68.05	258.8882	16.09	24.53
	180	73.48	89.81	266.6687	16.32	18.18
1256	1/60	1.07				
	30	45.45	65.74	411.6841	20.29	30.86
	90	61.97	83.79	476.1123	21.82	26.03
	180	109.0	114.5	29.8116	5.46	4.77
1311	1/60	1.55				
	30	65.75	106.8	1685.1025	41.05	38.44
	90	113.9	136.1	495.0625	22.25	16.35
	180	161.0	179.6	179.61	18.34	10.34
1367	1/60	2.17				
	30	91.98	127.0	1226.4004	35.02	38.07
	90	159.3				
	180	225.3				
				Σ=5323.33		Σ=260.04
				Std.Dev: 22.00		Err_{ave}: 20.0%

Table [4-6a] Calculated results using parabolic grain growth Equation obtained from fixing D_o = 2 μm.

$$D^2 = D_o^2 + k_o \exp\left(-\frac{Q}{RT}\right)t$$

T (°K)	t (min)	D_{cal} (μm)	D_{exp} (μm)	$(D_{cal}-D_{exp})^2$	$D_{cal}-D_{exp}$	$\frac{D_{cal}-D_{exp}}{D_{exp}}$(%)
1144	1/60	2.07				
	30	22.42	26.70	18.3184	4.28	16.03
	90	38.72	34.02	16.0	4.00	11.76
	180	54.72	48.12	43.56	6.60	43.56
1120	1/60	2.172				
	30	36.04	39.09	9.3025	3.05	7.80
	90	62.35	68.05	32.4901	5.70	8.38
	180	88.16	89.81	2.7225	1.65	1.84
1256	1/60	2.39				
	30	55.71	65.74	100.6009	10.03	15.26
	90	96.48	83.79	160.2755	12.66	15.11
	180	136.38	114.5	480.4870	21.92	19.15
1311	1/60	2.80				
	30	82.86	106.8	573.1237	29.94	22.42
	90	143.5	136.1	54.3171	7.37	5.41
	180	202.9	179.6	542.8901	23.30	12.97
1367	1/60	3.8				
	30	119.5	127.0	56.1007	7.49	5.90
	90	207.0				
	180	292.6				
				Σ=2096.28		Σ=155.75
				Std.Dev: 13.81		Err_{ave}: 11.98%

Table [4-6b] Calculated results using parabolic grain growth equation obtained from fixing D_o = 4 μm.

T (°K)	t (min)	D_{cal} (μm)	D_{exp} (μm)	$(D_{cal}-D_{exp})^2$	$D_{cal}-D_{exp}$	$\frac{D_{cal}-D_{exp}}{D_{exp}}$(%)
1144	1/60	4.03				
	30	22.60	26.70	16.81	4.10	15.36
	90	38.73	34.02	22.1841	4.71	13.84
	180	54.62	48.12	42.250	6.50	13.51
1120	1/60	4.09				
	30	36.11	39.09	8.8804	2.98	7.62
	90	62.29	68.05	33.1776	5.76	8.46
	180	88.00	89.81	3.2761	1.81	2.02
1256	1/60	4.21				
	30	55.70	65.74	100.8016	10.43	15.27
	90	96.31	83.79	156.7503	12.52	14.92
	180	136.1	114.5	470.0227	21.68	18.94
1311	1/60	4.45				
	30	82.91	106.8	570.7321	23.89	22.37
	90	143.4	136.1	52.8530	7.27	5.34
	180	202.9	179.6	542.4238	23.29	12.97
1367	1/60	4.89				
	30	119.7	127.0	54.0225	7.35	5.79
	90	207.2				
	180	293.0				
				Σ=2074.18		Σ=156.41
				Std.Dev: 13.73		Err_{ave}: 12.03%

Table [4-6c] Calculated results using parabolic grain growth equation obtained from fixing D_o = 12 μm.

T (°K)	t (min)	D_{cal} (μm)	D_{exp} (μm)	$(D_{cal}-D_{exp})^2$	$D_{cal}-D_{exp}$	$\frac{D_{cal}-D_{exp}}{D_{exp}}$(%)
1144	1/60	12.0				
	30	24.30	26.70	5.76	2.40	8.99
	90	38.51	34.02	20.16	4.49	13.20
	180	53.12	48.12	25.00	5.0	10.39
1120	1/60	12.03				
	30	36.72	39.09	5.6169	2.37	6.06
	90	61.29	68.05	45.6976	6.76	9.93
	180	85.85	89.81	15.6816	3.96	4.41
1256	1/60	12.07				
	30	55.09	65.74	96.8255	9.84	14.97
	90	95.33	83.79	133.1716	11.54	13.77
	180	134.3	114.5	392.8327	19.82	17.32
1311	1/60	12.16				
	30	84.09	106.8	515.7444	22.71	21.26
	90	144.7	136.1	72.9318	8.54	6.27
	180	204.2	179.6	606.1442	24.62	13.71
1367	1/60	12.33				
	30	121.5	127.0	30.1401	5.49	4.32
	90	209.8				
	180	296.4				
				Σ=1965.71		Σ=1965.7
				Std.Dev: 13.38		Err_{ave}: 11.12%

Table [4-6d] Calculated results using parabolic grain growth equation obtained from fixing D_o = 26 μm.

T (°K)	t (min)	D_{cal} (μm)	D_{exp} (μm)	$(D_{cal}-D_{exp})^2$	$D_{cal}-D_{exp}$	$\frac{D_{cal}-D_{exp}}{D_{exp}}$(%)
1144	1/60	26.00				
	30	29.19	26.70	6.2001	2.49	9.33
		34.71	34.02	0.4761	0.69	2.03
	180	41.63	48.12	42.1201	6.49	13.48
1120	1/60	26.03				
	30	36.76	39.09	5.4289	2.33	5.96
	90	51.97	68.05	258.5665	16.08	23.63
	180	68.75	89.81	443.5235	21.06	23.45
1256	1/60	26.02				
	30	54.56	65.74	124.9924	11.18	17.01
	90	87.06	83.79	10.6929	3.27	3.90
	180	120.3	114.5	34.5744	5.88	25.14
1311	1/60	26.07				
	30	87.93	106.8	356.6770	18.87	17.67
	90	147.8	136.1	136.1889	11.47	8.57
	180	207.4	179.6	796.3685	28.22	15.71
1367	1/60	26.21				
	30	143.0	127.0	257.2814	16.04	12.63
	90	245.0				
	180	345.5				
				Σ=2447.3		Σ=158.51
				Std.Dev: 14.92		Err_{ave}: 12.19%

Table [4-7] Estimated grain size number and temperature distribution along the centre line of the HAZ

Distance (mm)	Matched (G.S.#)	Reported (G.S.#)	Reported G.S.(μm)	Report Temp. (K)
2.91	-0.7	1.7	200.36	1432
2.55	1	3	127.27	1376
2.275	1.5	3.5	107.27	1354
1.95	2.5	4.5	76.17	1312
1.625	3.0	5.0	63.10	1290
1.325	3.8	5.8	48.30	1260
1.215	4	6.0	44.88	1252
1.075	4.5	6.5	37.91	1234
0.975	5	7.0	31.87	1216
0.875	5.2	7.2	29.45	1208
0.6	5.8	7.8	24.07	1188
0.3	6.2	8.2	20.81	1174

Table [7-1] Experiments on different post-weld heat input

Sample No.	Sloping Part of Post-weld heat		Horizontal part of Post-weld heat	
	Current (%Amps)	Last Time (cycles)	Current (%Amps)	Last Time (cycles)
1	0	0	0	0
2	0	0	5	180
3	0	0	5	720
4	0	0	10	720
5	0	0	15	720
6*	40-20	70	20	495
7	0	297	15	416

*Sample number 6 is the standard Coschell cycle.

Table [7-2] The results of the width of the intercritical zone change with different post-weld heating conditions

Sample No.	Post-weld heating Cycles				Width of Intercritical Zone (mm)
	Current (%)		Last Time(cycles)		
1	No		No		0.40
2	5		180		0.58
3	5		720		0.65
4	10		720		0.75
5	15		720		1.35
6	Part I	40-20	Part I	70	Mix with Fine Grained Zone (>1.35mm)
	Part II	20	Part II	495	
7	Part I	No	Part I	297	1.05
	Part II	15	Part II	416	

Table [8-1] Different post-weld heat schedules used in modelling microstructural development. Each number in the Hold Time is a separate sample.

Post-weld heat Current (%)	Hold Time (Cycles)			
10	300	450	600	750
15	300	450	600	750
20	300	450	600	750
30	300	450	600	750

FIGURES

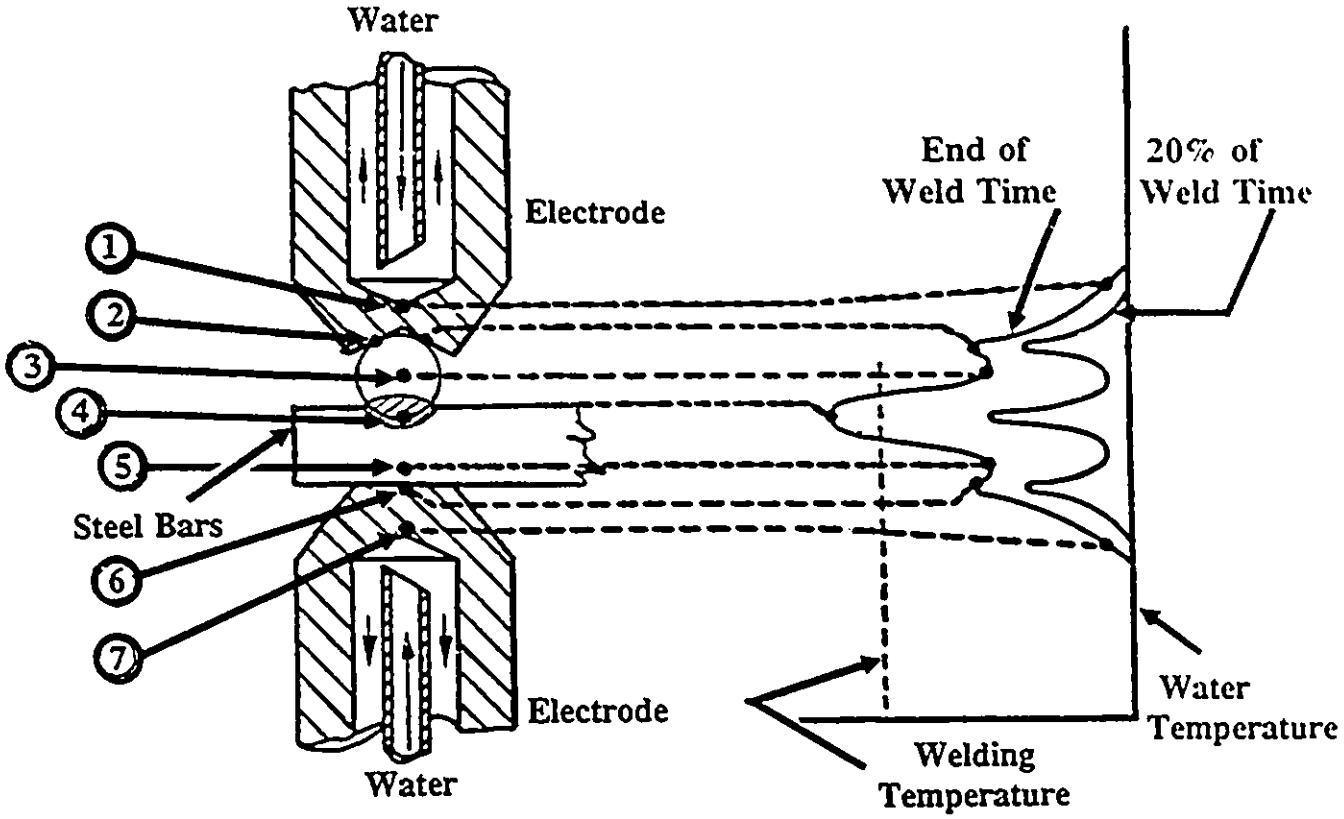

Fig. 1-1 Temperature distribution at various locations during resistance welding[1-1]

(1) and (7): The electrical resistance of the electrode material.
(2) and (6): The contact resistance between the electrode and the base metal.
(3) and (5): The resistance of the base metal itself.
(4): The base metal interface is where the weld formation starts

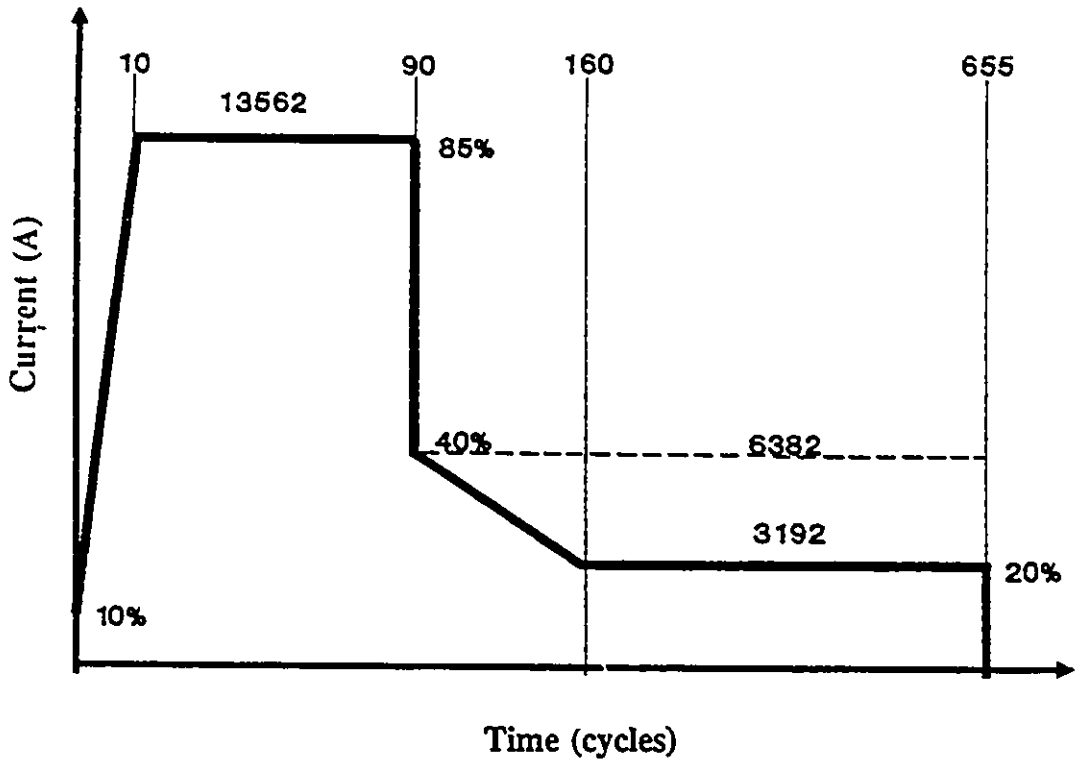

Fig. 1-2 The standard welding cycles program used by Coschell Inc.

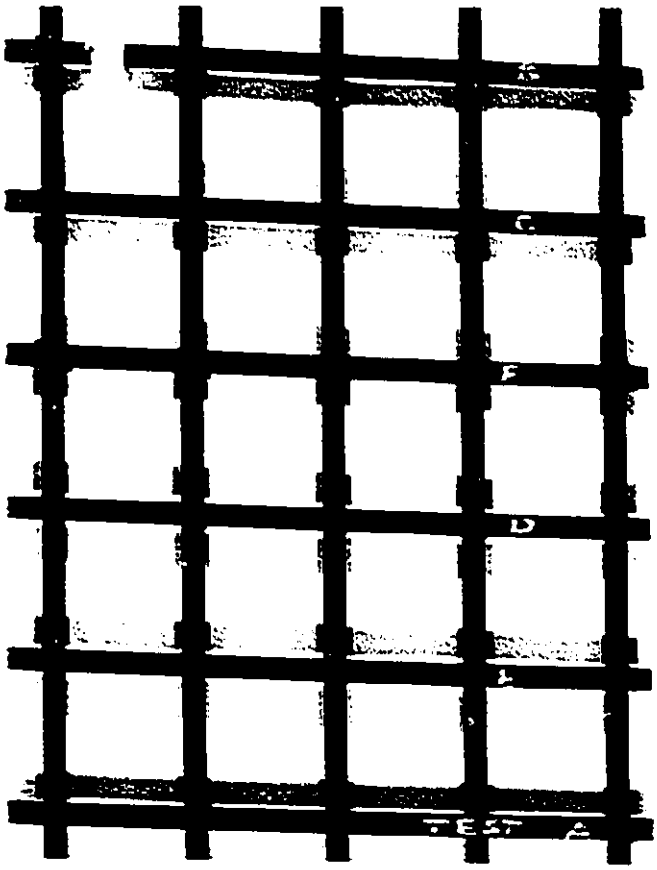

Fig. 1-3 Photograph of a resistance welded high carbon plain carbon steel wire meshes.

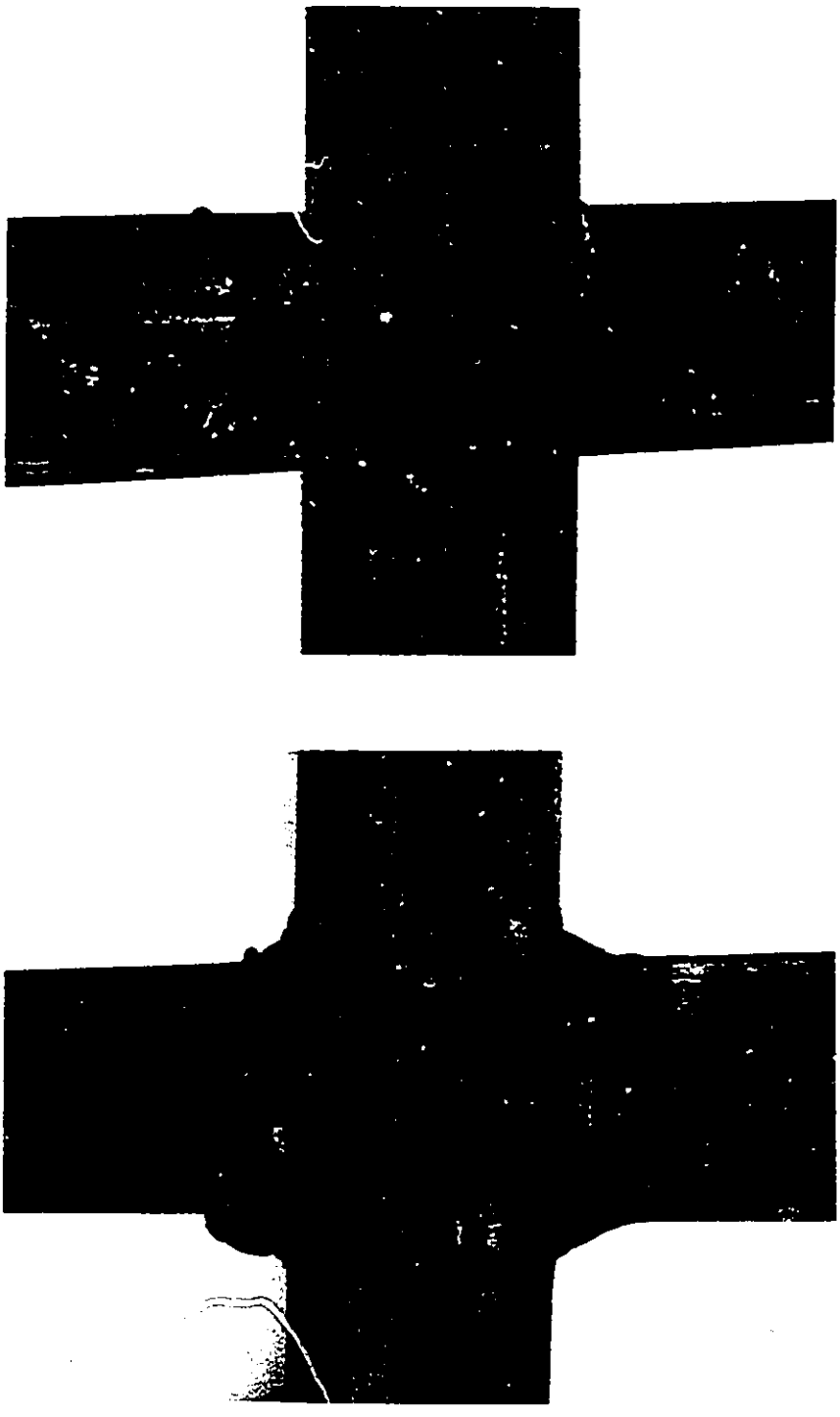

Fig. 1-4 Photograph of resistance welded joint with different post-weld heating schedules.

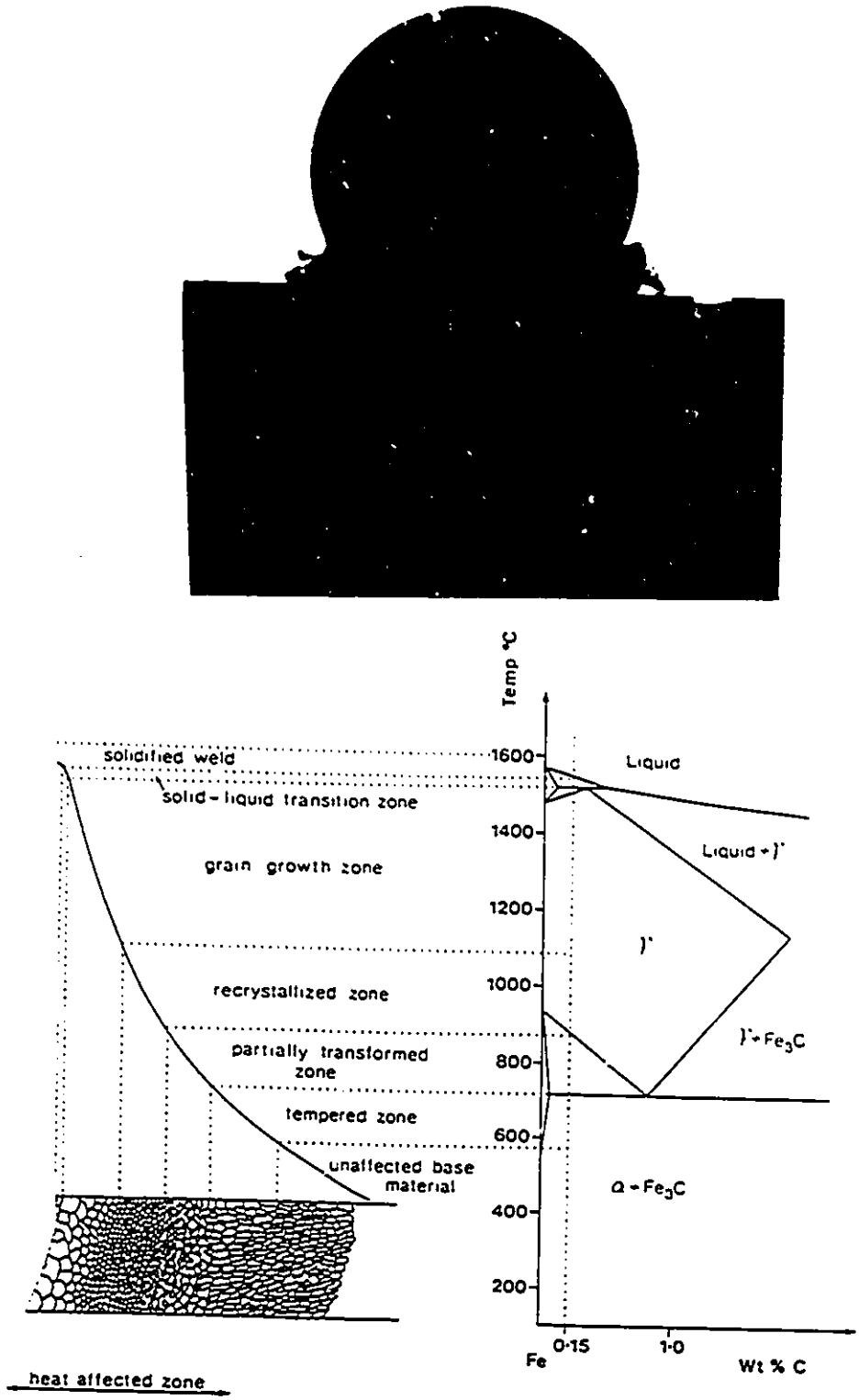

Fig. 1-5 (a) Diagram of a heat-affect zone for resistance welded bars
(b) The various sub-zones of the heat affected zone related to peak temperature indicated on an Fe-C diagram.

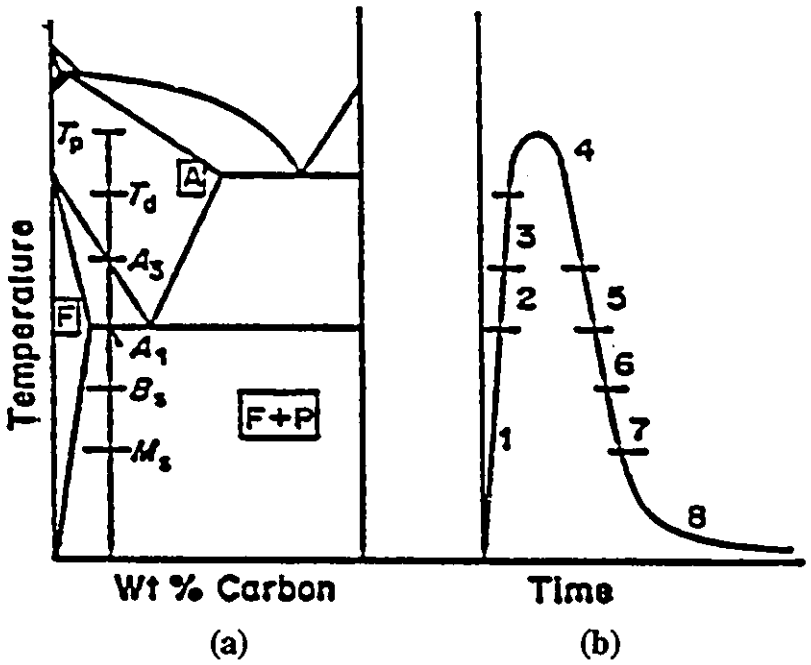

Fig. 2-1 (a) Fe-C phase diagram identifying the heating and cooling path and critical temperatures.(b) thermal cycle identifying the regions that must be considered when implementing the microstructure algorithm[2-32].

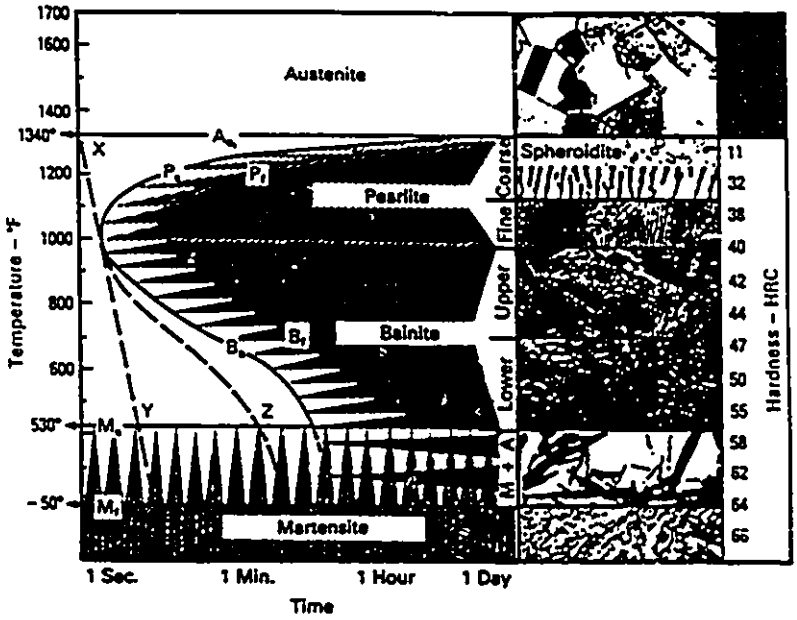

Fig. 2-2 Time-temperature-transformation diagram for a eutectoid (0.77%) carbon steel. Source: MEI Course 10, Lesson 3, American Society for Metals, p 5, 1981.

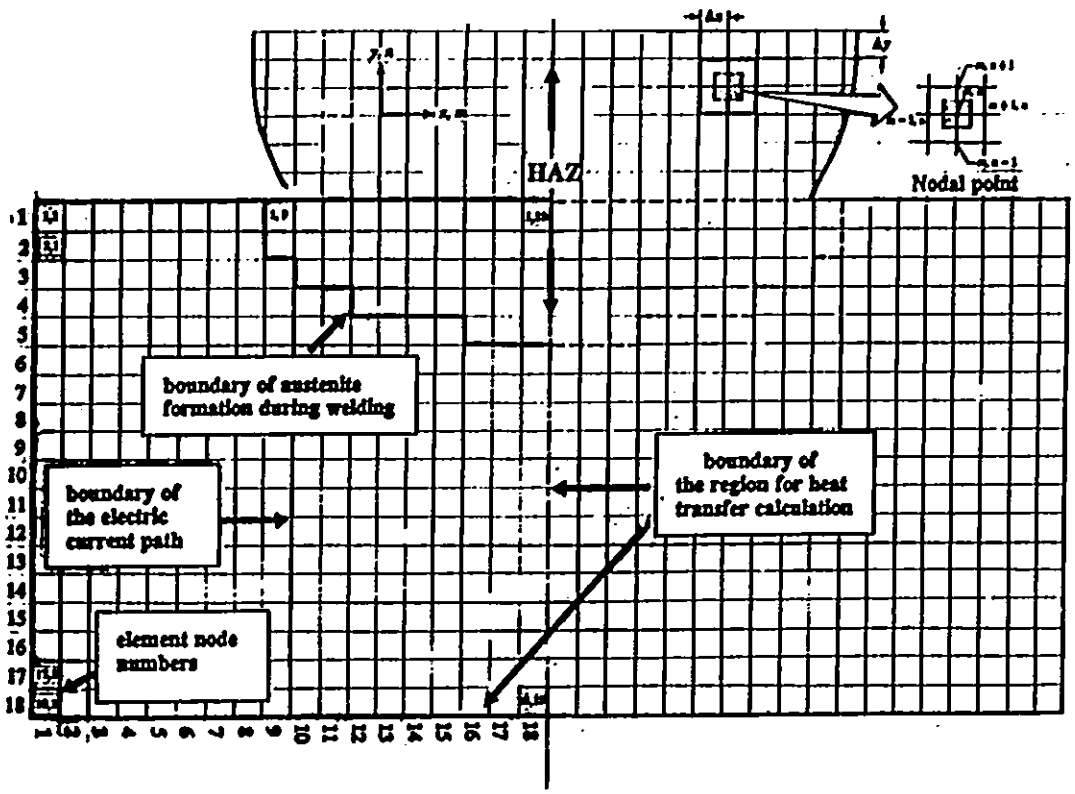

Fig. 3-1 Schematic of the finite difference model of weld microstructure.

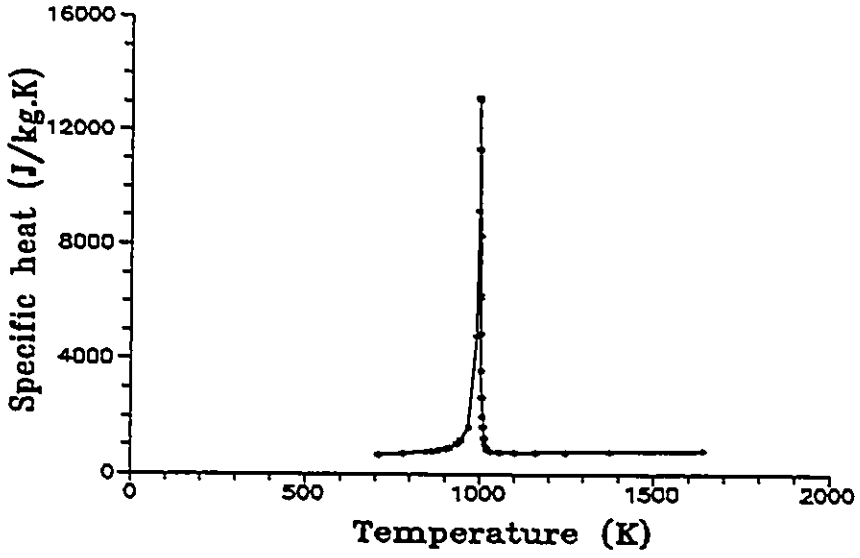

Fig. 3-2 Simulated variation of the specific heat with temperature.

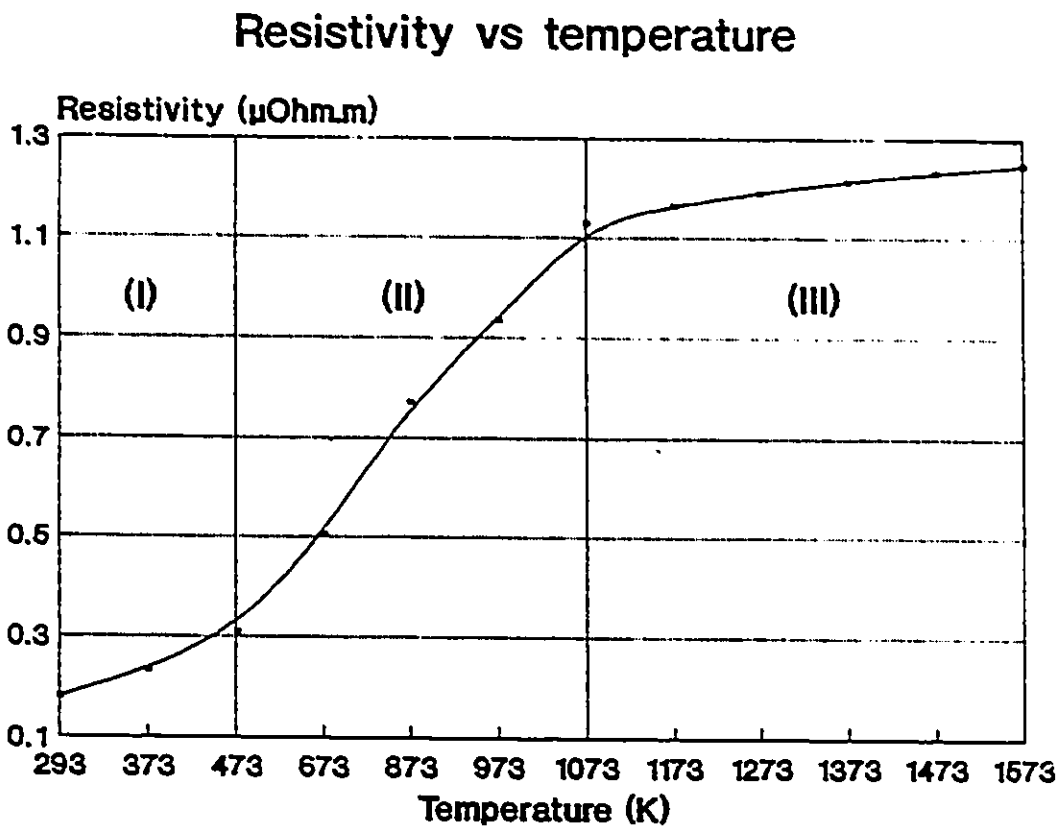

Fig. 3-3 Change in resistivity with temperature.

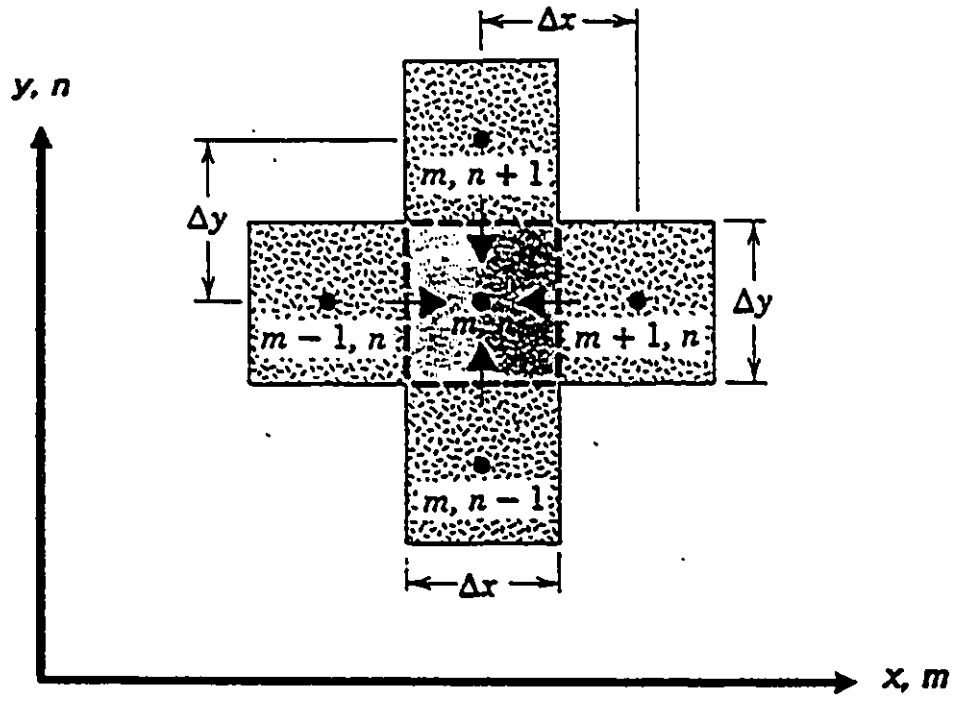

Fig. 3-4 Diagram of heat conduction to an interior node.

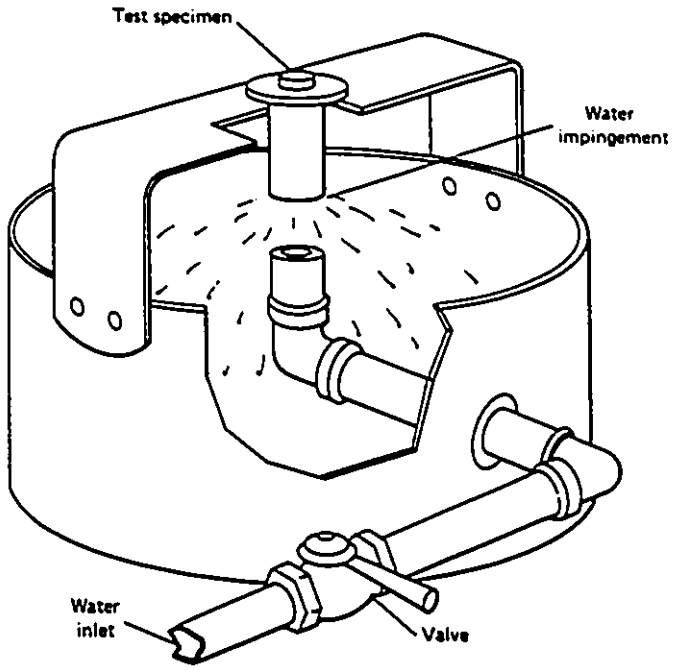

Fig. 4-1 Standard end-quench(Jominy) test specimen and method of quenching in quenching jig. Source: Heat Treaters' Guide: Standard practices and Procedures for Steel, American Society for Metals, p 21, 1982.

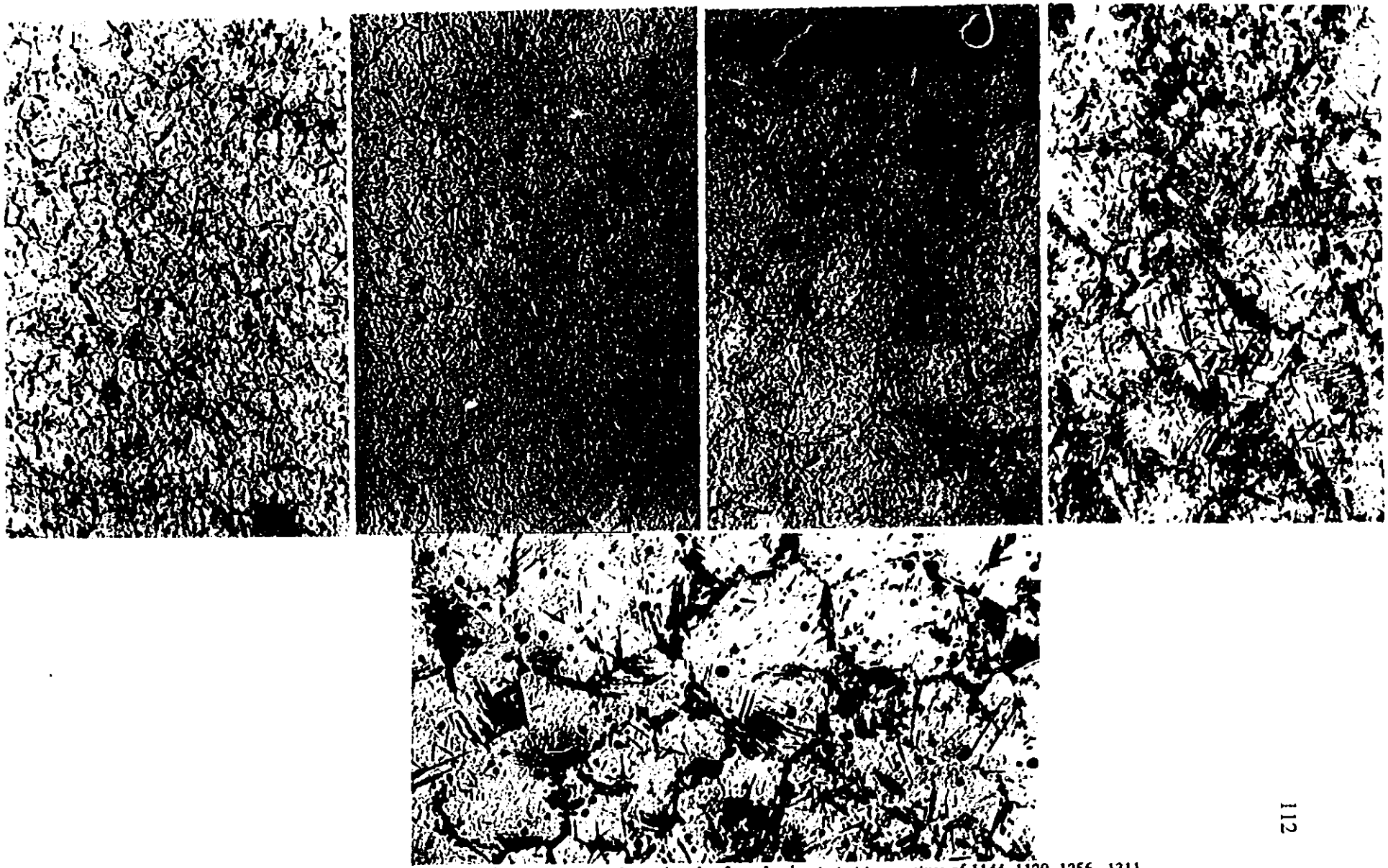

Fig. 4-2a Photographs of Measured austenite grains size from Jominy test at temperature of 1144, 1120, 1256, 1311 and 1367(°K); Hold time: 0.5 hour. Magnification, 200X.

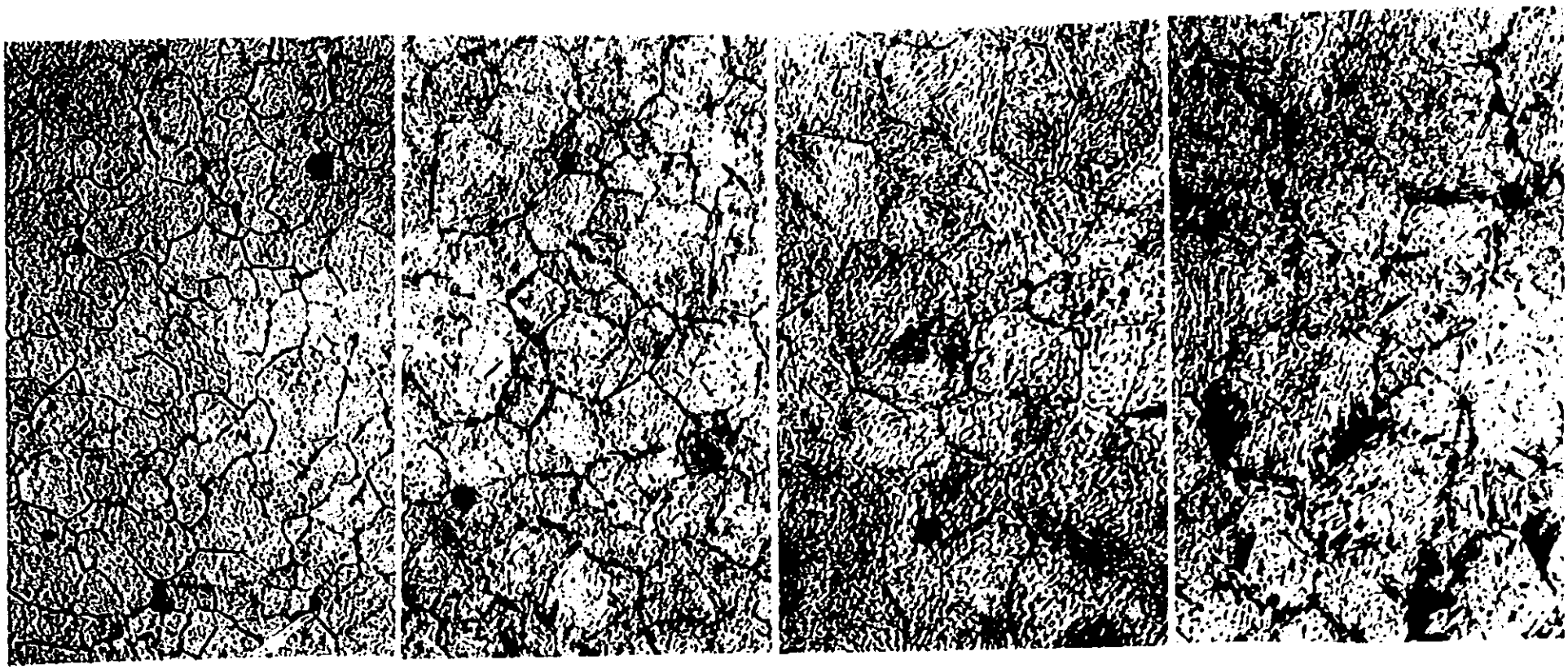

Fig. 4-2b Photographs of Measured austenite grains size from Jominy test at temperature of 1144, 1120, 1256, and 1311(°K). Hold time: 1.5 hour. Magnification, 200X.

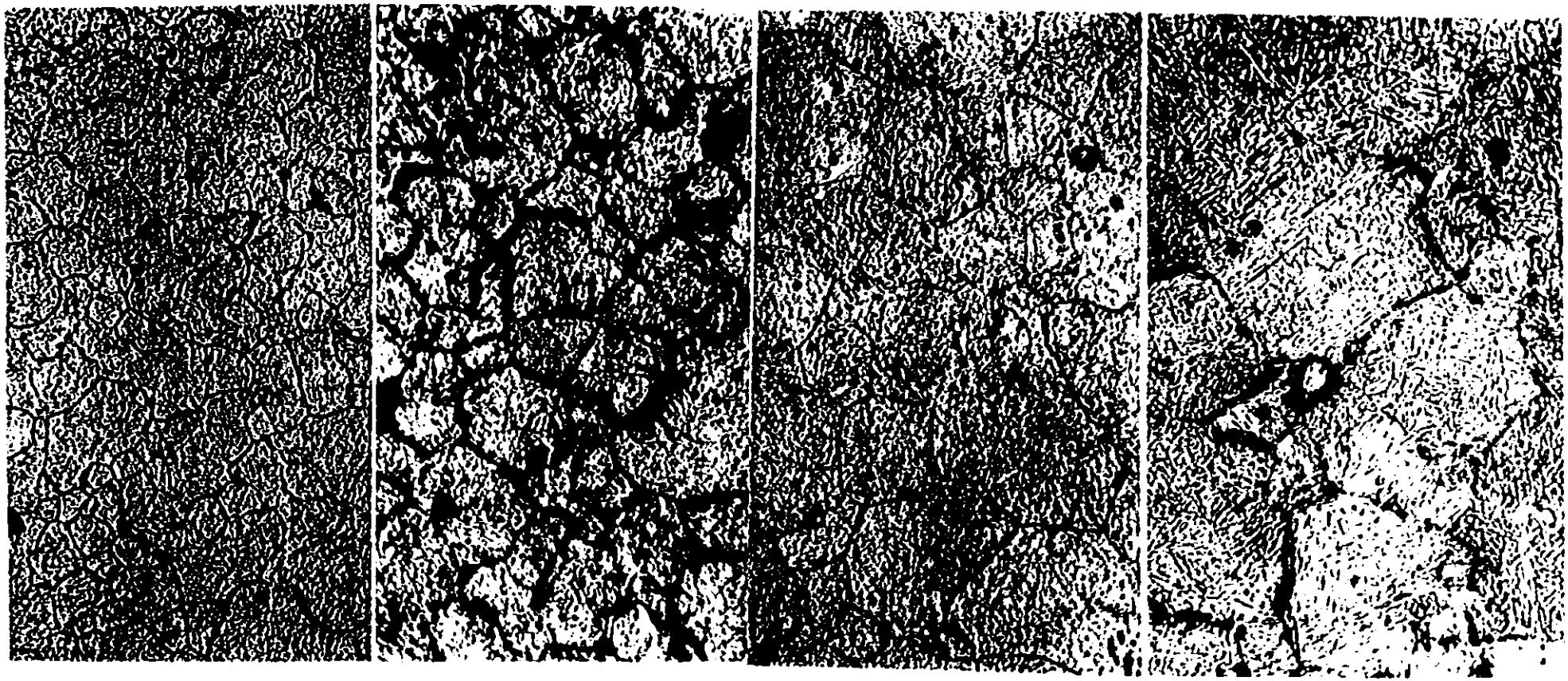

Fig. 4-2c Photographs of Measured austenite grains size from Jominy test at temperature of 1144, 1120, 1256, and 1131(°K); Hold time: 3.0 hour. Magnification, 200X.

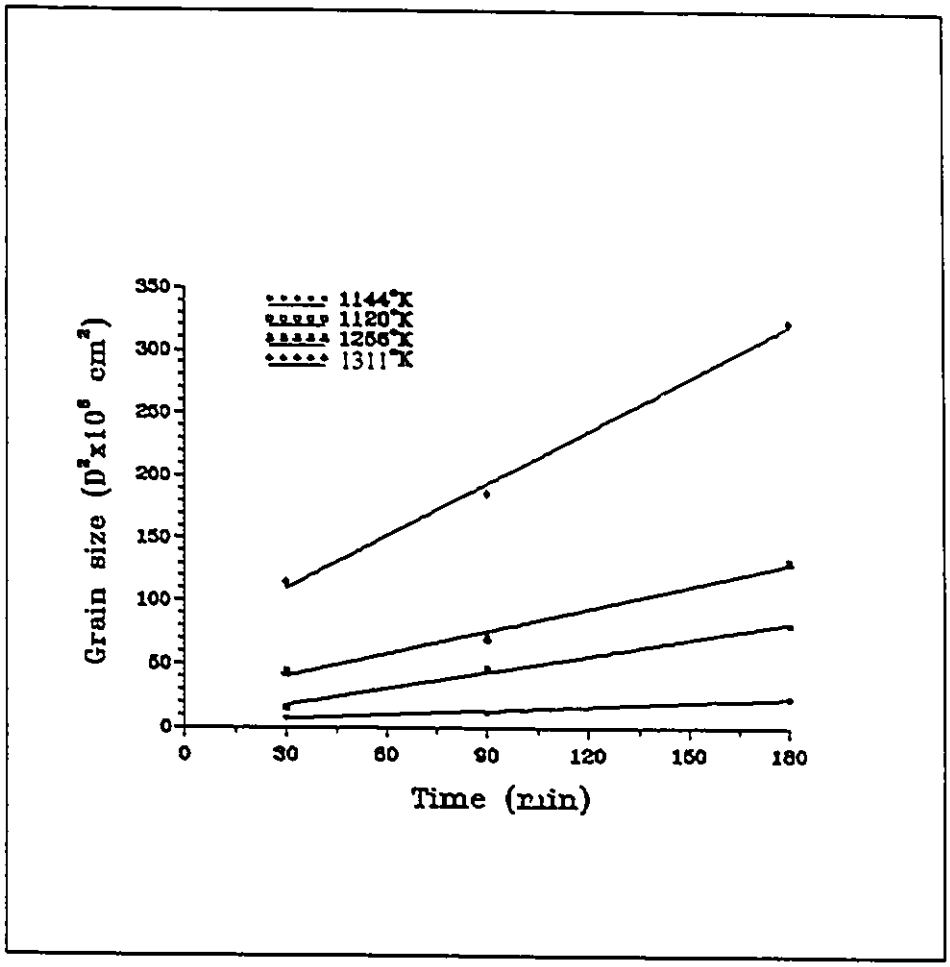

Fig. 4-3 Grain Growth results from Jominy test specimens; grain diameter (D^2) vs time.

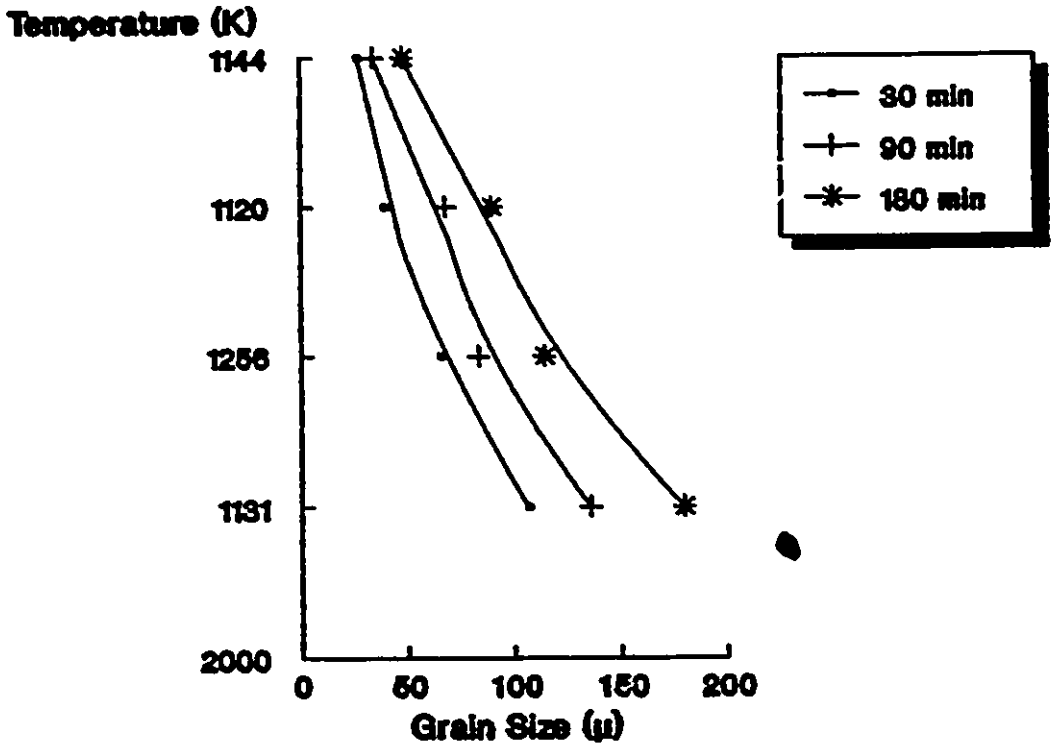

Fig. 4-4 Grain Growth results from Jominy test specimens; temperature vs grain size.

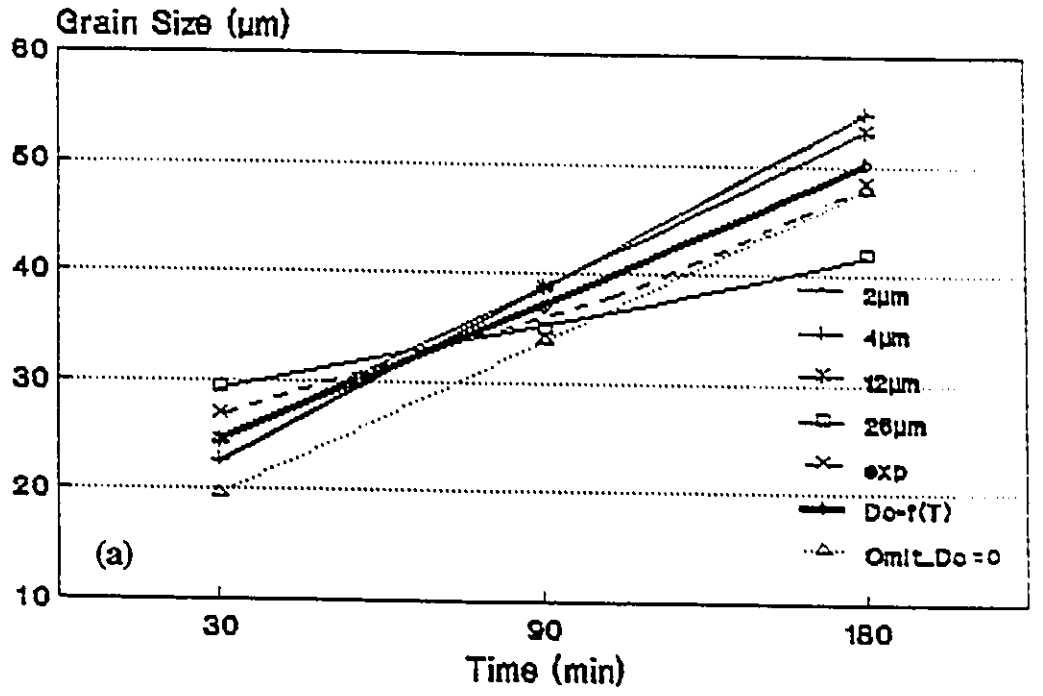

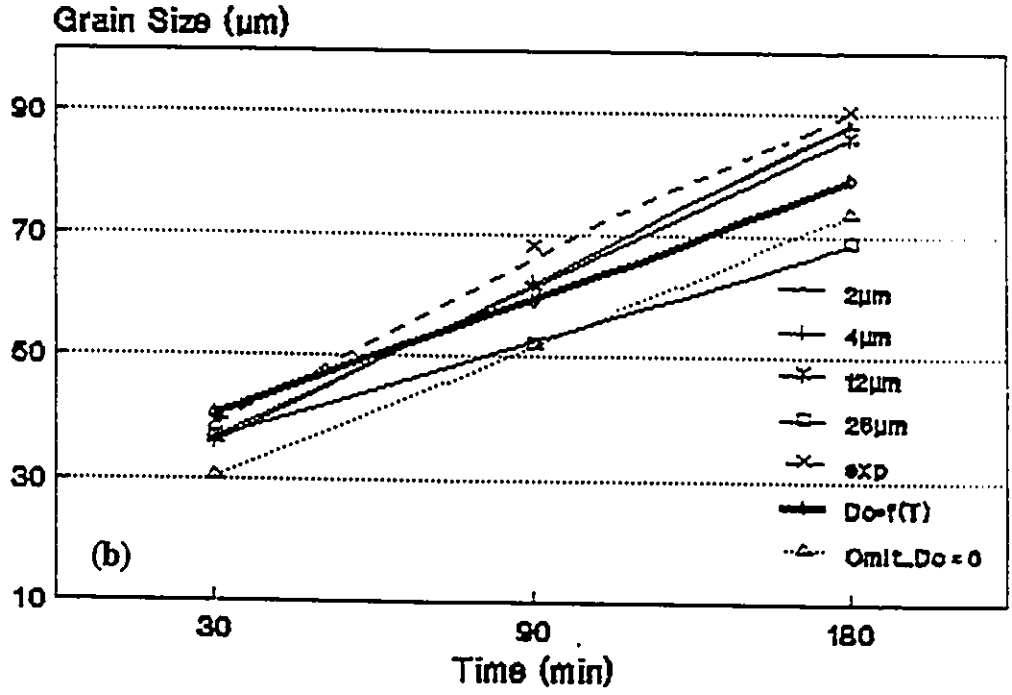

Fig. 4-5 Calculated grain sizes for Jominy test data using parabolic grain growth equation with different assumed D_o at different temperatures. (a) 1144 K; (b) 1120 K; (c) 1256 K; (d) 1311 K.

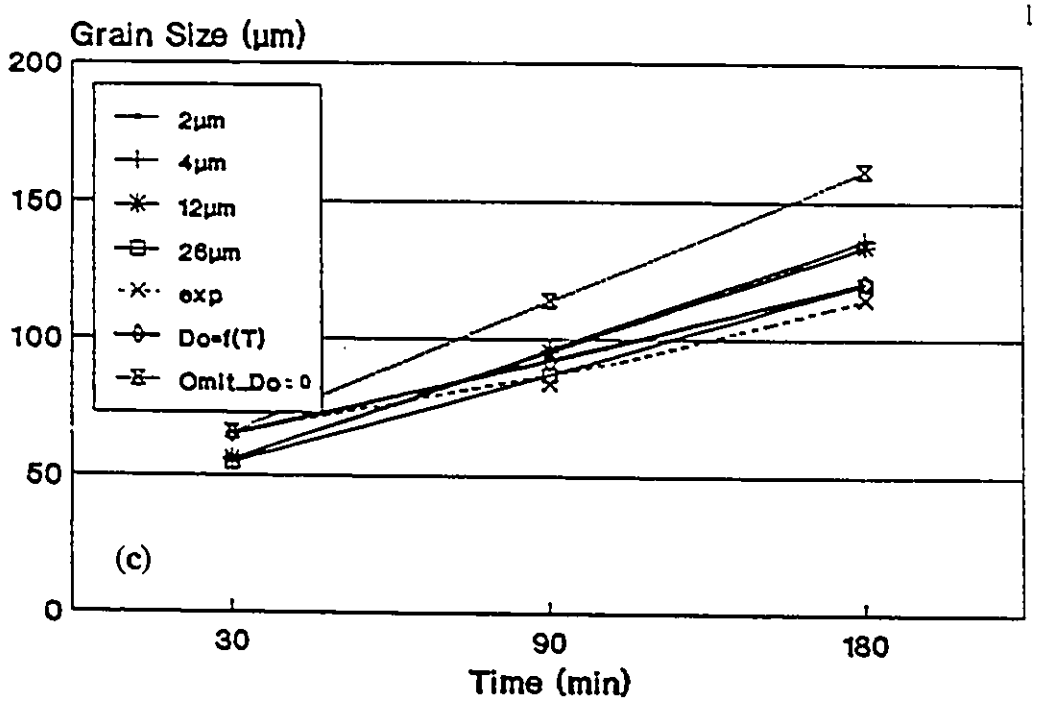

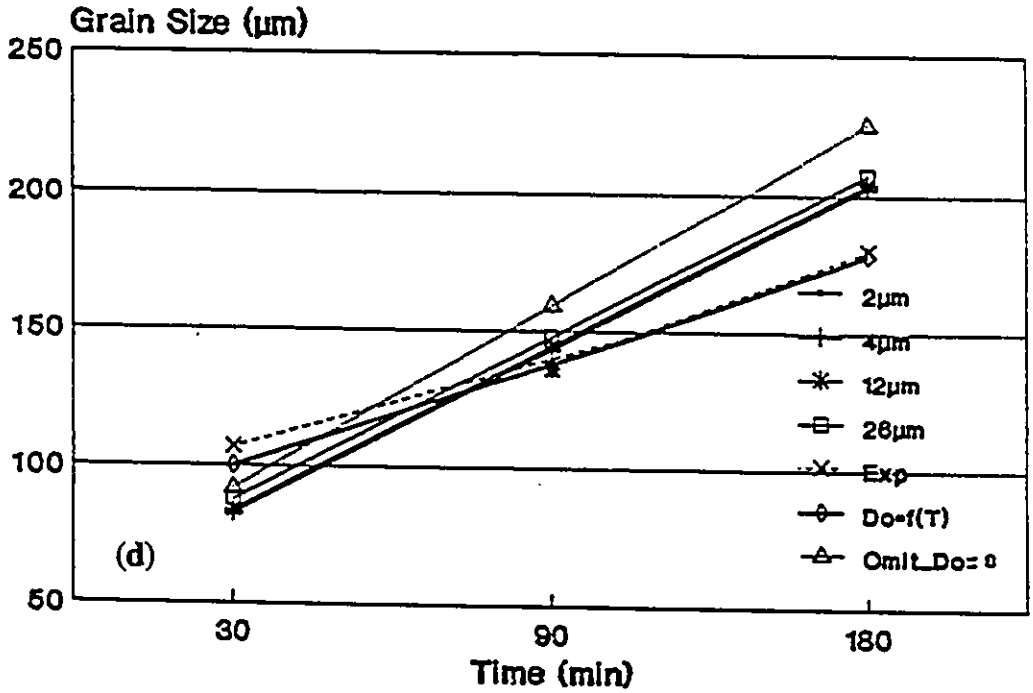

Fig. 4-5 (continue) Calculated grain sizes for Jominy test data using parabolic grain growth equation with different assumed D_o at different temperatures. (a) 1144 K; (b) 1120 K; (c) 1256 K; (d) 1311 K.

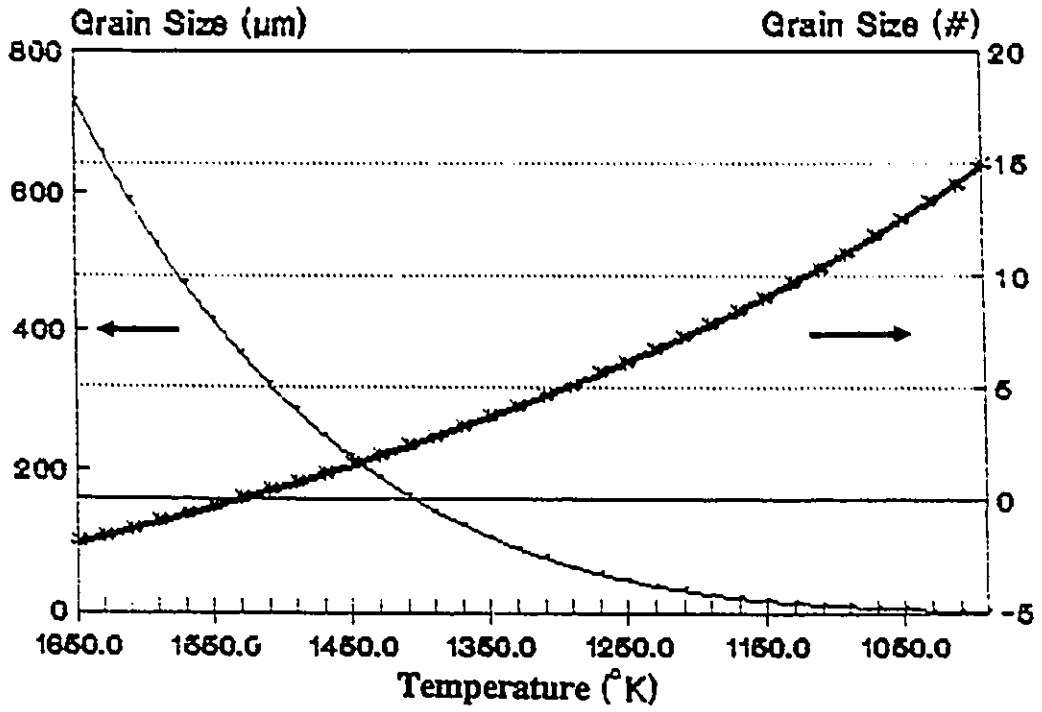

Fig. 4-6 Grain Diameter and grain size number vs temperature calculated by the derived empirical equation at one second.

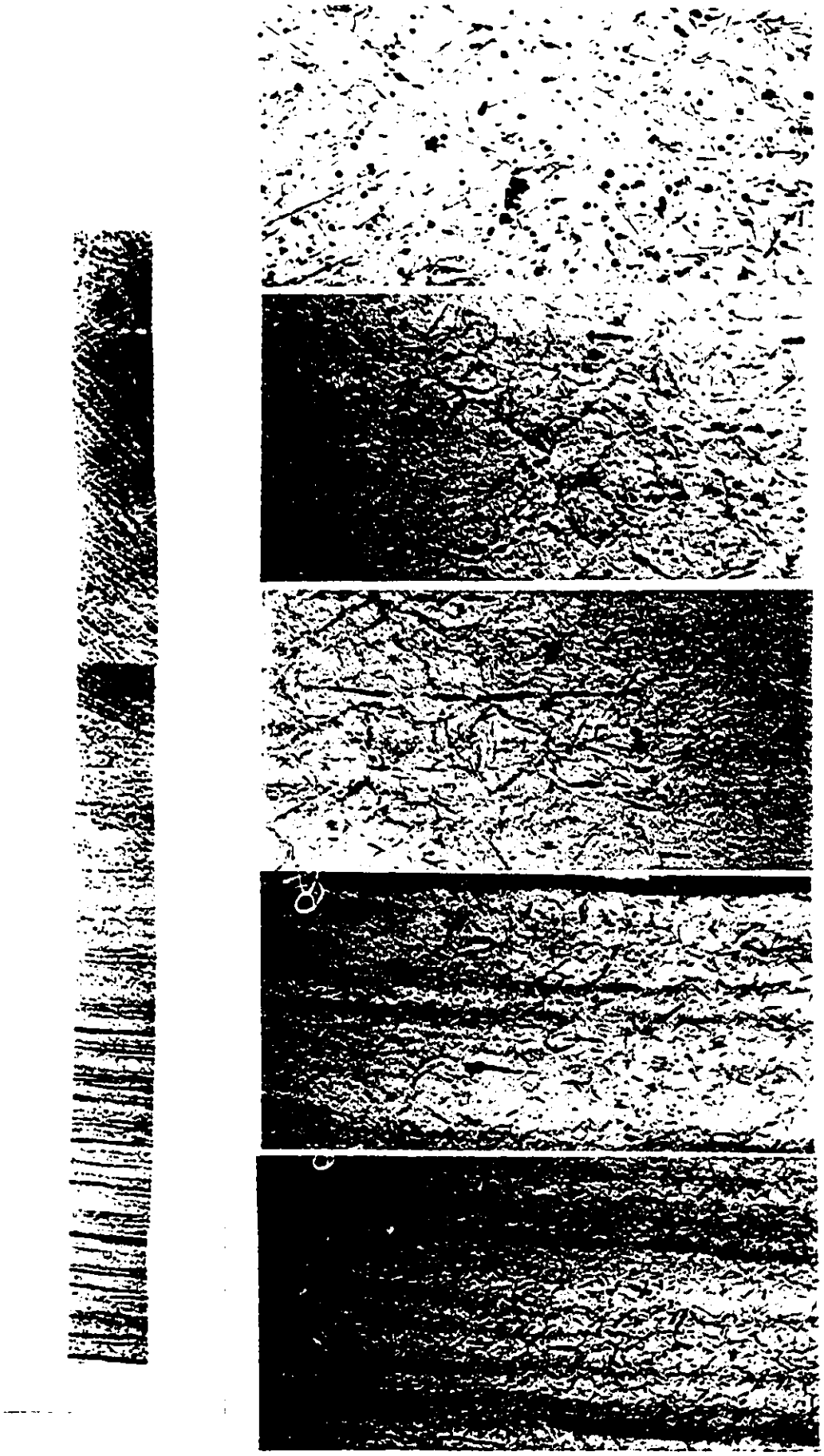

Fig. 4-7 Photographs of austenite grain size in the heat-affected zone along the centreline from real resistance welded bars as shown in left strip; right: corresponding pictures as indicated in left strip at magnification 200X.

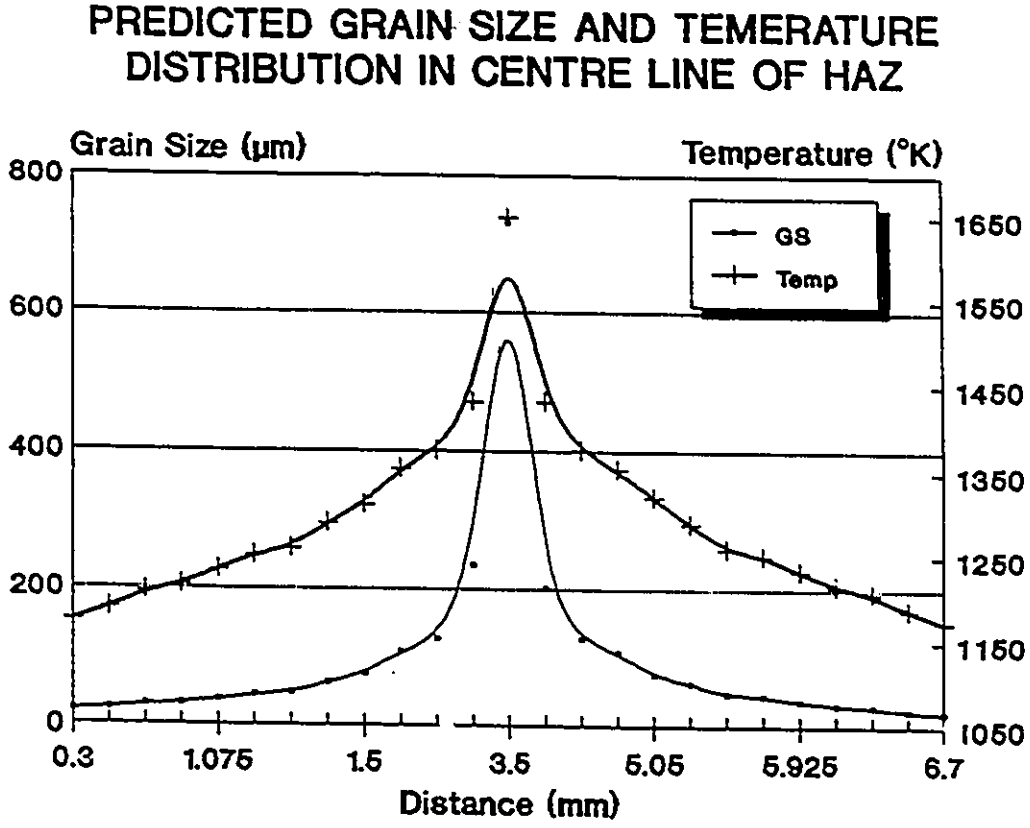

Fig. 4-8 Predicted temperature and grain size distribution along the vertical centre line of the heat-affected zone. The weld line is at 3.5 mm.

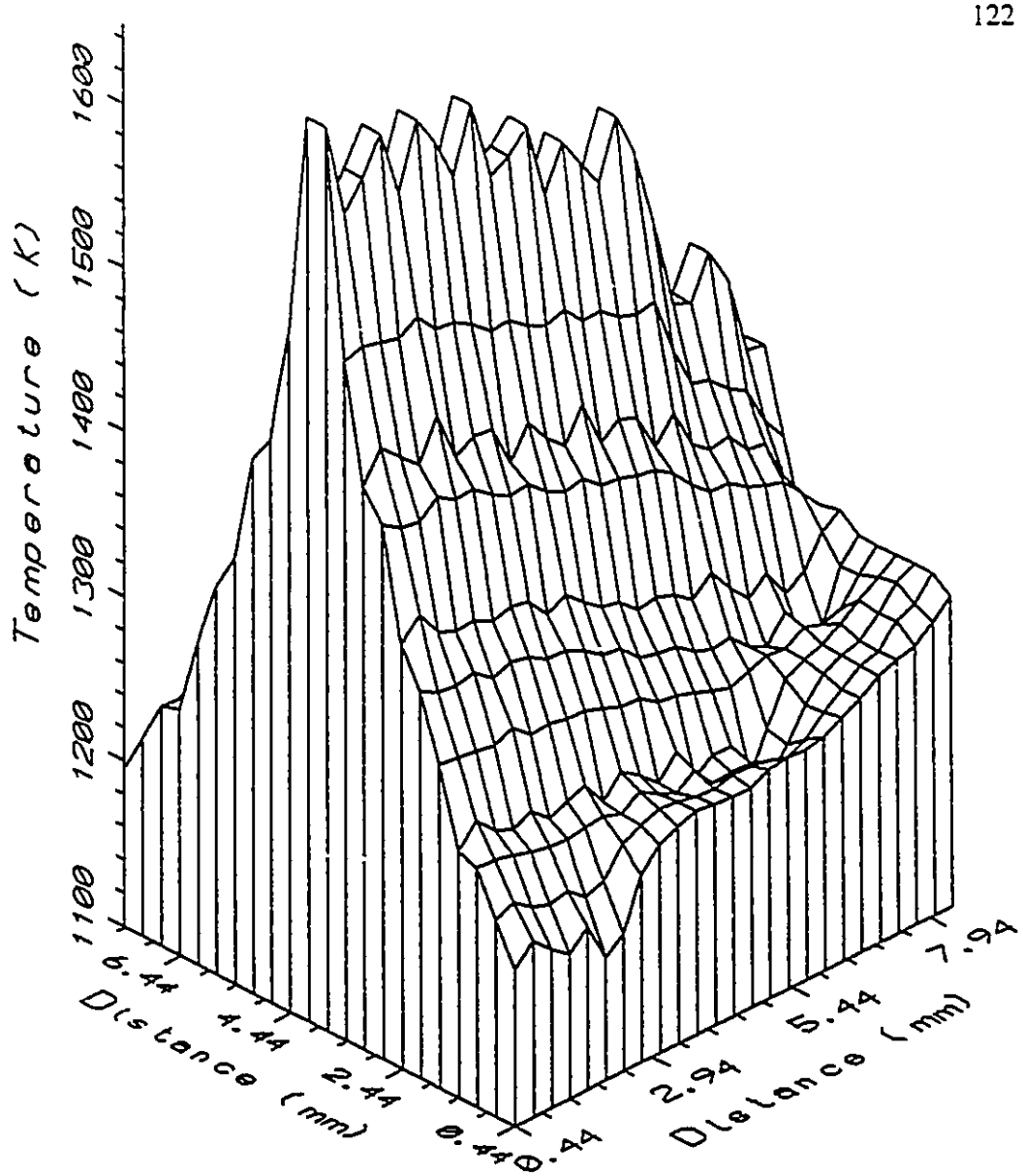

Fig. 4-9 Predicted initial temperature profile in the heat-affected zone at the end of the welding current stage.

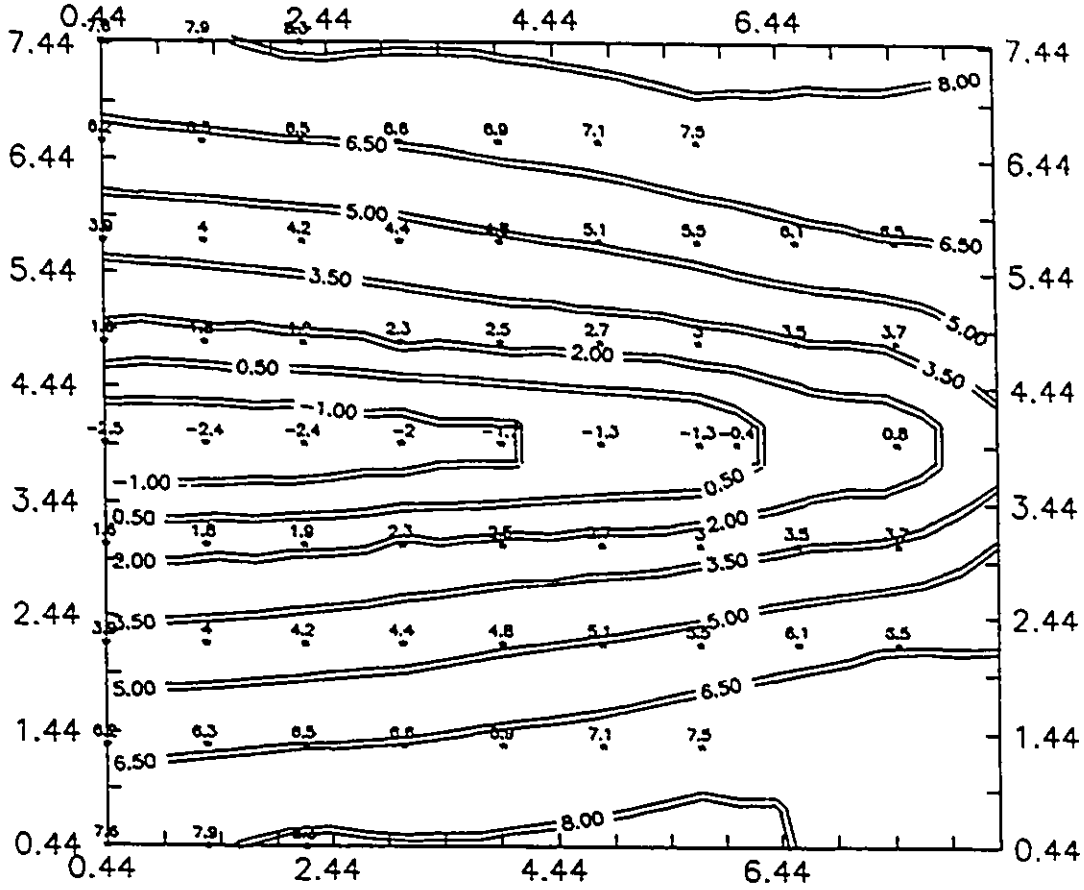

Fig.4-10 A map of the predicted austenite grain size numbers in the heat-affected zone in the geometrical model of resistance welded bars.

Fig.4-11 Photograph of crack initiated at the edge of the heat-affected zone typical of the resistance welded bars.

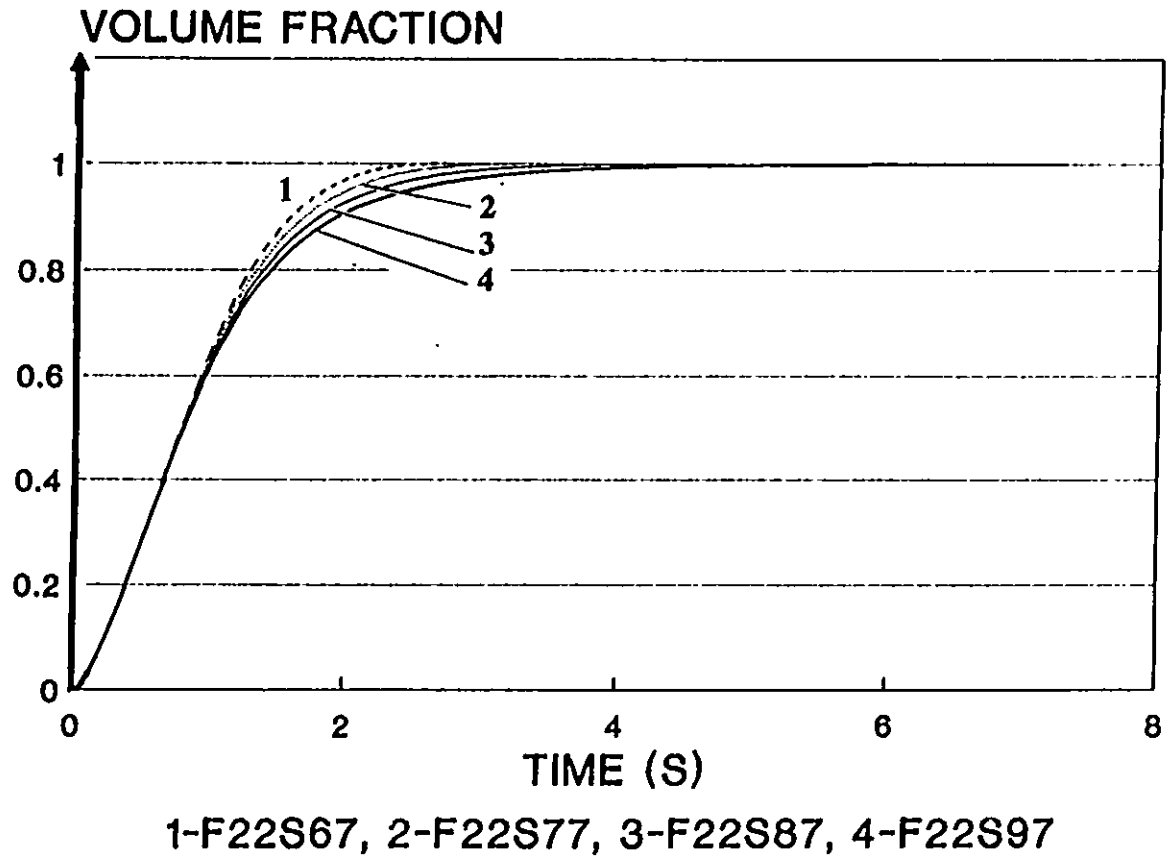

Fig. 6-1 Influence of the exponents F and S on transformation reaction rate; transformed volume fraction vs time. First exponent F was fixed at 0.22, and second exponents S is changed to 0.67, 0.77, 0.87, and 0.97.

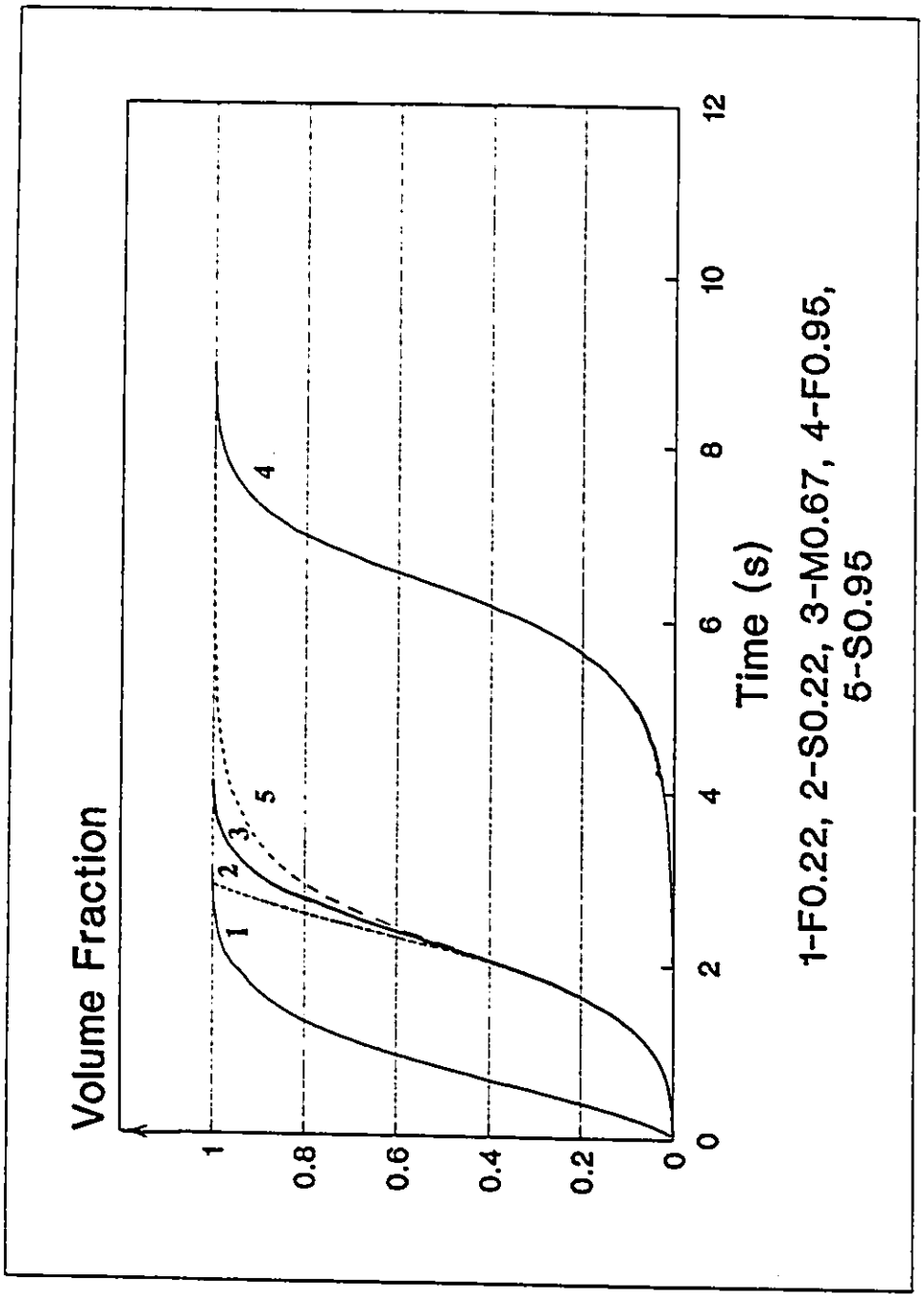

Fig. 6-2 Influence of the exponents F and S on transformation reaction rate; transformed volume fraction vs time. One of the exponents is fixed at 0.67, another is changed as indicated in Figure.

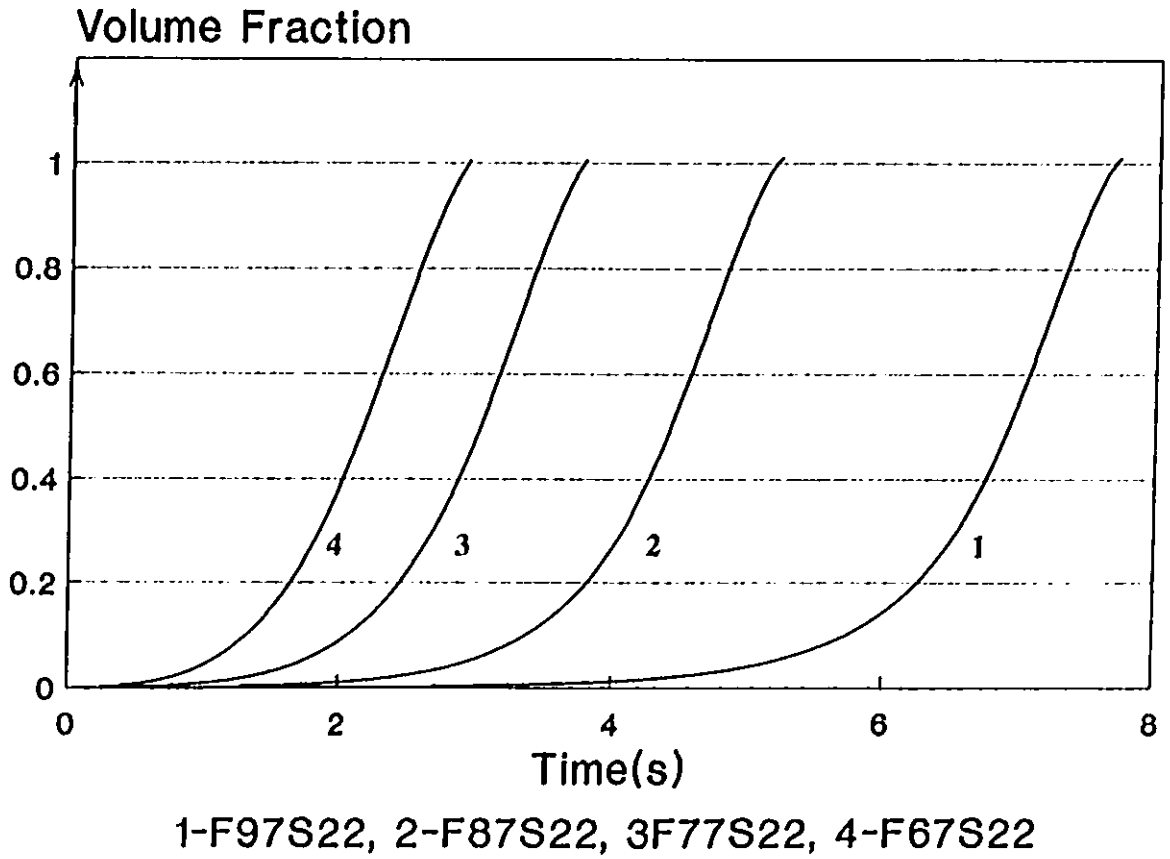

Fig. 6-3 Influence of the exponents F and S on transformation reaction rate; transformed volume fraction vs time. The first exponent F is changed to 0.67, 0.77, 0.87 and 0.97; the second exponent S is fixed at 0.22.

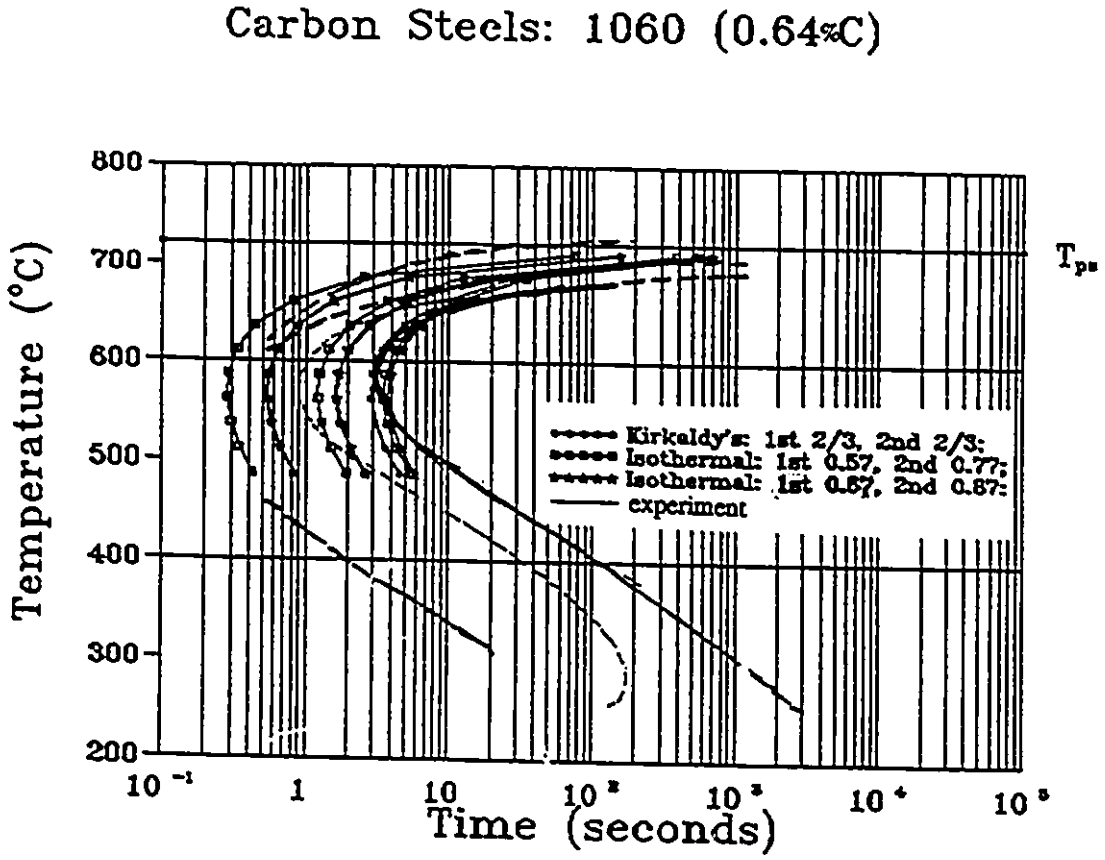

Fig. 6-4 IT diagram calculated using modified and unmodified Kirkaldy equations compared with the experimental IT diagrams for a 1060 steel. C 0.64; Mn 0.68; Si 0.22; G.S. 7.5.

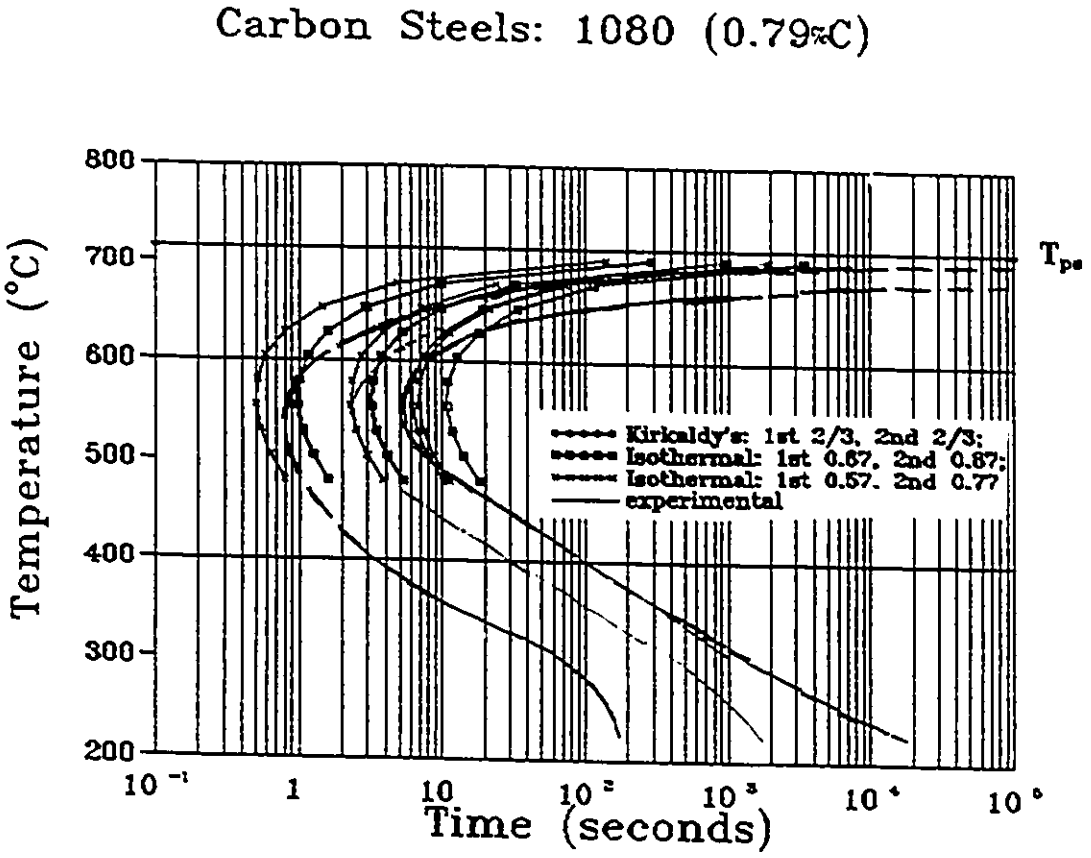

Fig. 6-5 IT diagram calculated using modified and unmodified Kirkaldy equations compared with the experimental IT diagrams for a 1080 steel. C 0.79; Mn 0.76; Grain Size 6.

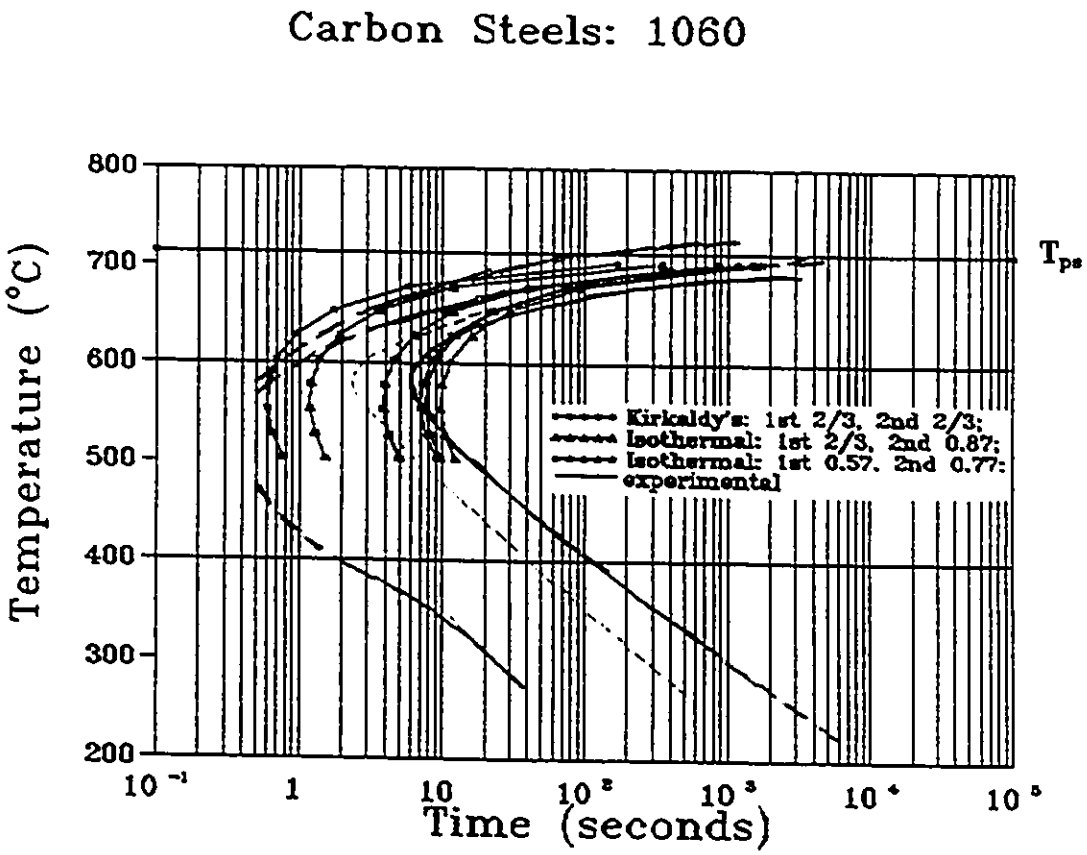

Fig. 6-6 IT diagram calculated using modified and unmodified Kirkaldy equations compared with the experimental IT diagrams for a 1060 steel. C 0.63; Mn 0.87; Grain Size 5-6.

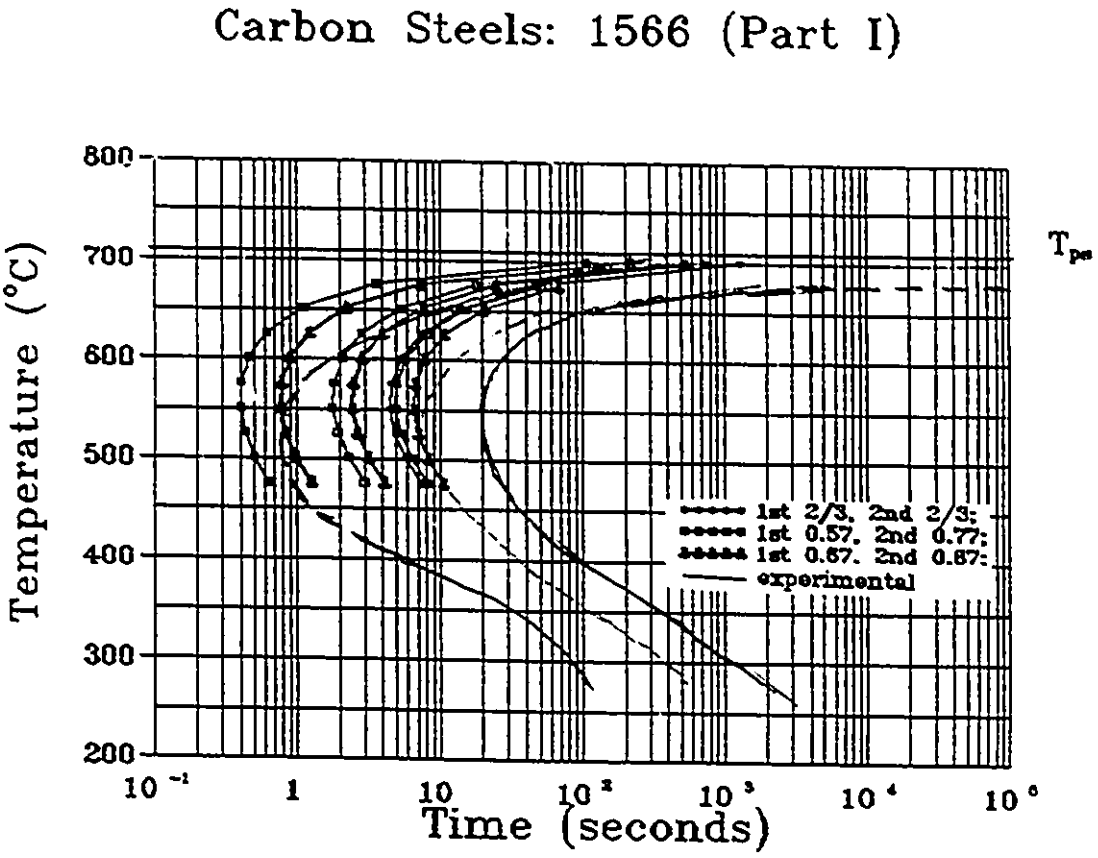

Fig. 6-7 IT diagram calculated using modified and unmodified Kirkaldy equations compared with the experimental IT diagrams for a 1566 steel. C 0.64; Mn 1.13; Grain Size 7.

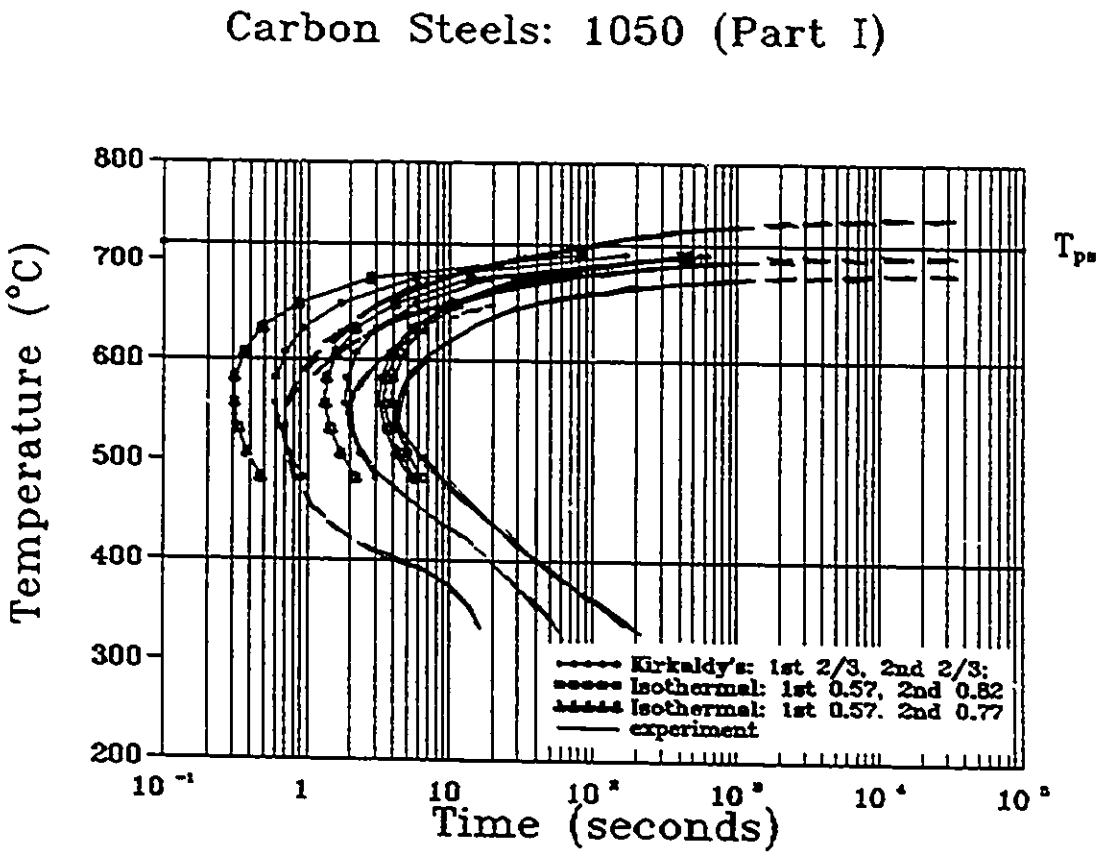

Fig. 6-8 IT diagram calculated using modified and unmodified Kirkaldy equations compared with the experimental IT diagrams for a 1050 steel. C 0.50; Mn 0.91; Si 0.13; Grain Size 7-8.

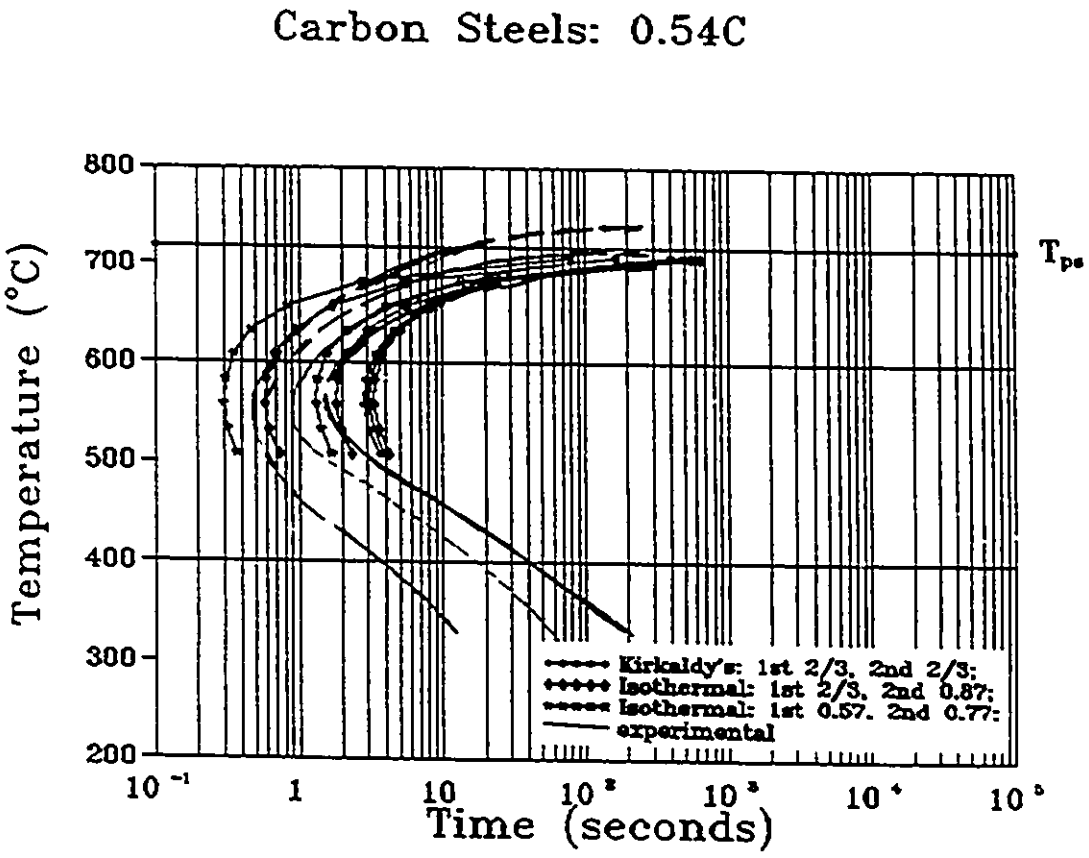

Fig. 6-9 IT diagram calculated using modified and unmodified Kirkaldy equations compared with the experimental IT diagrams for a 1055 modified Mn steel. C 0.54; Mn 0.46; Grain Size 7-8.

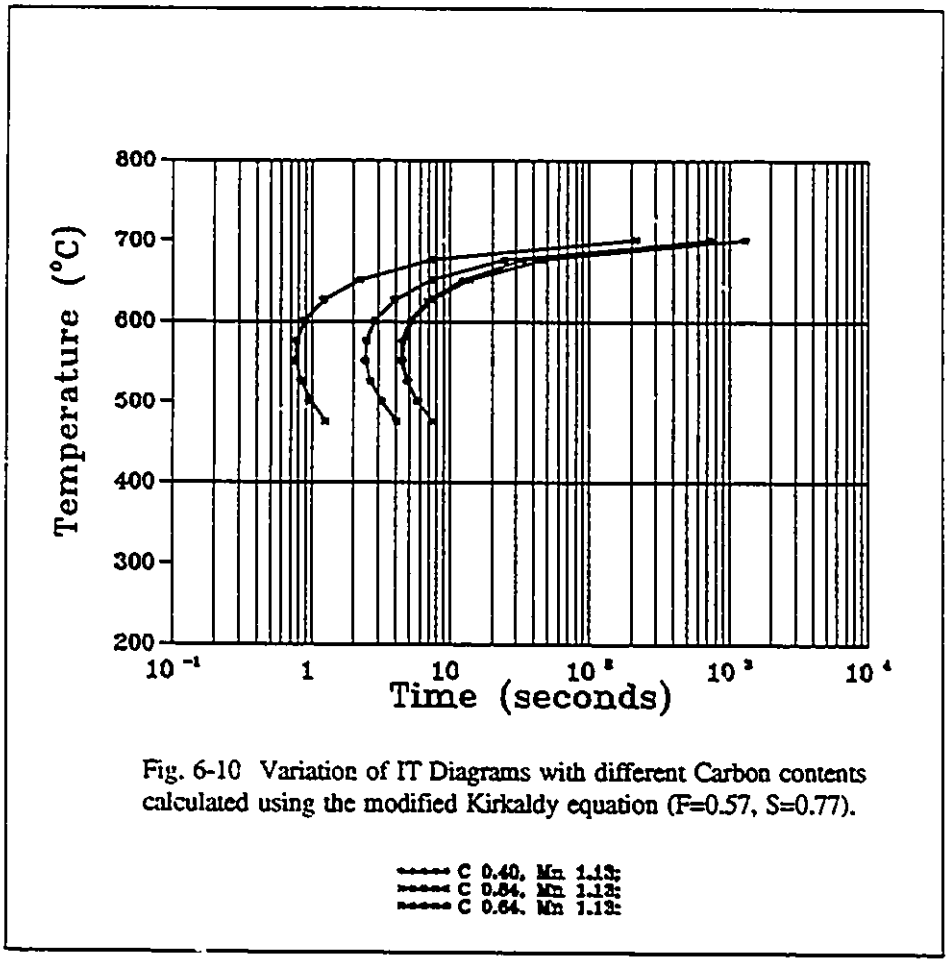

Fig. 6-10 Variation of IT Diagrams with different Carbon contents calculated using the modified Kirkaldy equation (F=0.57, S=0.77).

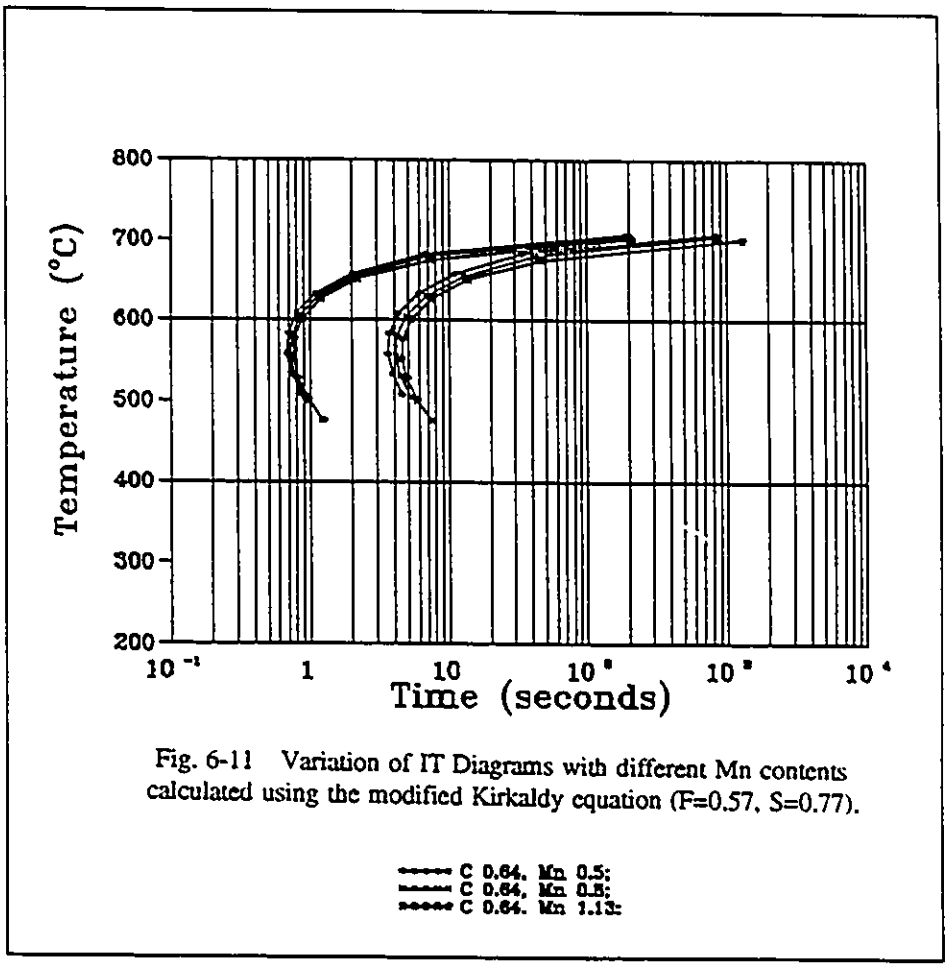

Fig. 6-11 Variation of IT Diagrams with different Mn contents calculated using the modified Kirkaldy equation (F=0.57, S=0.77).

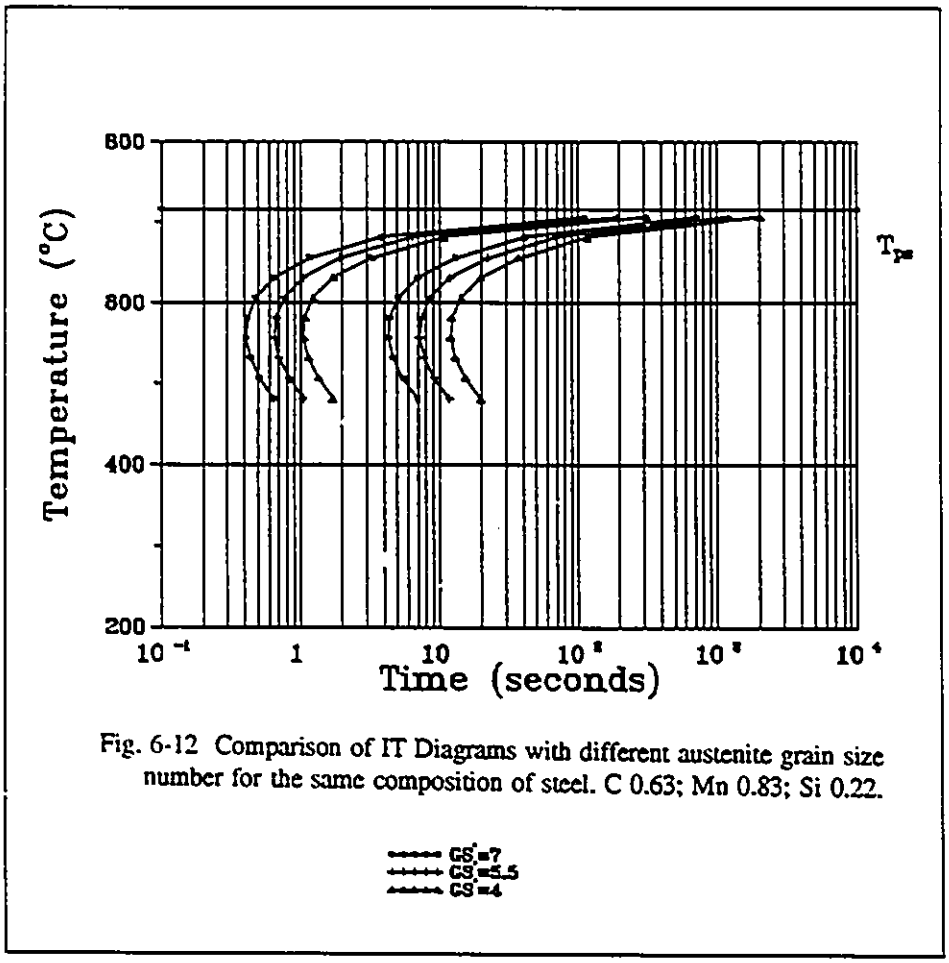

Fig. 6-12 Comparison of IT Diagrams with different austenite grain size number for the same composition of steel. C 0.63; Mn 0.83; Si 0.22.

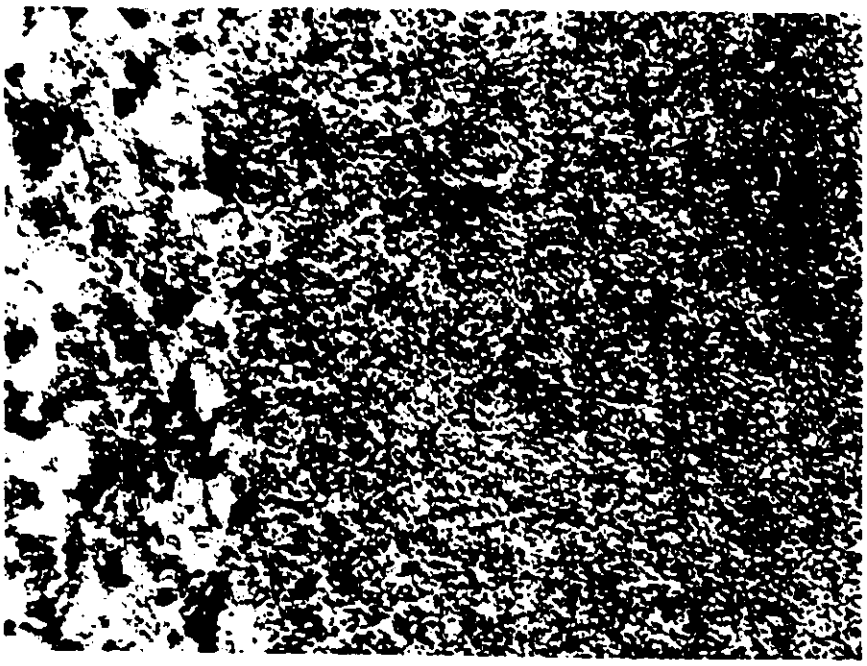

(a)

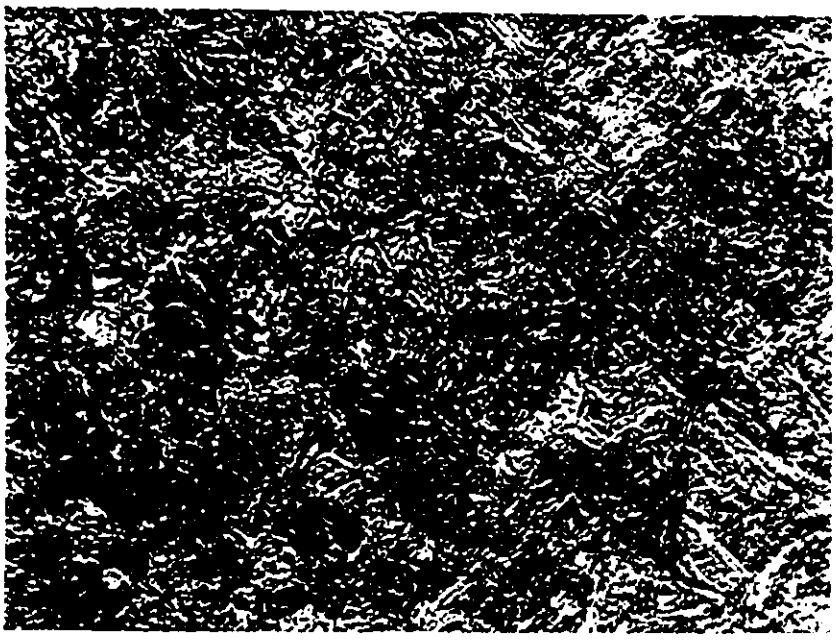

(b)

Fig. 7-1 Microstructures in the HAZ for a no post-weld heat. (a) at intercritical grained zone of the HAZ. The microstructure is a pearlite, bainite and martensite mixture; (b) at the centre of the HAZ near the fusion line, the microstructure is martensite. Light micrograph. Vilella'reagent. Magnification 200X.

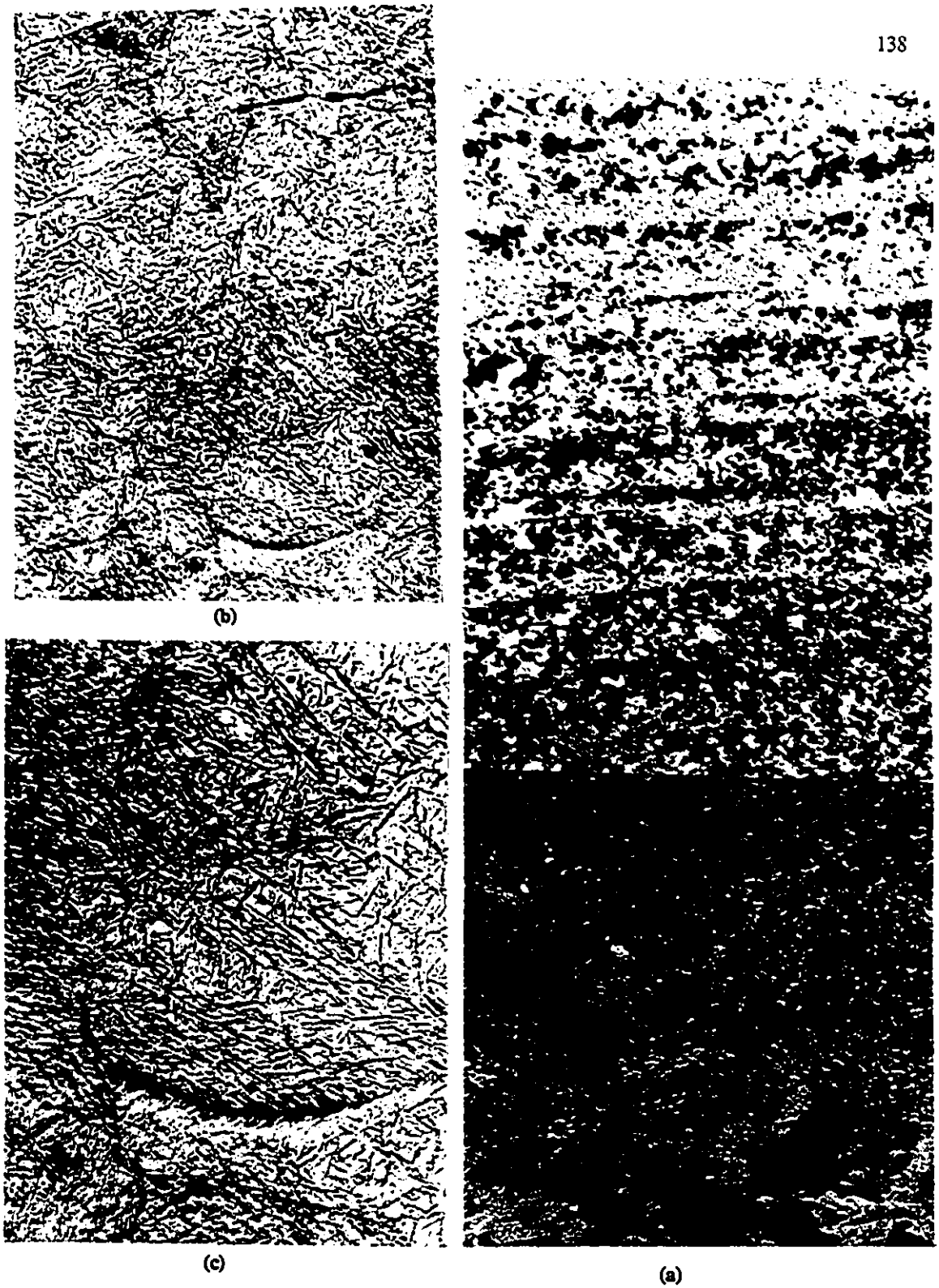

Fig.7-2 Microstructures in the HAZ at a post-weld heat of 5% of welding current, and 180 cycles. (a) at intercritical grained zone of the HAZ, microstructure is a pearlite, bainite and martensite mixture; 200X; (b) at the centre of the HAZ near the fusion line, the microstructure is martensite. Some feather like bainite occur(200X). (c) same as (b) but 500X. Light micrograph. Vilella'reagent.

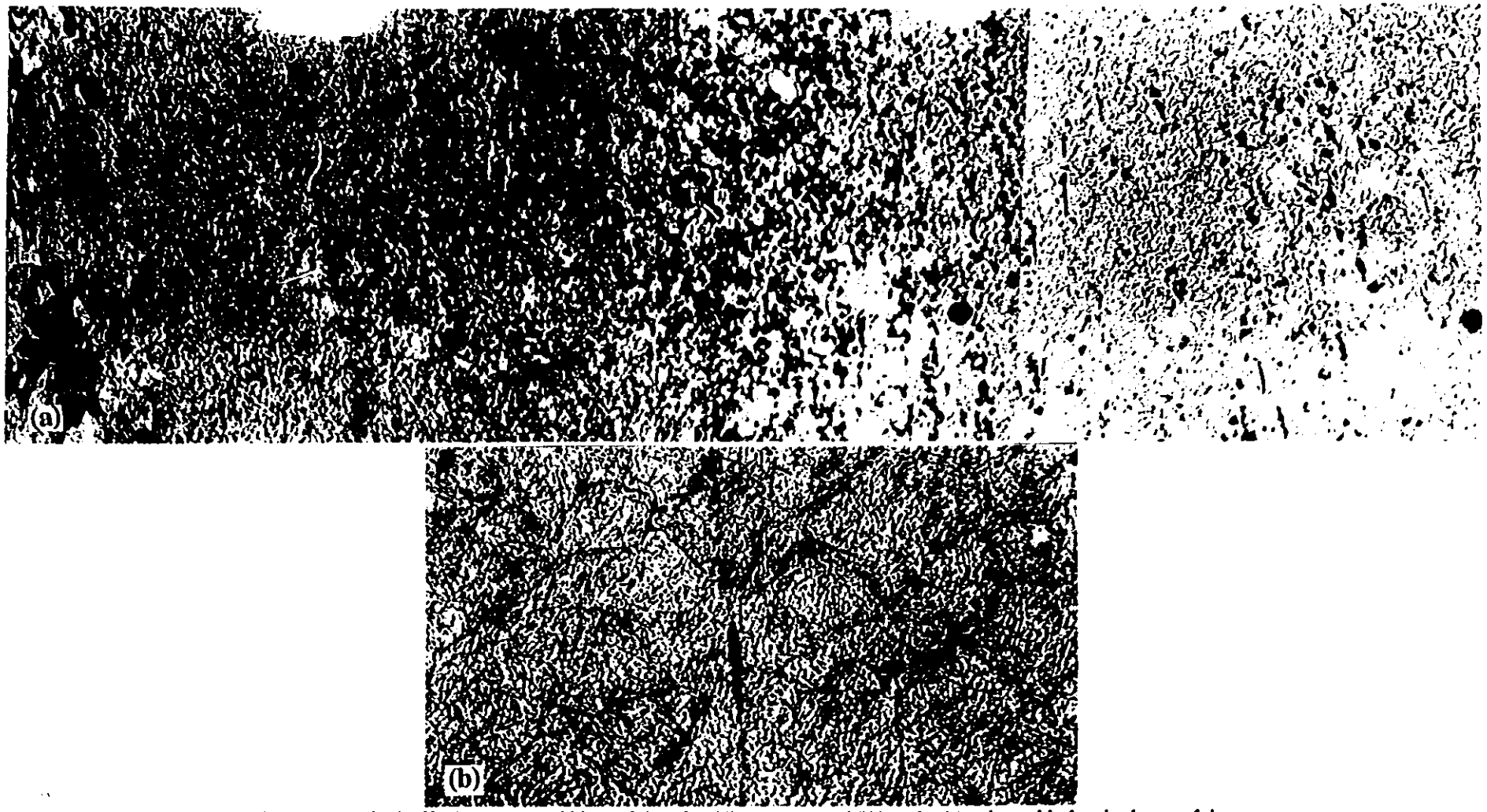

Fig. 7-3 Microstructures in the HAZ at a post-weld heat of 5% of welding current, and 720 cycles.(a) at intercritical grained zone of the HAZ, the microstructure is a pearlite, bainite and martensite mixture; (b) at the centre of the HAZ near the fusion line, microstructure is martensite. Light micrograph. Vilella'reagent. Magnification 200X.

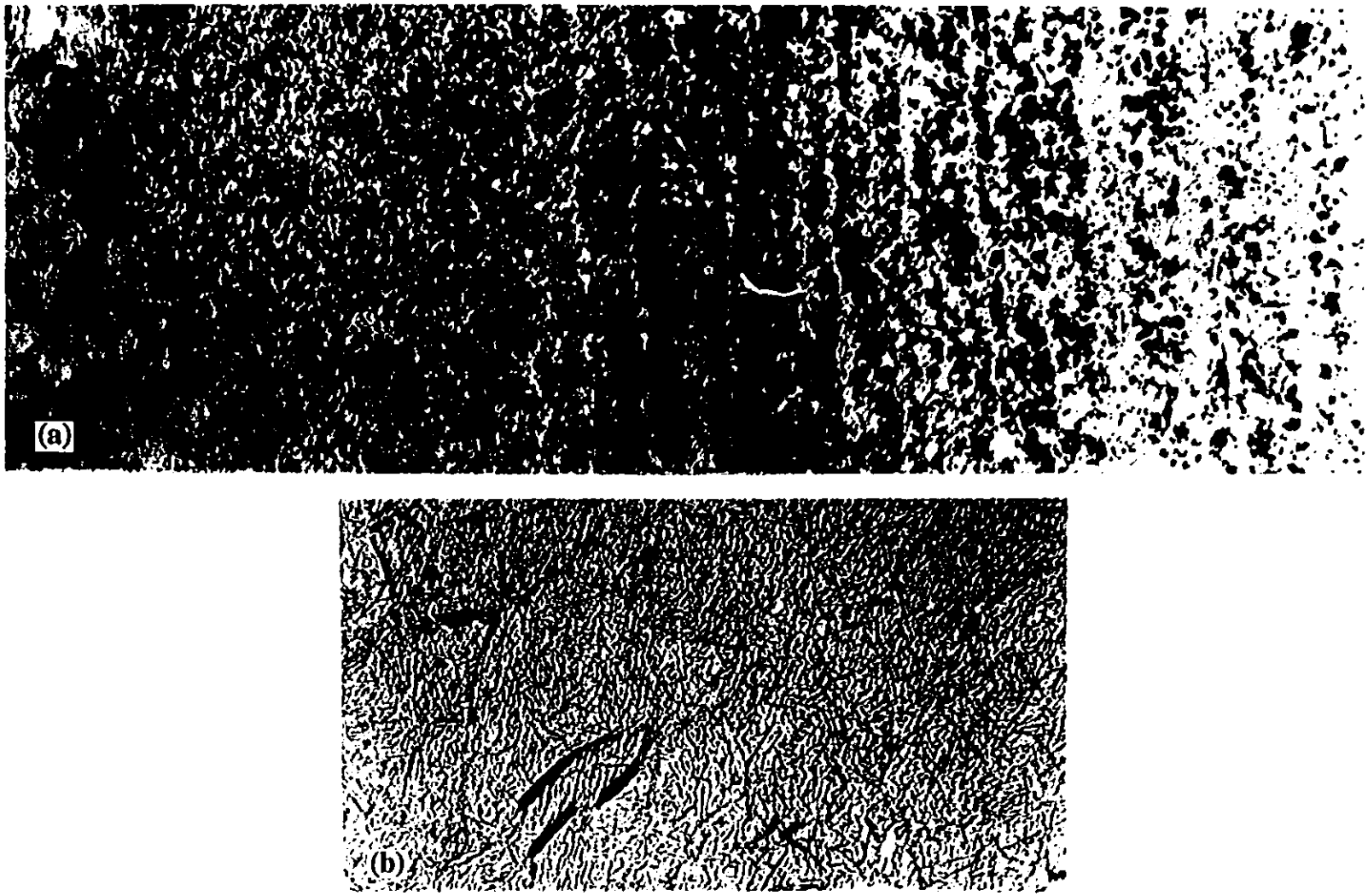

Fig. 7-4 Microstructures in the HAZ at a post-weld heat of 10% of welding current, and 720 cycles. (a) at intercritical grained zone of the HAZ, the microstructure is pearlite, bainite and martensite mixture; (b) at the centre of the HAZ near the fusion line, microstructure is martensite. Light micrograph. Vilella'reagent etched. Magnification 200X.

Fig. 7-5 Microstructures in the HAZ at a post-weld heat of 15% of welding current, and 720 cycles.
(a) a strip along the centre part of the HAZ.

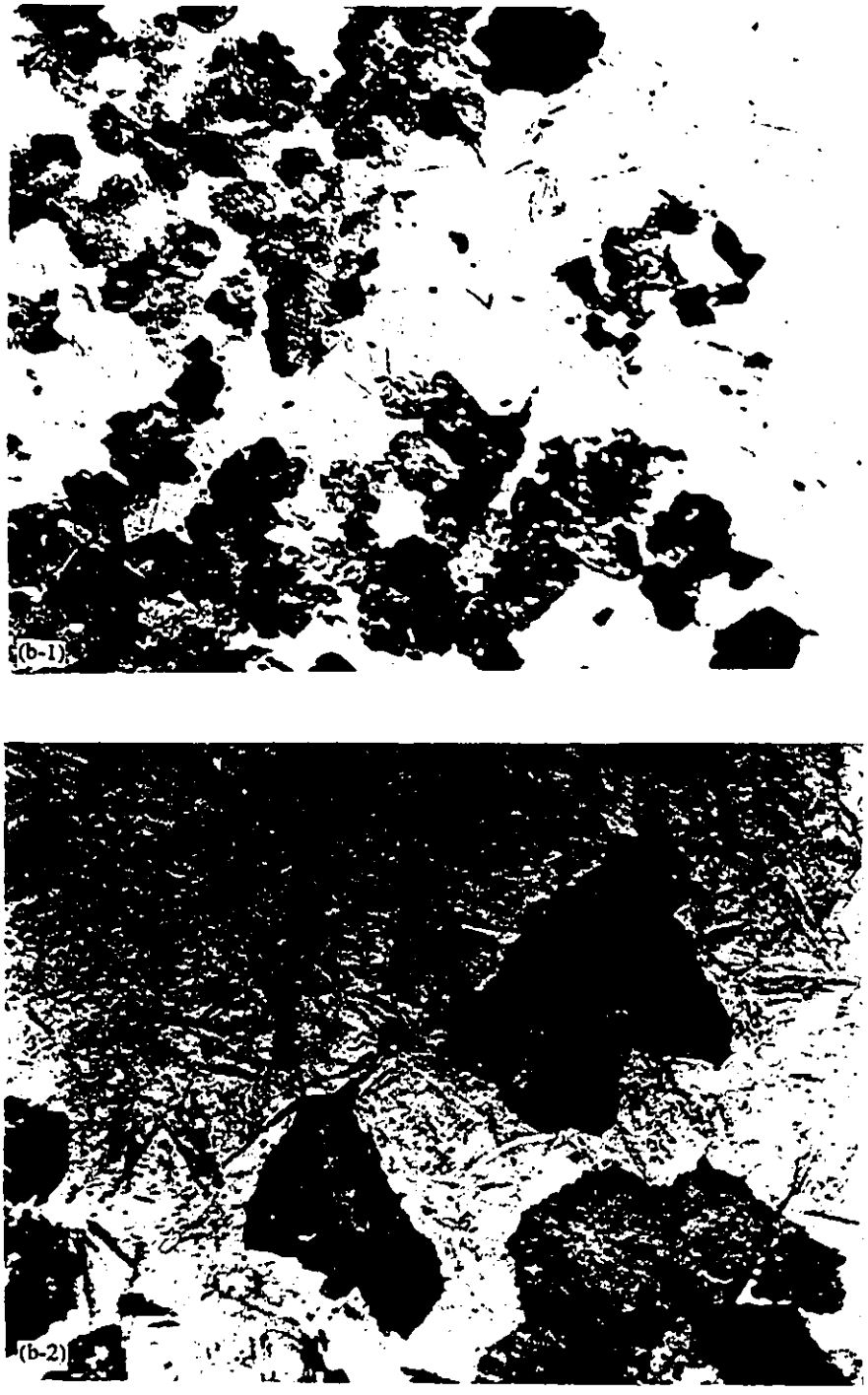

Fig. 7-5 [continue]: (b-1) related to point A in the (a), pearlite develops at the austenite grain boundaries 200X; (b-2) same as (b-1) but magnification of (b) 1000X;

(c)

(d)

Fig.7-5 [continue] (c) related to point B in the (a), feather like bainite occurs near the fusion line of the HAZ, together with Martensite 500X; (d) related to point C in the (a), feather like bainite occurs together with martensite 500X. Light micro graph. Vilella'reagent.

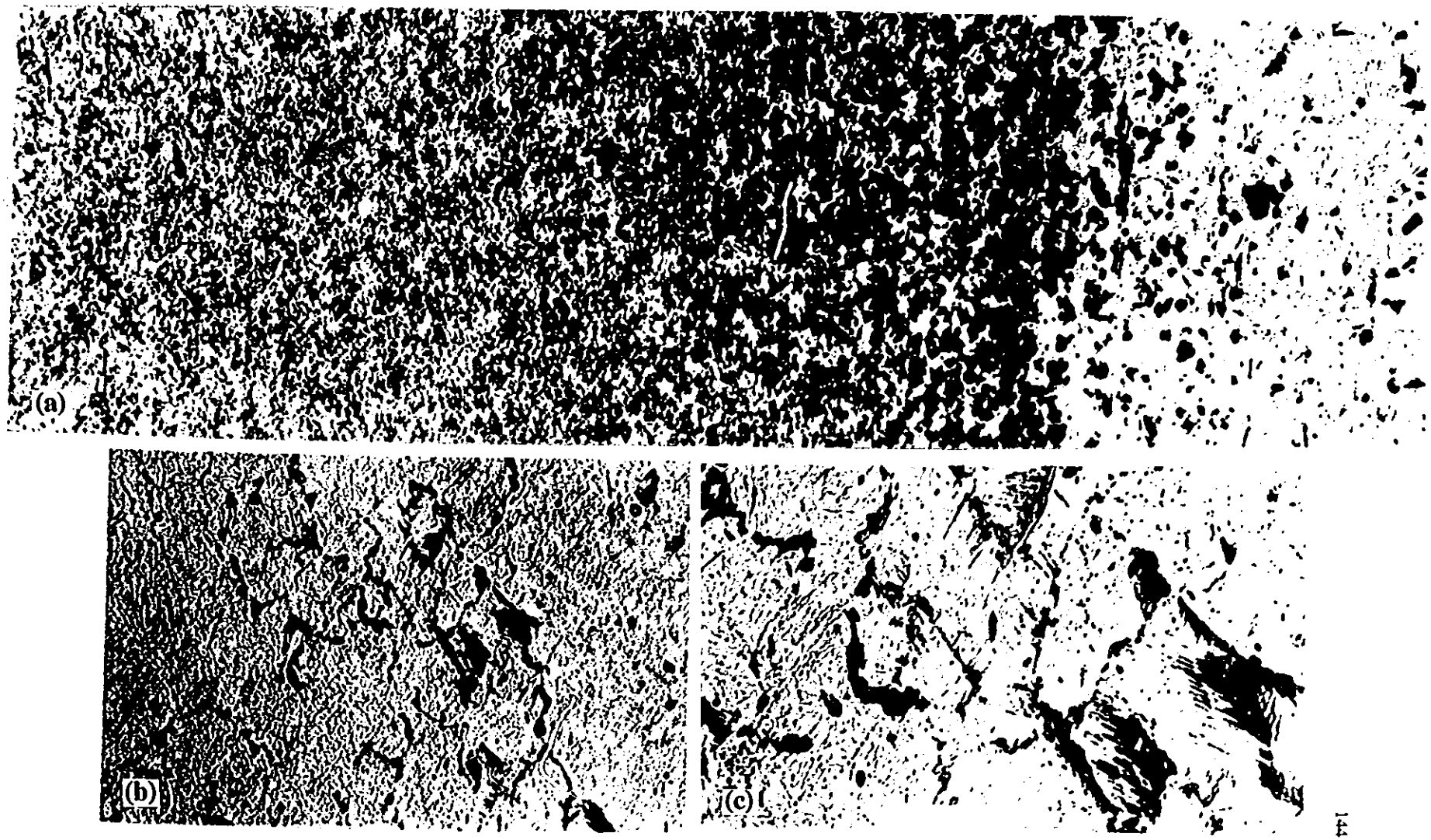

Fig.7-6 Microstructures in the HAZ at a post weld heat of 15% of welding current, and 416 cycles. Magnification 200X. (a) at intercritical grained zone of the HAZ. The microstructure is a pearlite, bainite and martensite mixture; (b) at the centre of the HAZ near the fusion line, microstructure is martensite. A few feather like bainite occur. (c) magnification of (b) at 500X. Light micrograph.

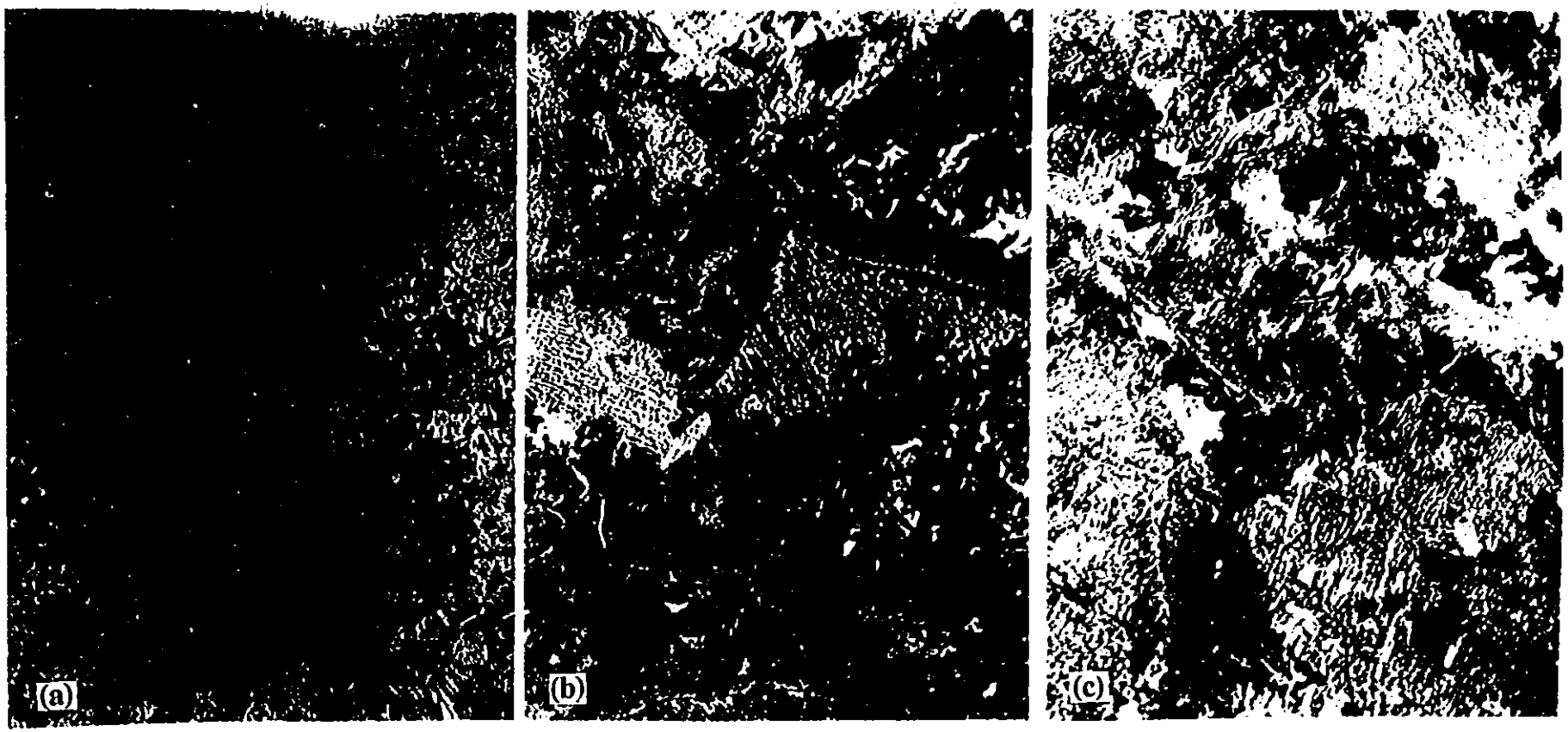

Fig.7-7 Microstructures in the HAZ for at the standard welding cycle used by Coschell. (a) at the intercritical grained zone of the HAZ, a pearlite, bainite and martensite mixture; (b) and (c) at the centre of the HAZ near the fusion line, feather like bainite well developed, magnification 500X. Light micrograph. Vilella'reagent .

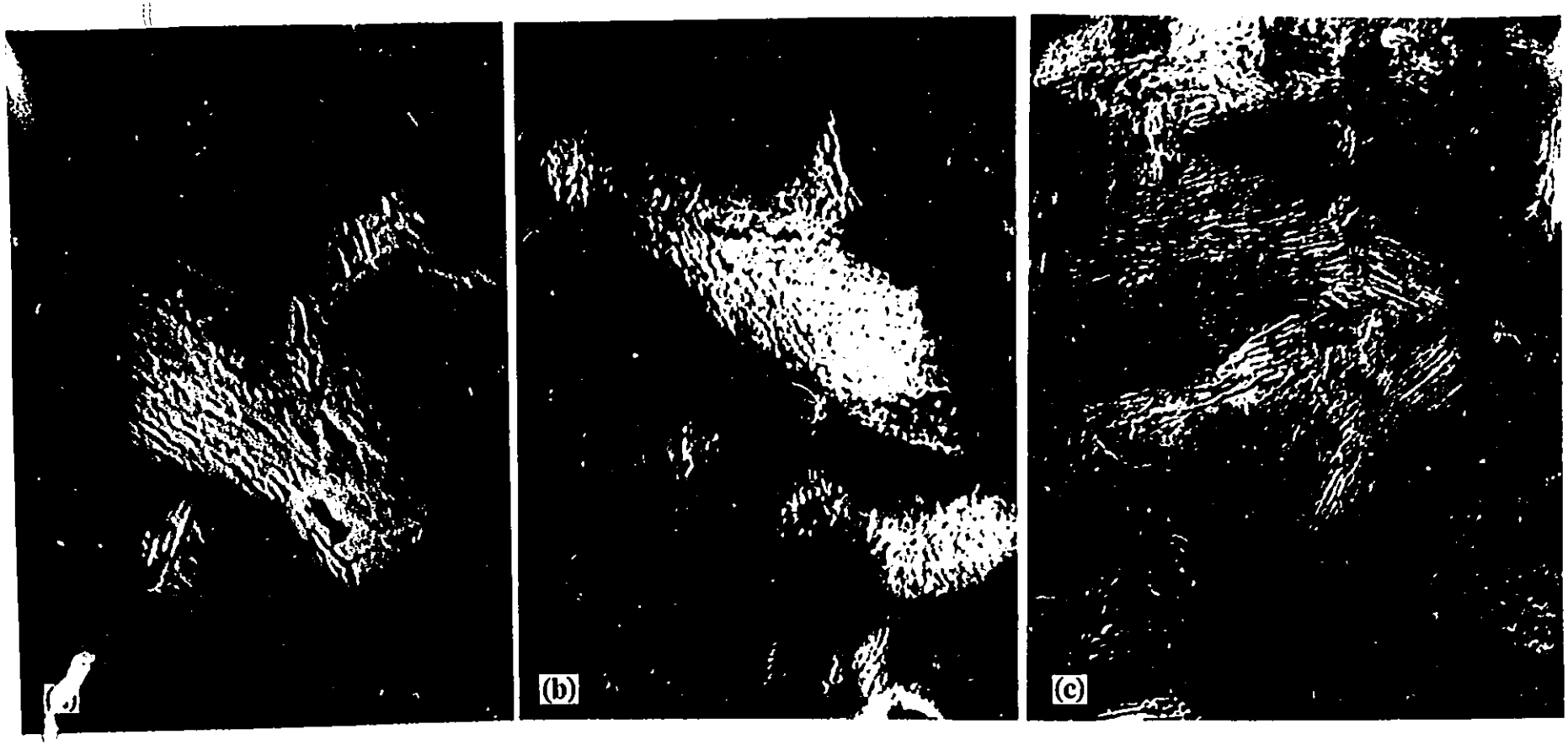

Fig.7-8 Pearlite nodulus from intercritical grained region of the HAZ taken by SEM. post-weld heat: (a) 10% of welding current, 720 cycles, 5000X; (b) 15% of welding current, 416 cycles, 5000X; (c) 15% of welding current, 720 cycles, 3000X;

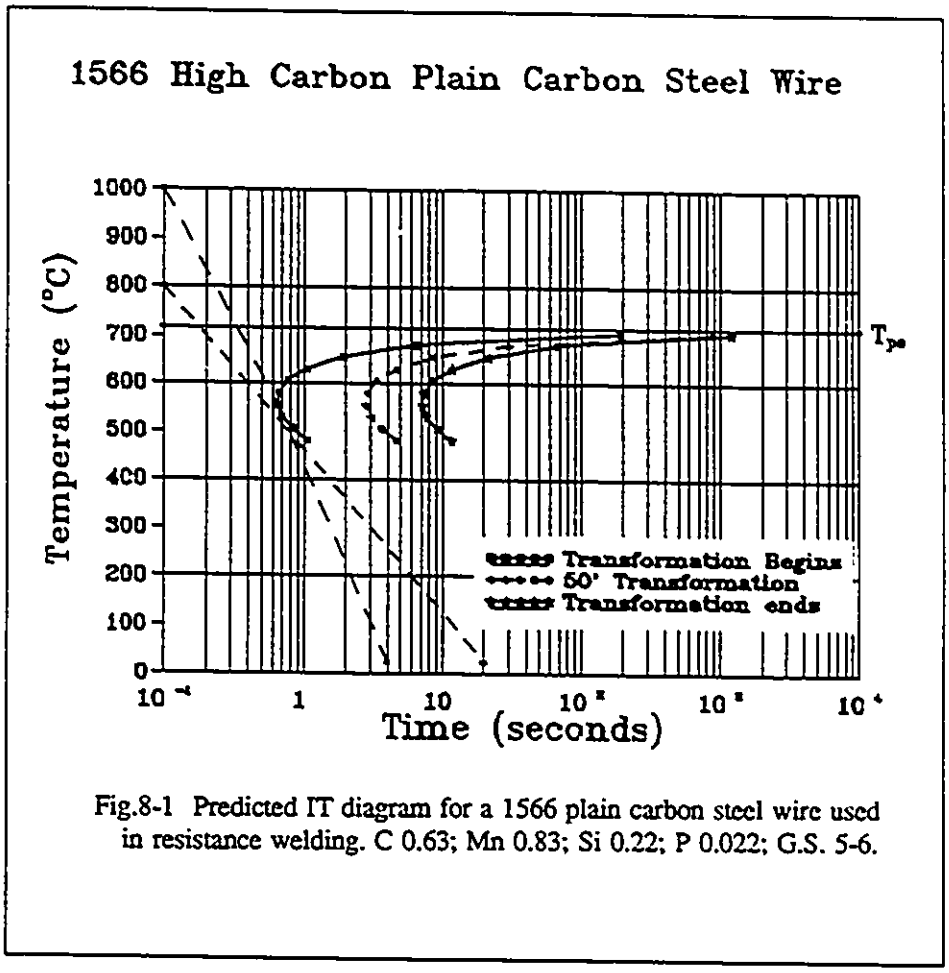

Fig.8-1 Predicted IT diagram for a 1566 plain carbon steel wire used in resistance welding. C 0.63; Mn 0.83; Si 0.22; P 0.022; G.S. 5-6.

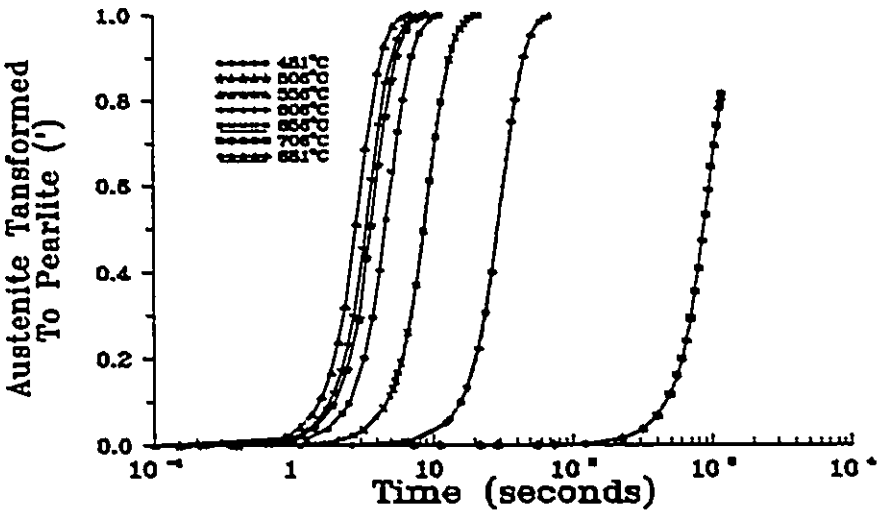

Fig.8-2 Relationship of 1566 steel wire isothermal reaction curves for pearlite transformation at different temperatures.

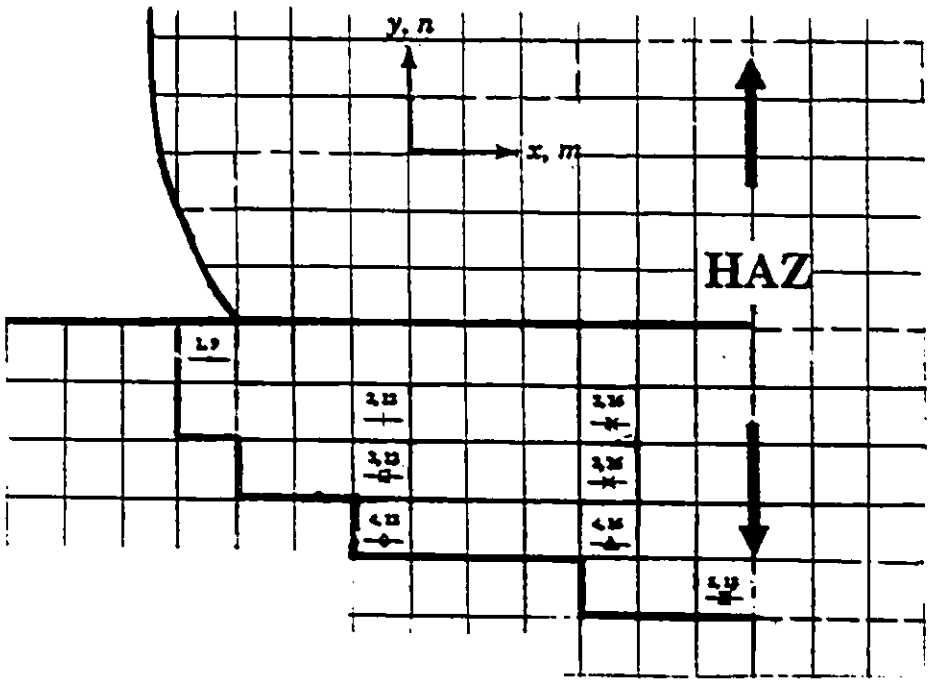

Fig. 8-3 Selected node positions and symbols in the HAZ.

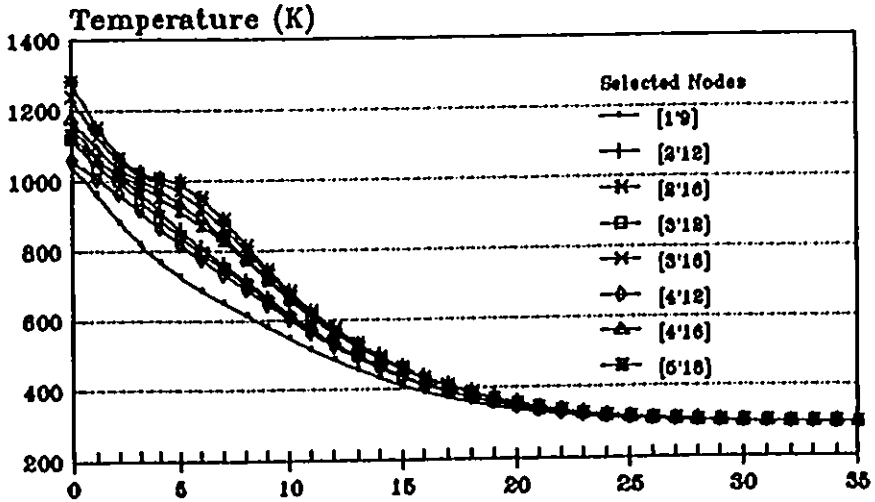

Cooling curves for selected nodes
(No post-heating)

(a)

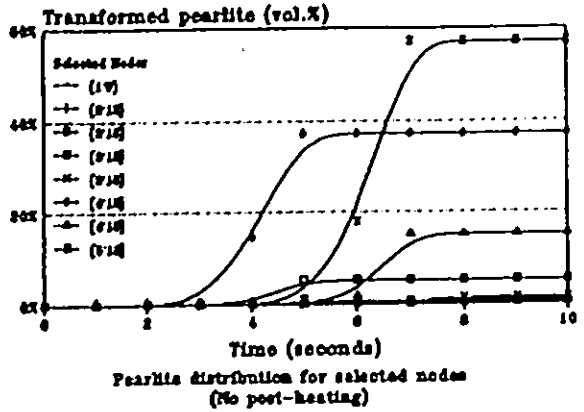

Pearlite distribution for selected nodes
(No post-heating)

(b)

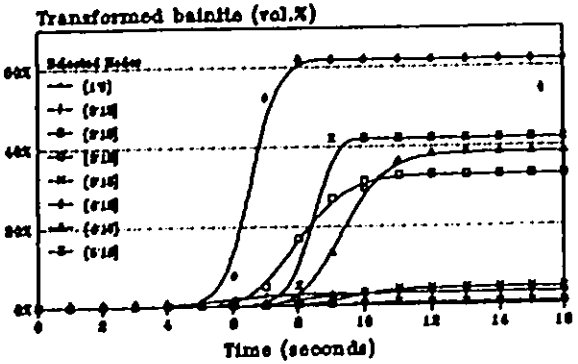

Bainite distribution for selected nodes
(No post-heating)

(c)

Fig.8-4 Diagrams for temperature distribution and microstructure development for selected nodes on cooling at no post-weld heat. (a) temperature vs time. (b) Transformed pearlite (vol.%) vs time. (c) Transformed bainite (vol.%) vs time.

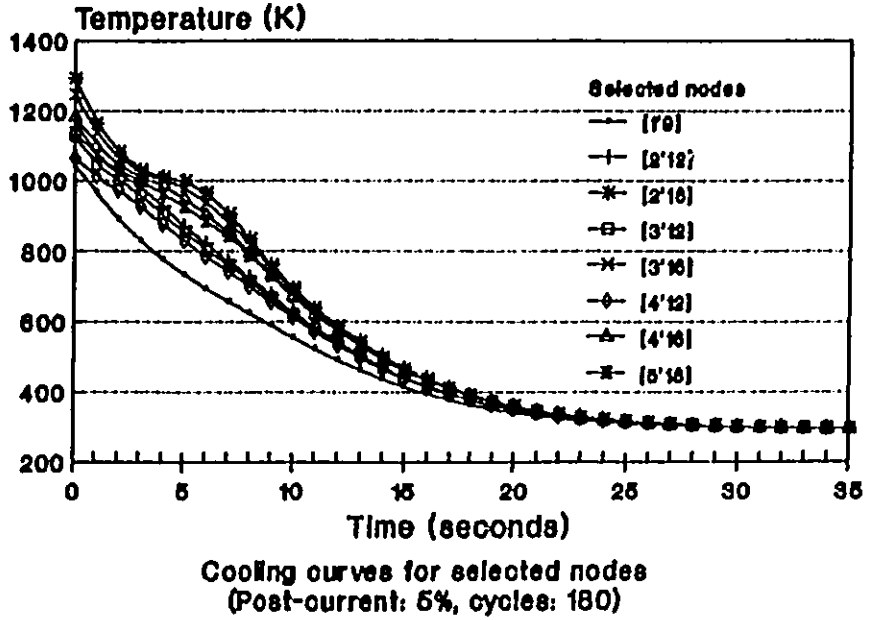

(a)

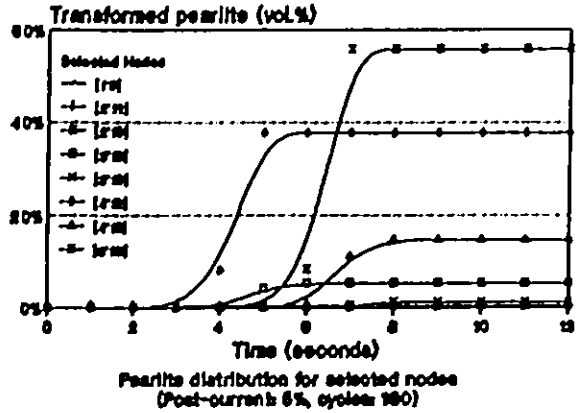

(b)

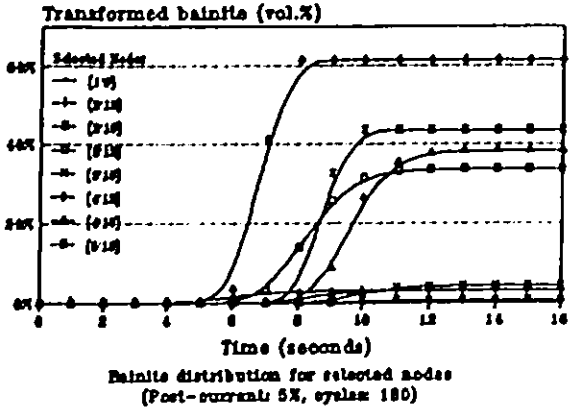

(c)

Fig.8-5 Diagrams for temperature distribution and microstructure development for selected nodes on cooling at post-weld heat: 5% of welding current, 180 cycles. (a) temperature vs time. (b) Transformed pearlite (vol.%) vs time. (c) Transformed bainite (vol.%) vs time.

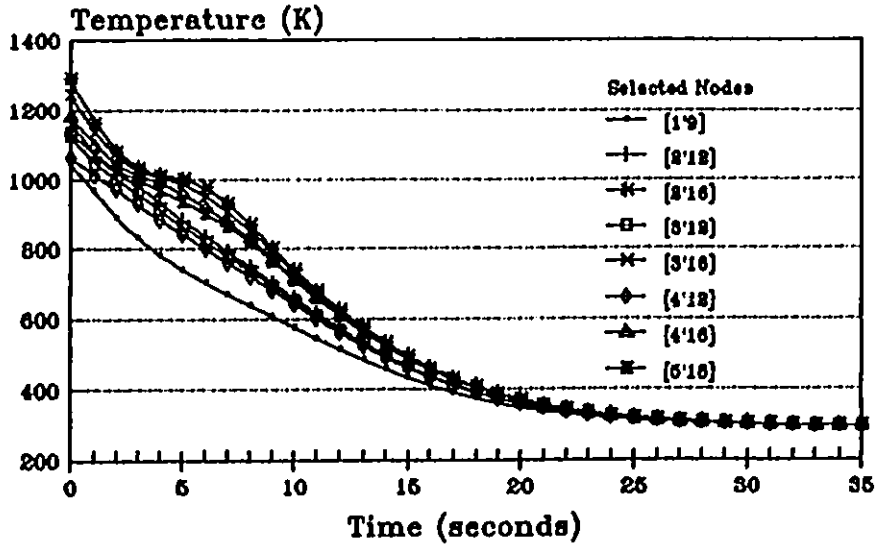

Cooling ourves for selected nodes
(Post-ourrent: 5%, oyoles: 720)

(a)

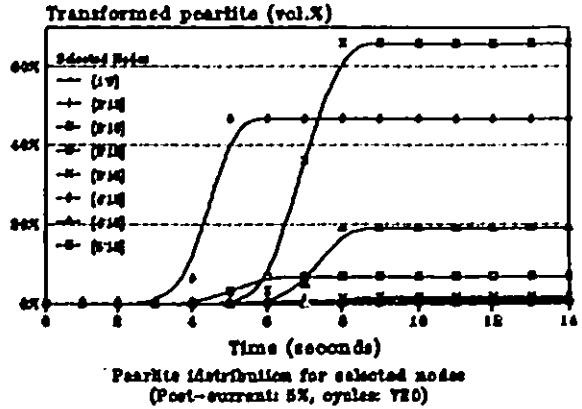

Pearlite distribution for selected nodes
(Post-current: 5%, cycles: 720)

(b)

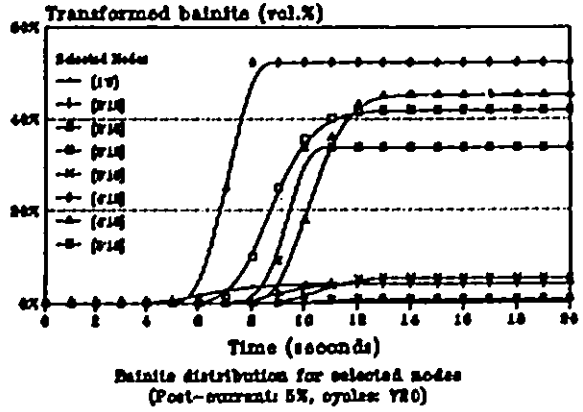

Bainite distribution for selected nodes
(Post-current: 5%, cycles: 720)

(c)

Fig.8-6 Diagrams for temperature distribution and microstructure development for selected nodes on cooling at post-weld heat: 5% of welding current, 720 cycles. (a) temperature vs time. (b) Transformed pearlite (vol.%) vs time. (c) Transformed bainite (vol.%) vs time.

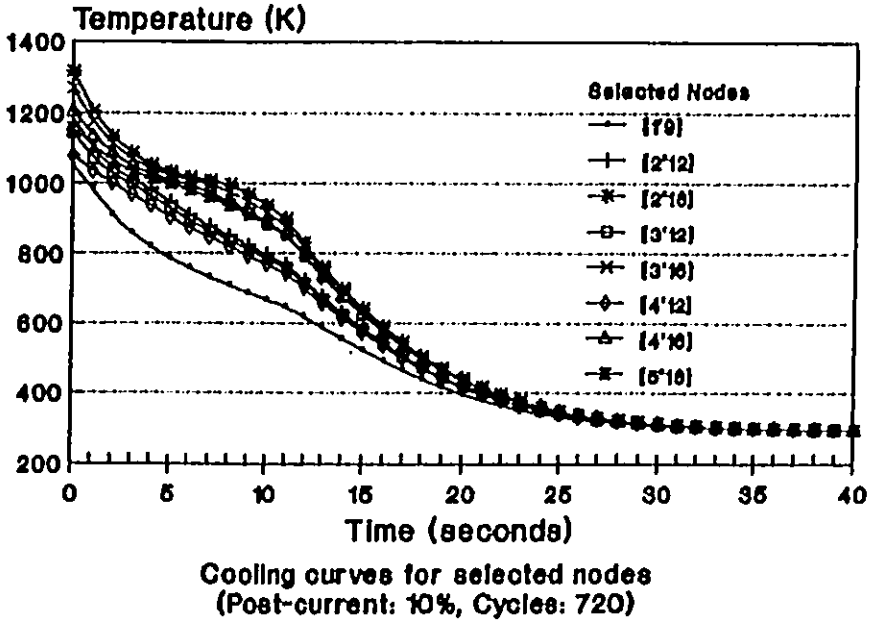

(a)

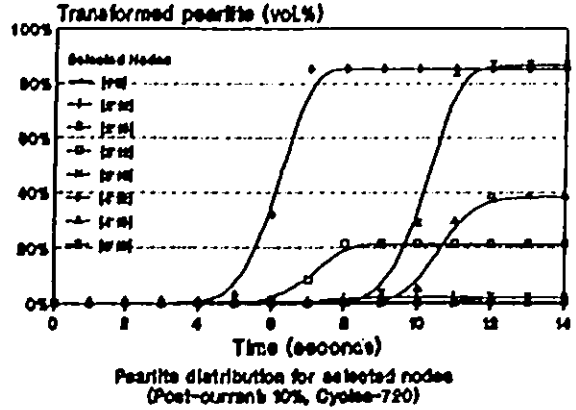

(b)

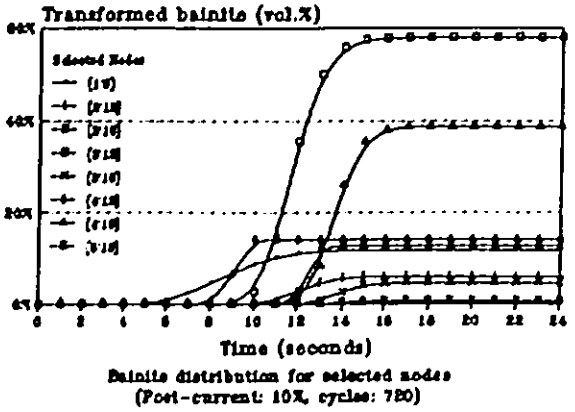

(c)

Fig.8-7 Diagrams for temperature distribution and microstructure development for selected nodes on cooling at post-weld heat: 10% of welding current, 720 cycles. (a) temperature vs time. (b) Transformed pearlite (vol.%) vs time. (c) Transformed bainite (vol.%) vs time.

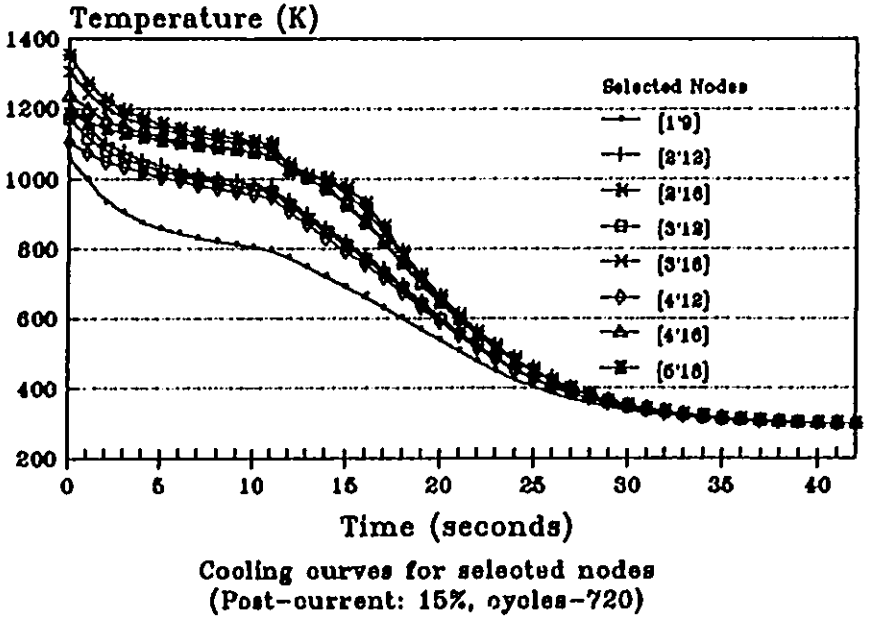

(a)

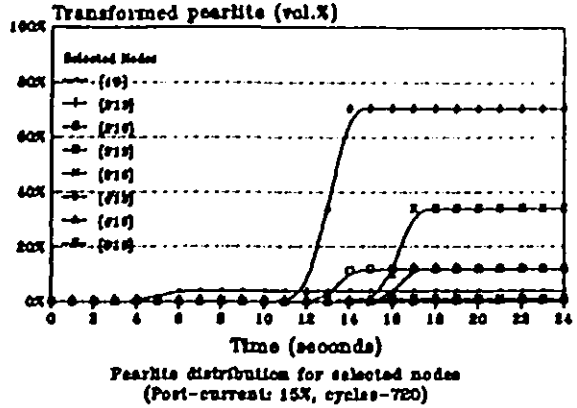

(b)

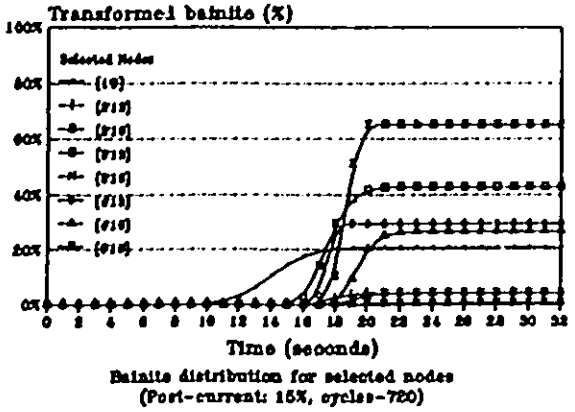

(c)

Fig.8-8 Diagrams for temperature distribution and microstructure development for selected nodes on cooling at post-weld heat: 15% of welding current, 720 cycles. (a) temperature vs time. (b) Transformed pearlite (vol.%) vs time. (c) Transformed bainite (vol.%) vs time.

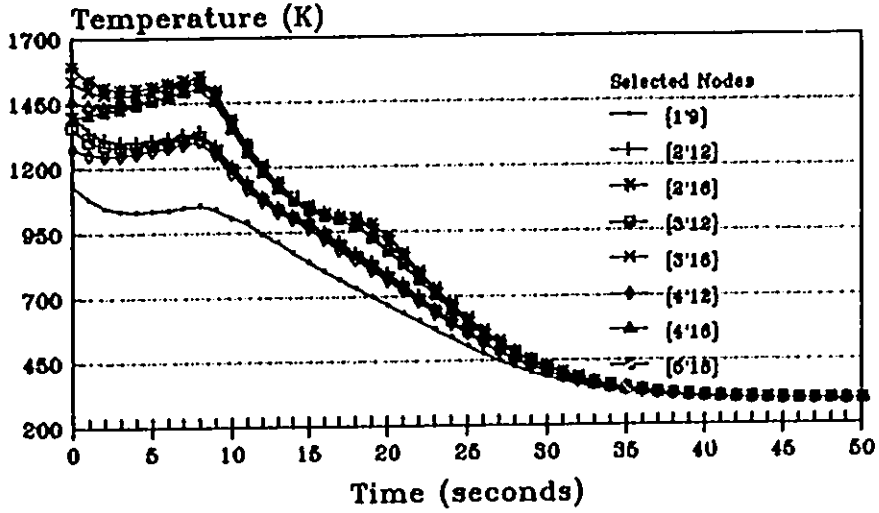

(a)

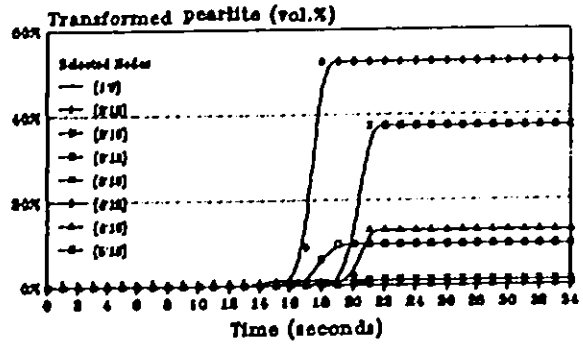

(b)

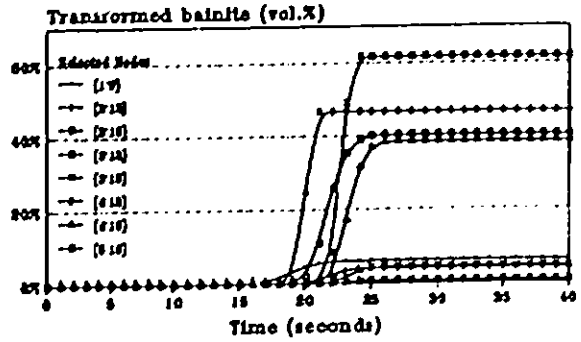

(c)

Fig.8-9 Diagrams for temperature distribution and microstructure development for selected nodes on cooling at post-weld heat: (part I) 40-20% of welding current, 70 cycles, and (part II) 20%, 495 cycles. (a) temperature vs time. (b) Transformed pearlite (vol.%) vs time. (c) Transformed bainite (vol.%) vs time.

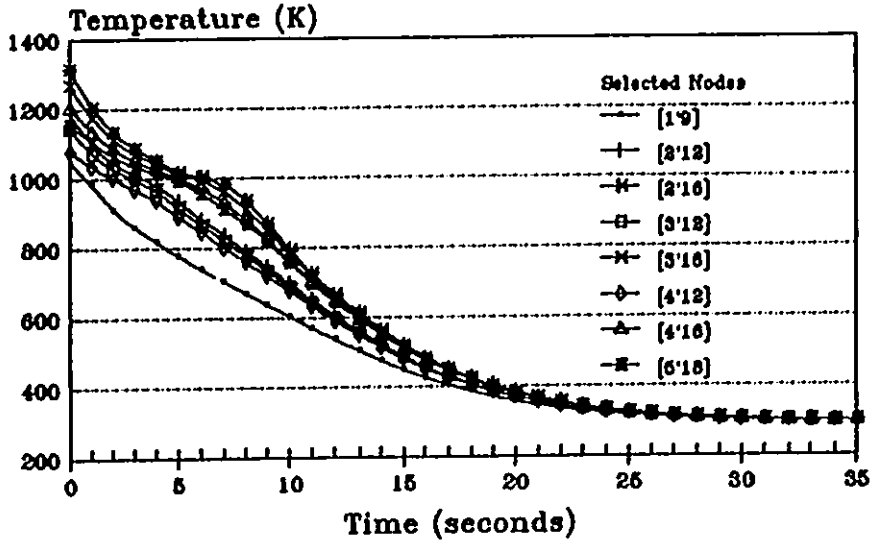

Cooling curves for selected nodes
(Post-current: 10%, cycles: 300)

(a)

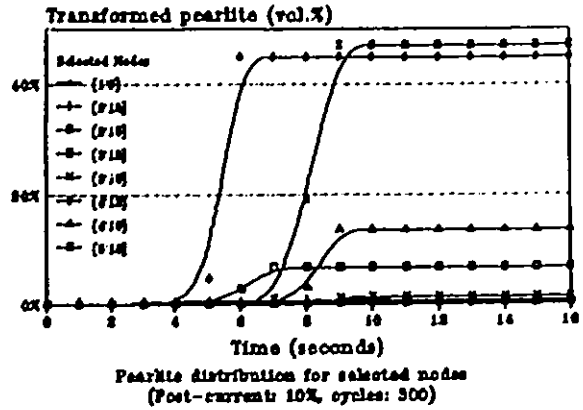

Pearlite distribution for selected nodes
(Post-current: 10%, cycles: 300)

(b)

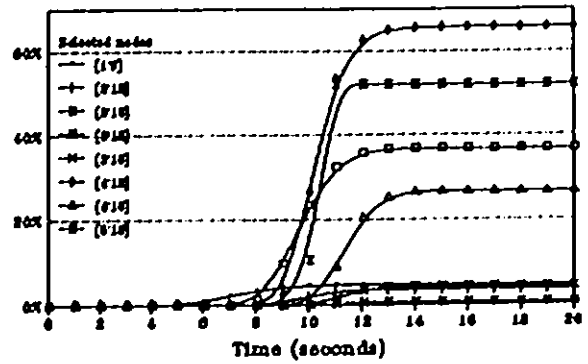

Bainite distribution for selected nodes
(Post-current: 10%, cycles: 300)

(c)

Fig.8-10 Diagrams for temperature distribution and microstructure development for selected nodes on cooling at post-weld heat: 10% of welding current, 300 cycles. (a) temperature vs time. (b) Transformed pearlite (vol.%) vs time. (c) Transformed bainite (vol.%) vs time.

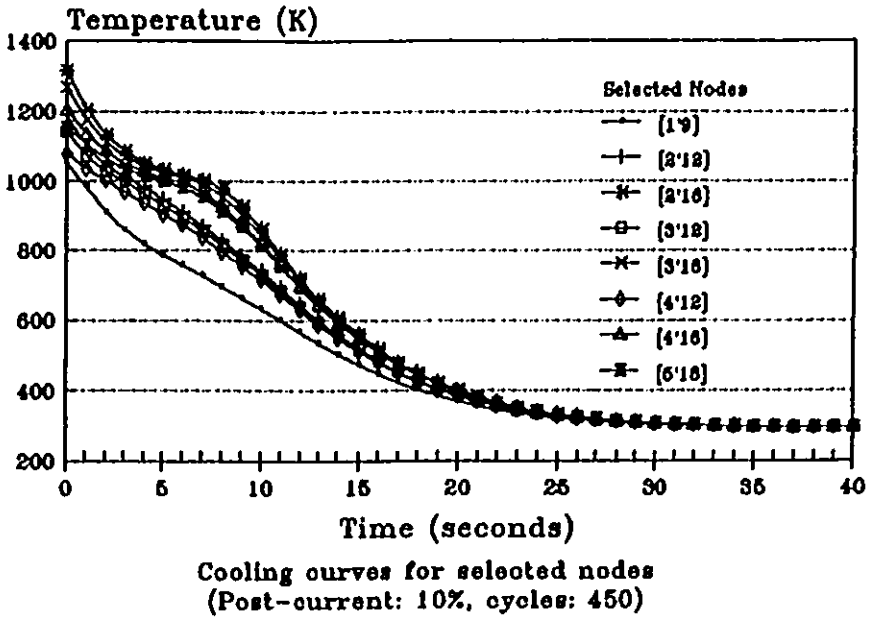

(a)

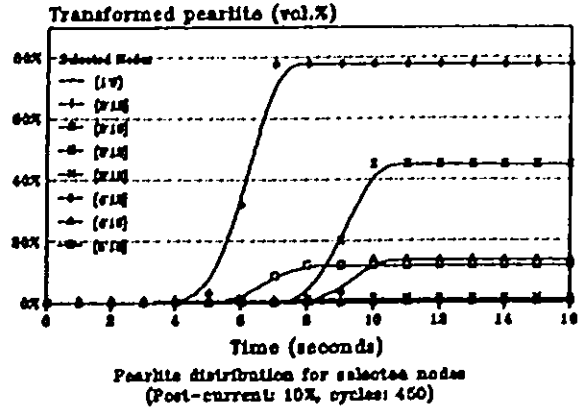

(b)

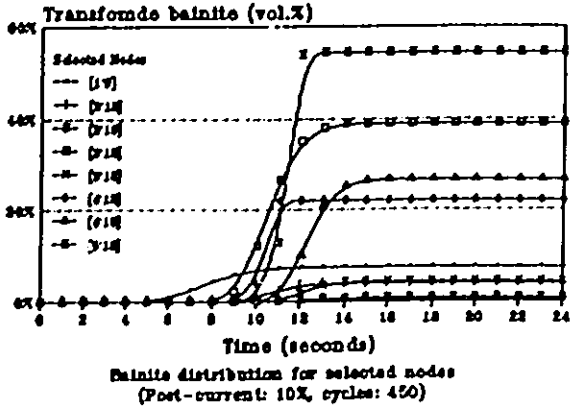

(c)

Fig.8-11 Diagrams for temperature distribution and microstructure development for selected nodes on cooling at post-weld heat: 10% of welding current, 450 cycles. (a) temperature vs time. (b) Transformed pearlite (vol.%) vs time. (c) Transformed bainite (vol.%) vs time.

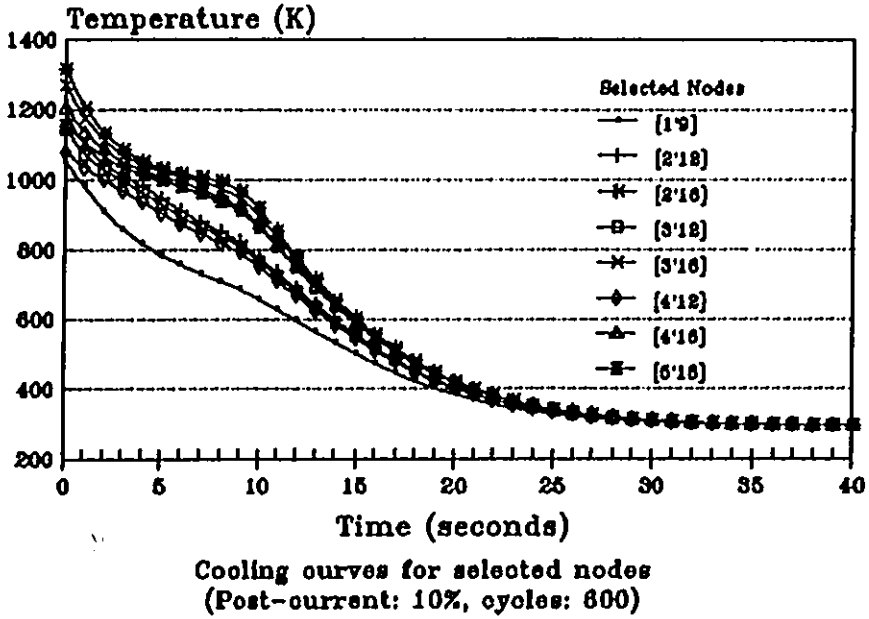

Cooling ourves for selected nodes
(Post-current: 10%, cycles: 600)

(a)

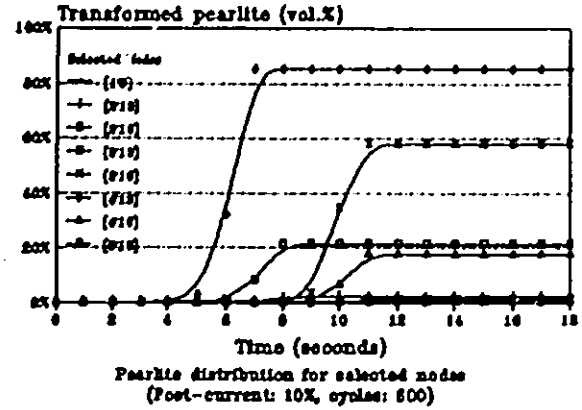

Pearlite distribution for selected nodes
(Post-current: 10%, cycles: 600)

(b)

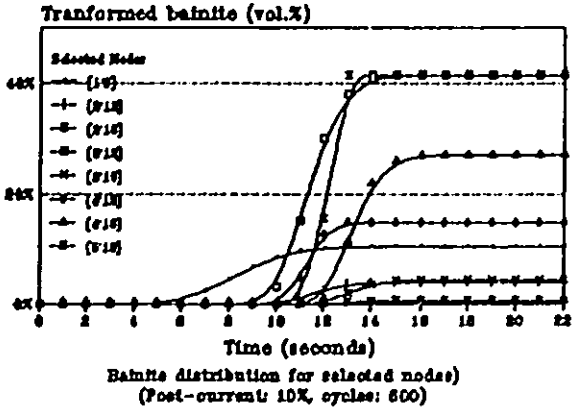

Bainite distribution for selected nodes)
(Post-current: 10%, cycles: 600)

(c)

Fig.8-12 Diagrams for temperature distribution and microstructure development for selected nodes on cooling at post-weld heat: 10% of welding current, 600 cycles. (a) temperature vs time. (b) Transformed pearlite (vol.%) vs time. (c) Transformed bainite (vol.%) vs time.

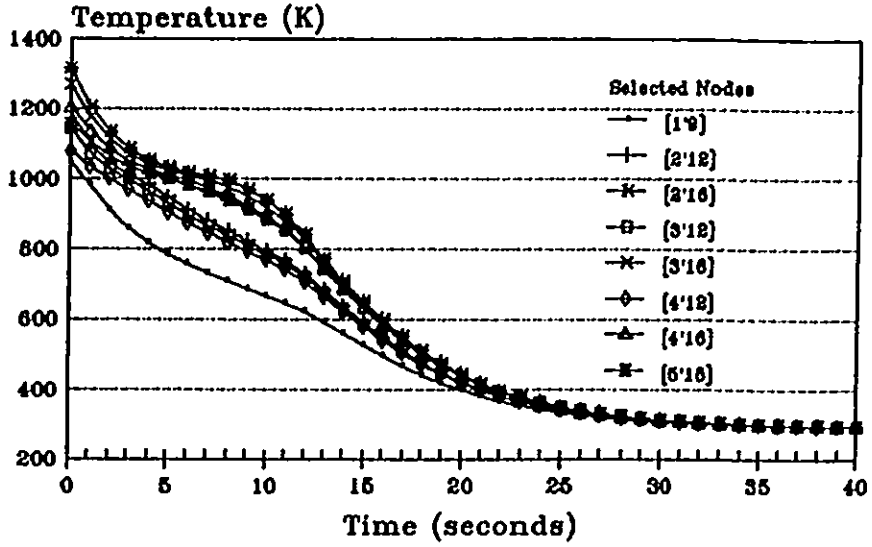

Cooling curves for selected nodes
(Post-current: 10%, cycles: 750)

(a)

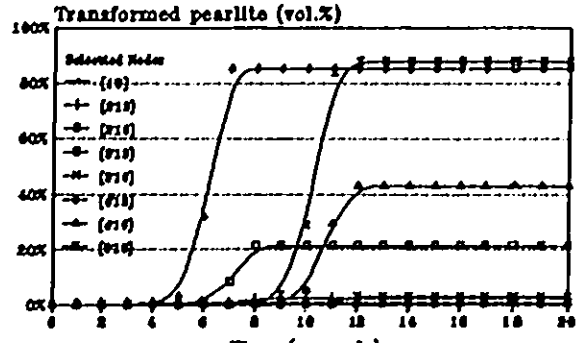

Pearlite distribution for selected nodes
(Post-current: 10%, cycles: 750)

(b)

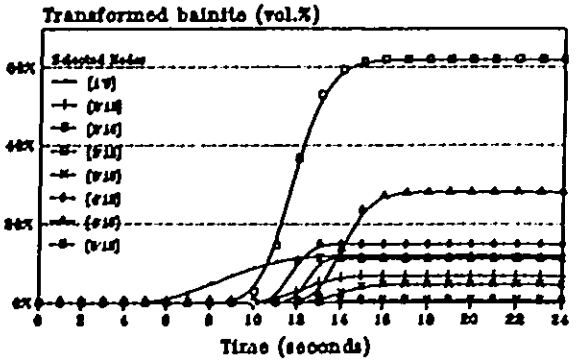

Bainite distribution for selected nodes
(Post-current: 10%, cycles: 750)

(c)

Fig.8-13 Diagrams for temperature distribution and microstructure development for selected nodes on cooling at post-weld heat: 10% of welding current, 750 cycles. (a) temperature vs time. (b) Transformed pearlite (vol.%) vs time. (c) Transformed bainite (vol.%) vs time.

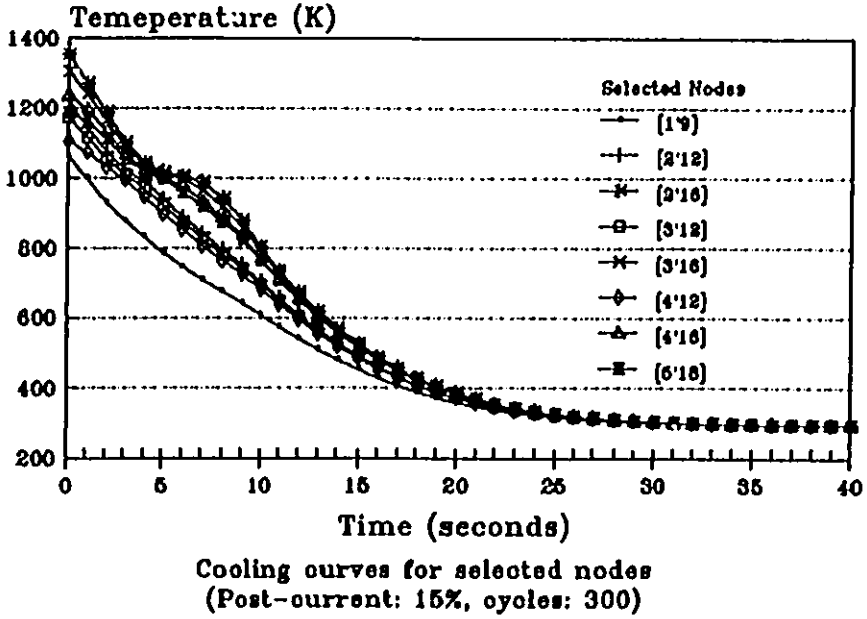

Cooling curves for selected nodes
(Post-current: 15%, cycles: 300)

(a)

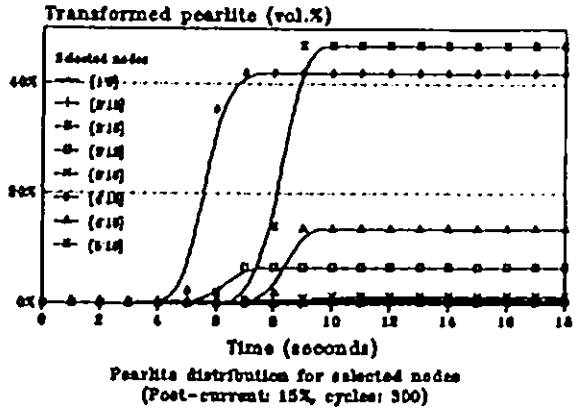

Pearlite distribution for selected nodes
(Post-current: 15%, cycles: 300)

(b)

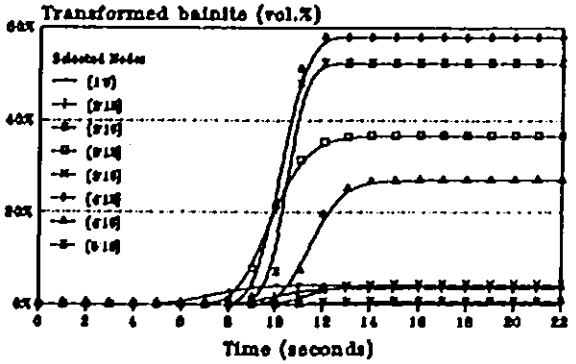

Bainite distribution for selected nodes
(Post-current: 15%, cycles: 300)

(c)

Fig.8-14 Diagrams for temperature distribution and microstructure development for selected nodes on cooling at post-weld heat: 15% of welding current, 300 cycles. (a) temperature vs time. (b) Transformed pearlite (vol.%) vs time. (c) Transformed bainite (vol.%) vs time.

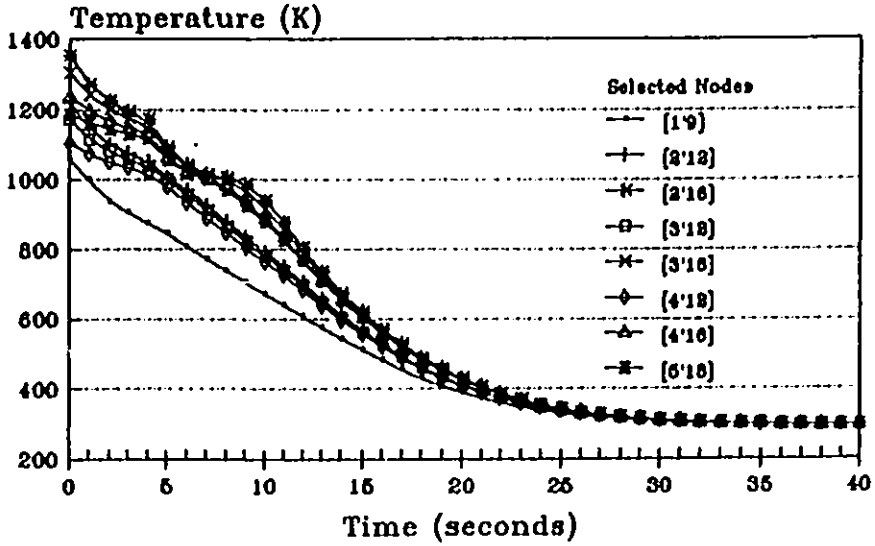

Cooling curves for selected nodes
(Post-current: 15%, cycles: 450)

(a)

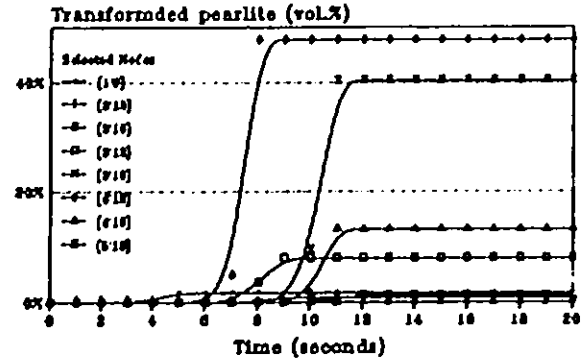

Pearlite distribution for selected nodes
(Post-current: 15%, cycles: 450)

(b)

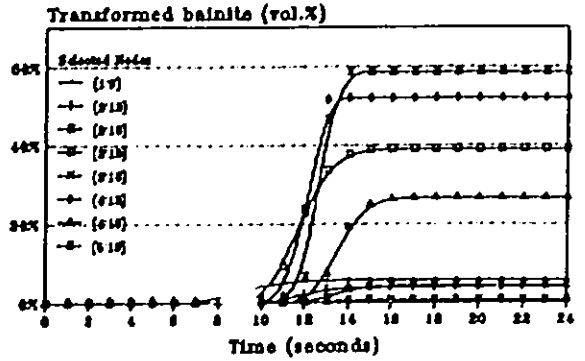

Bainite distribution for selected nodes
(Post-current: 15%, cycles: 450)

(c)

Fig.8-15 Diagrams for temperature distribution and microstructure development for selected nodes on cooling at post-weld heat: 15% of welding current, 450 cycles. (a) temperature vs time. (b) Transformed pearlite (vol.%) vs time. (c) Transformed bainite (vol.%) vs time.

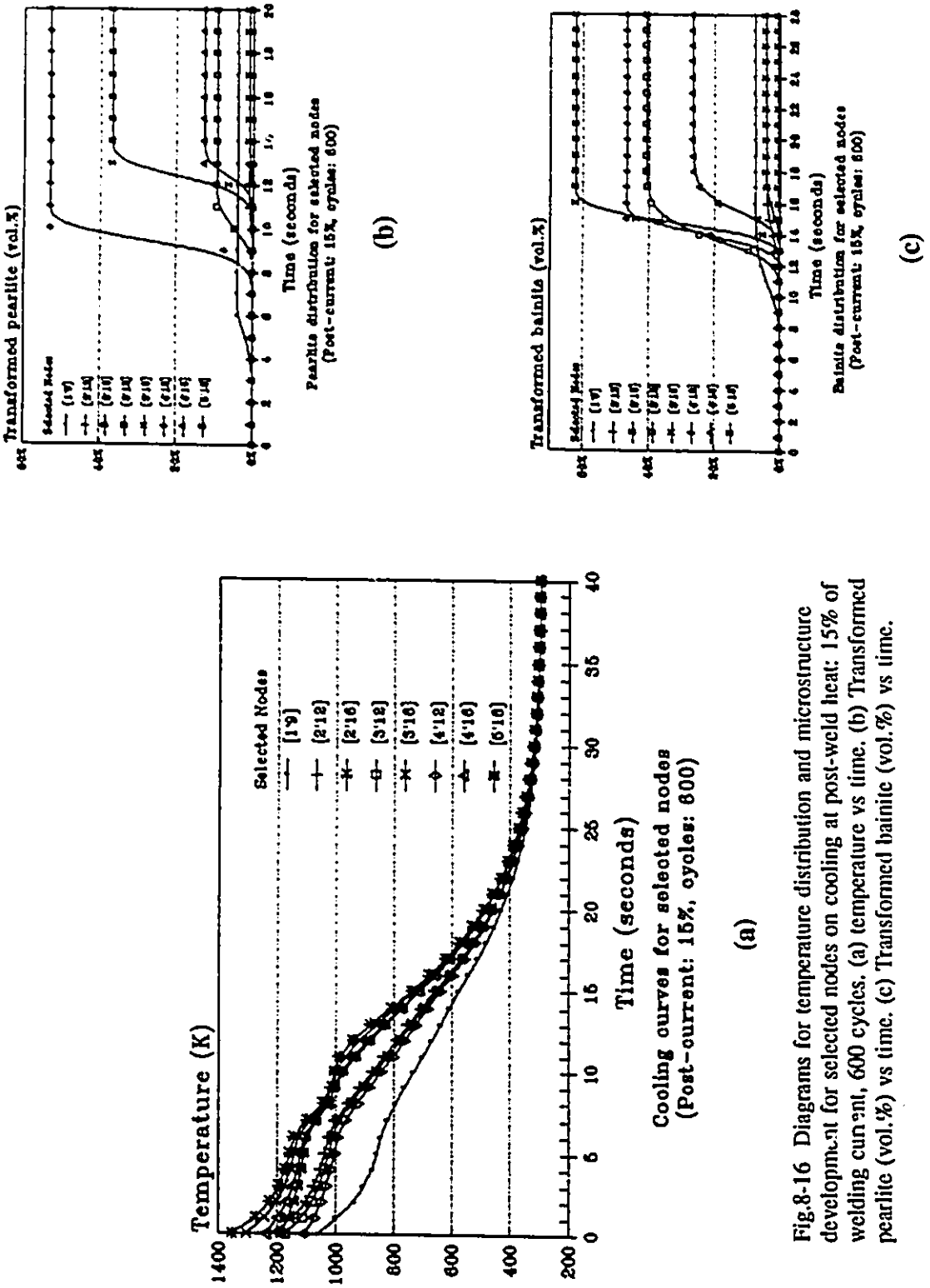

Fig.8-16 Diagrams for temperature distribution and microstructure development for selected nodes on cooling at post-weld heat: 15% of welding current, 600 cycles. (a) temperature vs time. (b) Transformed pearlite (vol.%) vs time. (c) Transformed bainite (vol.%) vs time.

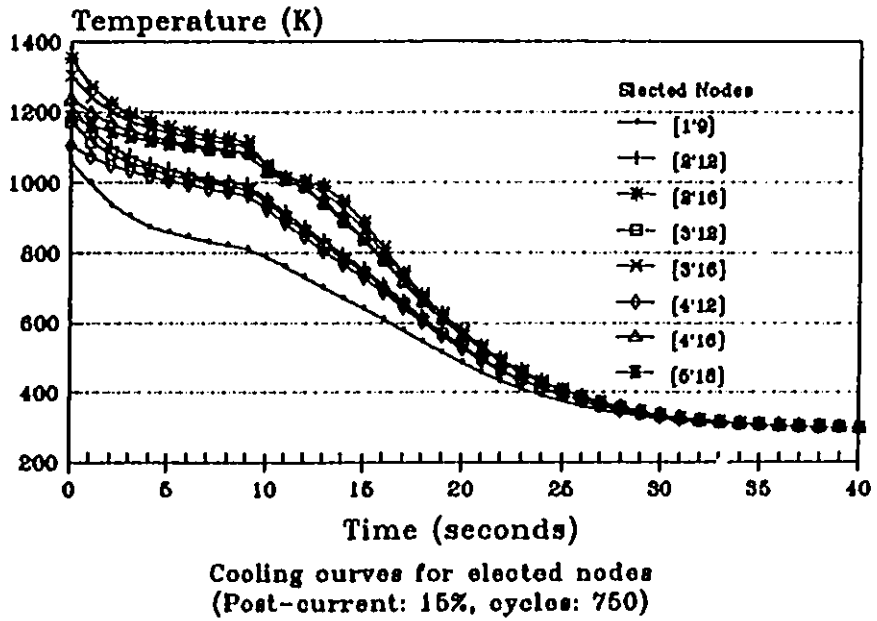

(a)

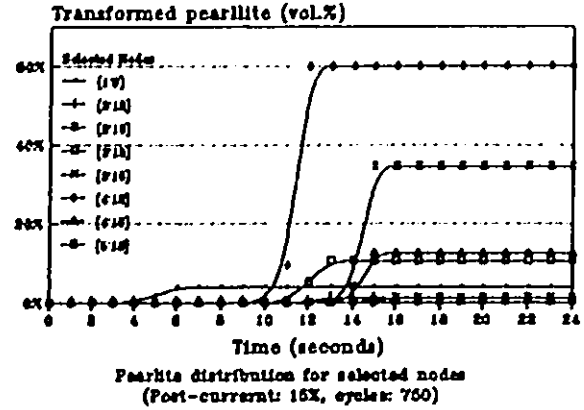

(b)

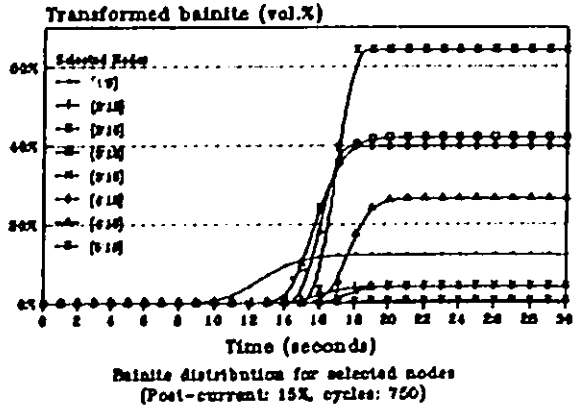

(c)

Fig.8-17 Diagrams for temperature distribution and microstructure development for selected nodes on cooling at post-weld heat: 15% of welding current, 750 cycles. (a) temperature vs time. (b) Transformed pearlite (vol.%) vs time. (c) Transformed bainite (vol.%) vs time.

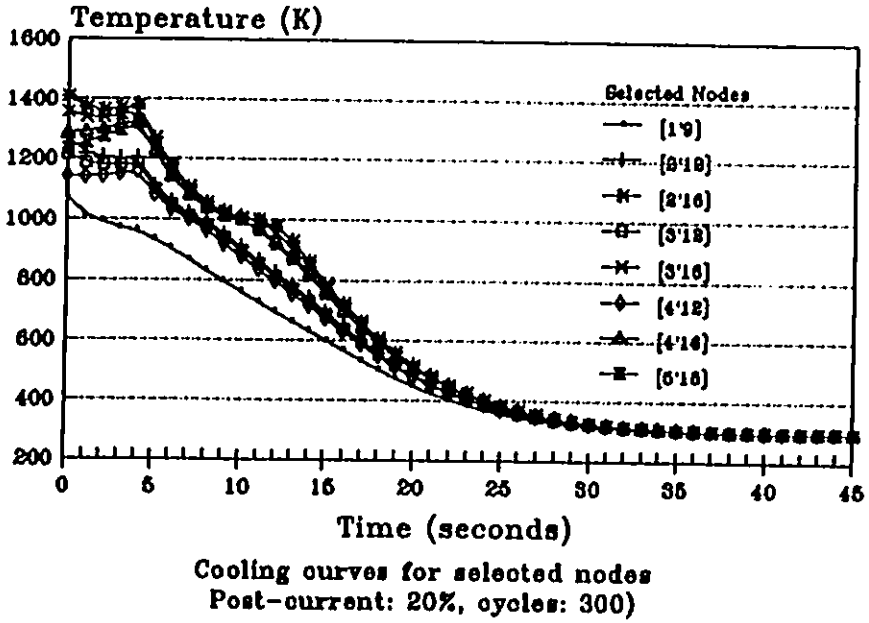

Cooling curves for selected nodes
Post-current: 20%, cycles: 300)

(a)

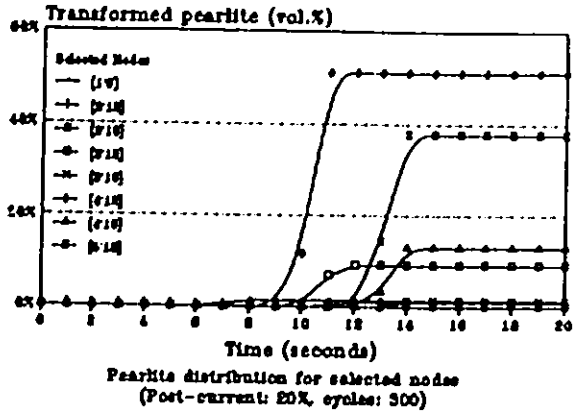

Pearlite distribution for selected nodes
(Post-current: 20%, cycles: 300)

(b)

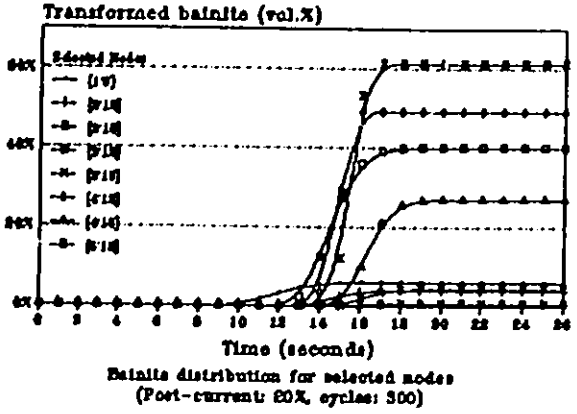

Bainite distribution for selected nodes
(Post-current: 20%, cycles: 300)

(c)

Fig.8-18 Diagrams for temperature distribution and microstructure development for selected nodes on cooling at post-weld heat: 20% of welding current, 300 cycles. (a) temperature vs time. (b) Transformed pearlite (vol.%) vs time. (c) Transformed bainite (vol.%) vs time.

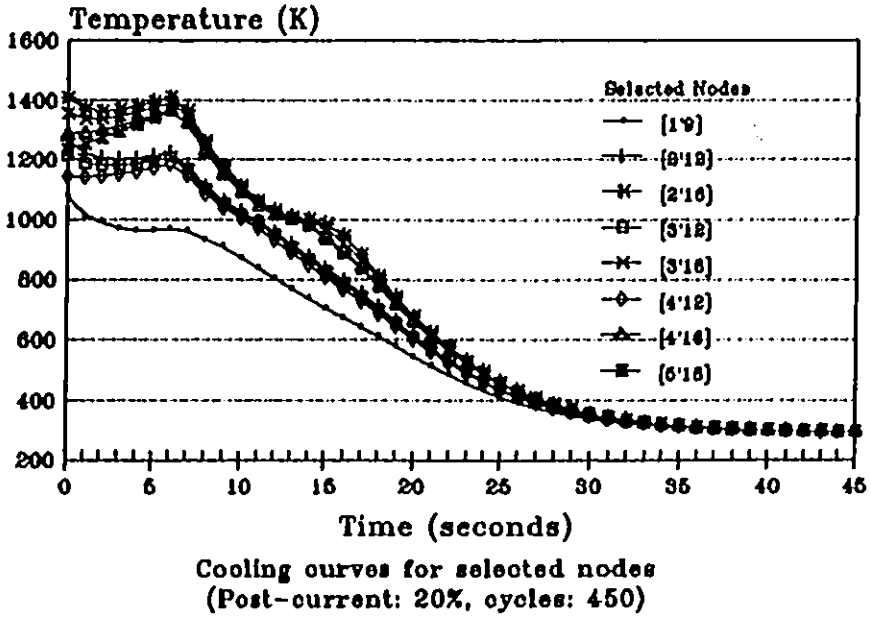

(a)

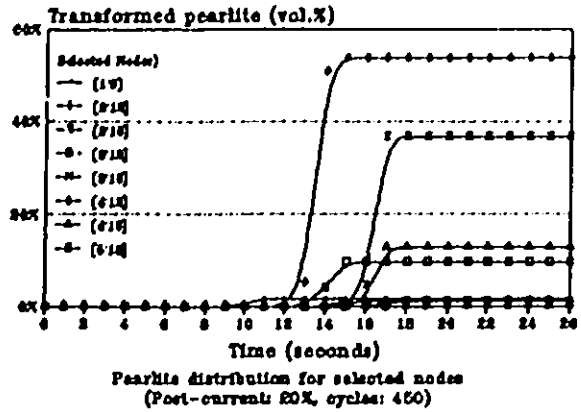

(b)

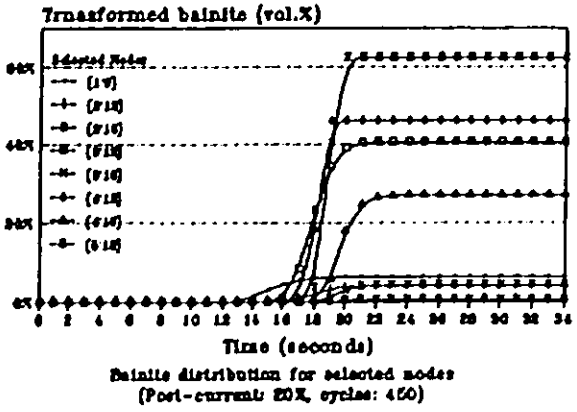

(c)

Fig.8-19 Diagrams for temperature distribution and microstructure development for selected nodes on cooling at post-weld heat: 20% of welding current, 450 cycles. (a) temperature vs time. (b) Transformed pearlite (vol.%) vs time. (c) Transformed bainite (vol.%) vs time.

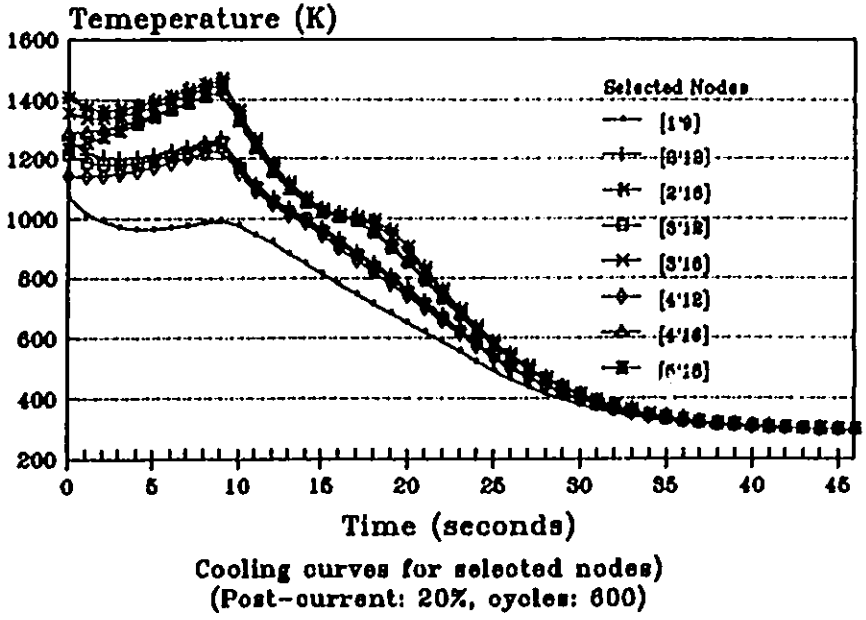

(a)

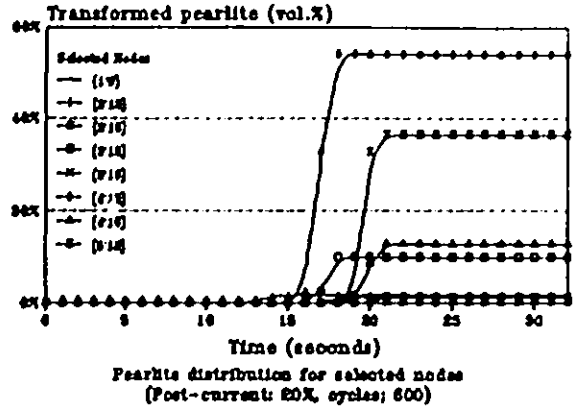

(b)

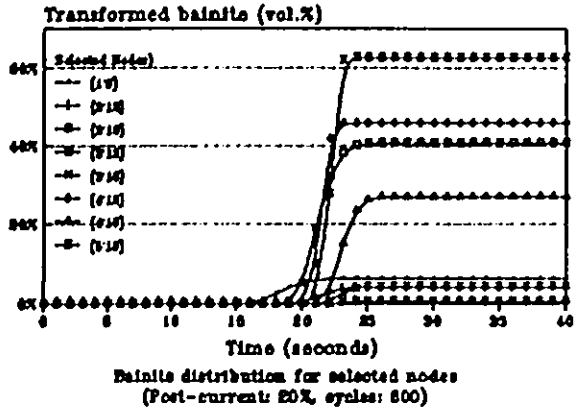

(c)

Fig.8-20 Diagrams for temperature distribution and microstructure development for selected nodes on cooling at post-weld heat: 20% of welding current, 600 cycles. (a) temperature vs time. (b) Transformed pearlite (vol.%) vs time. (c) Transformed bainite (vol.%) vs time.

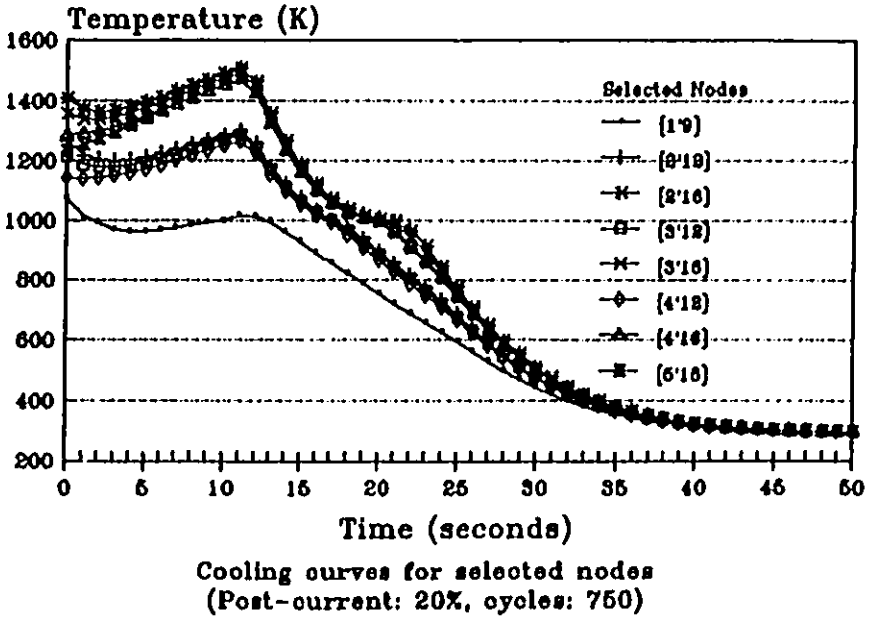

(a)

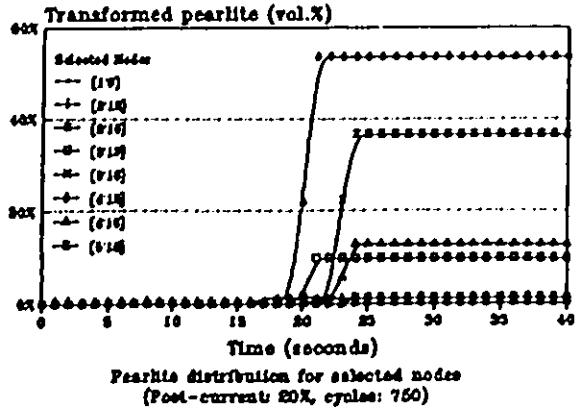

(b)

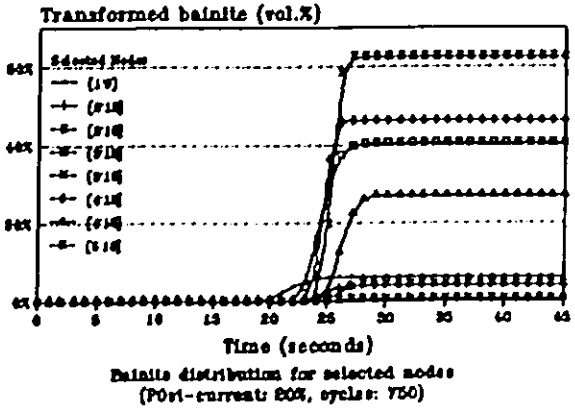

(c)

Fig.8-21 Diagrams for temperature distribution and microstructure development for selected nodes on cooling at post-weld heat: 20% of welding current, 750 cycles. (a) temperature vs time. (b) Transformed pearlite (vol.%) vs time. (c) Transformed bainite (vol.%) vs time.

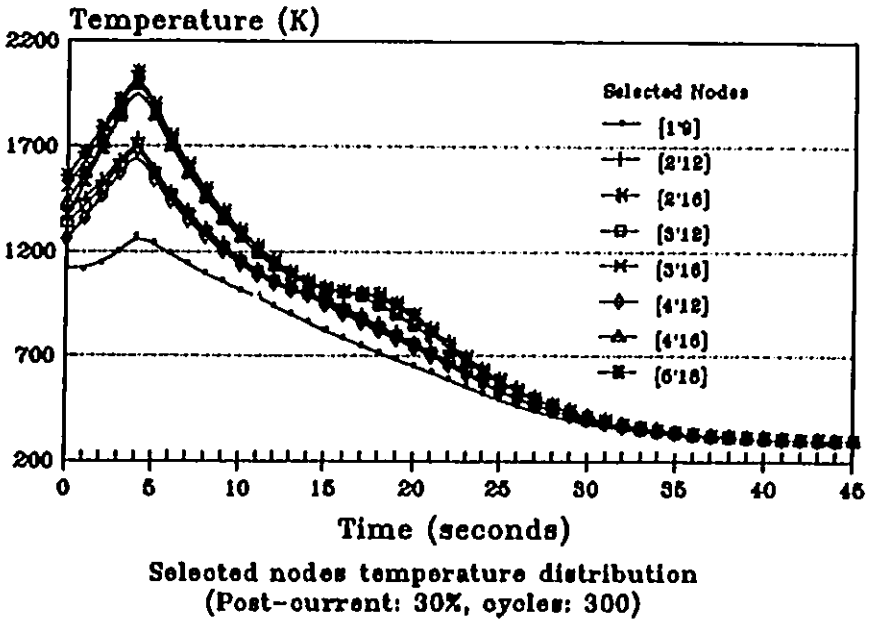

Selected nodes temperature distribution
(Post-current: 30%, cycles: 300)

(a)

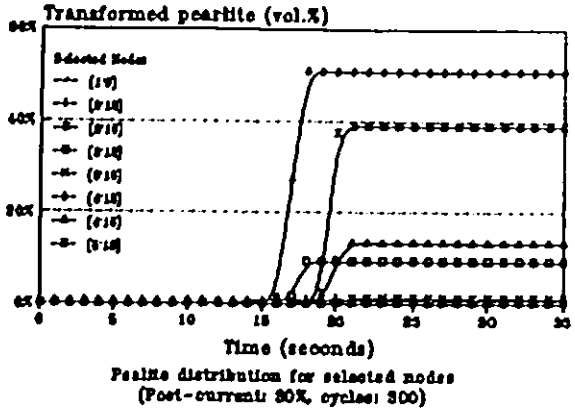

Pearlite distribution for selected nodes
(Post-current: 30%, cycles: 300)

(b)

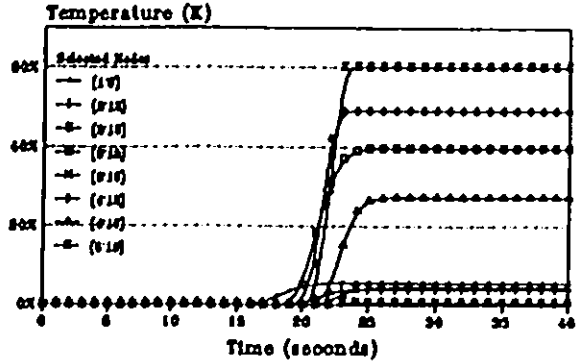

Bainite distribution for selected nodes
(Post-current: 30%, cycles: 300)

(c)

Fig.8-22 Diagrams for temperature distribution and microstructure development for selected nodes on cooling at post-weld heat: 30% of welding current, 300 cycles. (a) temperature vs time. (b) Transformed pearlite (vol.%) vs time. (c) Transformed bainite (vol.%) vs time.

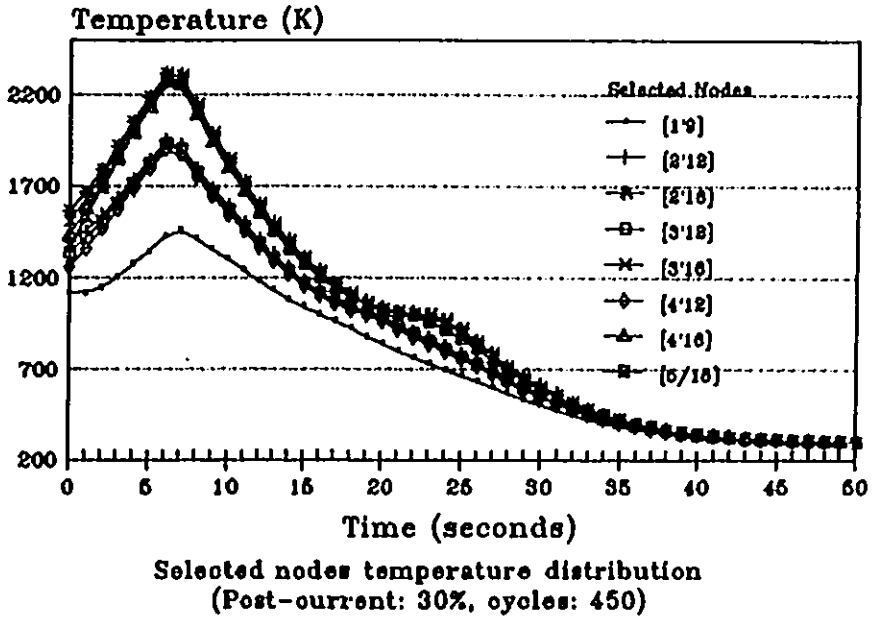

(a)

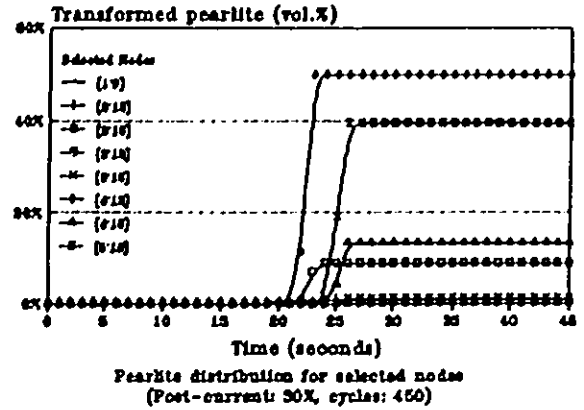

(b)

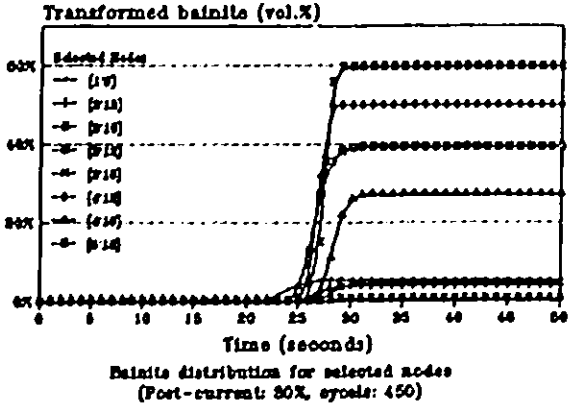

(c)

Fig.8-23 Diagrams for temperature distribution and microstructure development for selected nodes on cooling at post-weld heat: 30% of welding current, 450 cycles. (a) temperature vs time. (b) Transformed pearlite (vol.%) vs time. (c) Transformed bainite (vol.%) vs time.

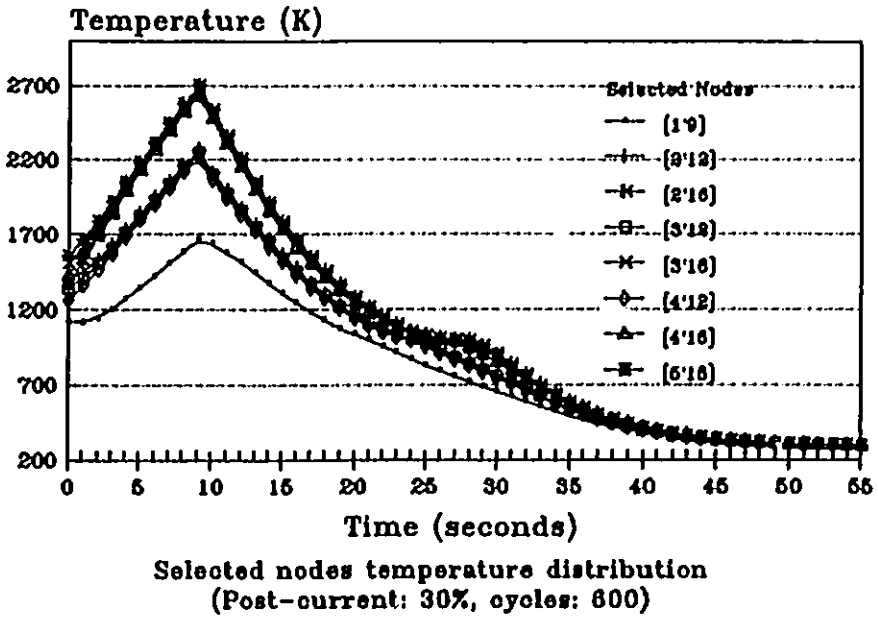

(a)

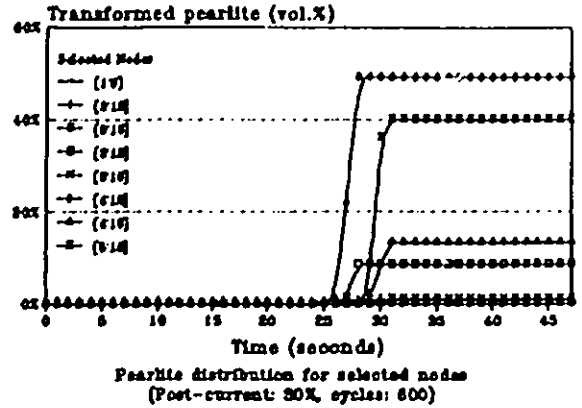

(b)

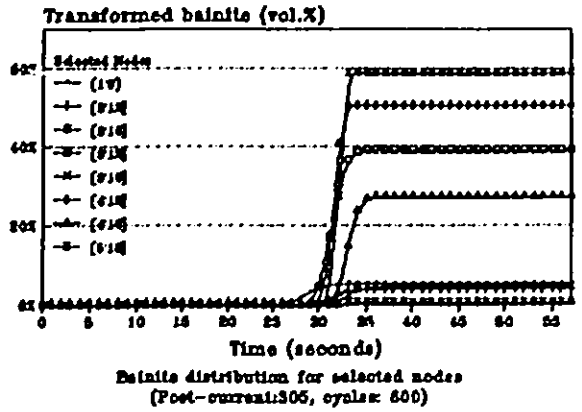

(c)

Fig.8-24 Diagrams for temperature distribution and microstructure development for selected nodes on cooling at post-weld heat: 30% of welding current, 600 cycles. (a) temperature vs time. (b) Transformed pearlite (vol.%) vs time. (c) Transformed bainite (vol.%) vs time.

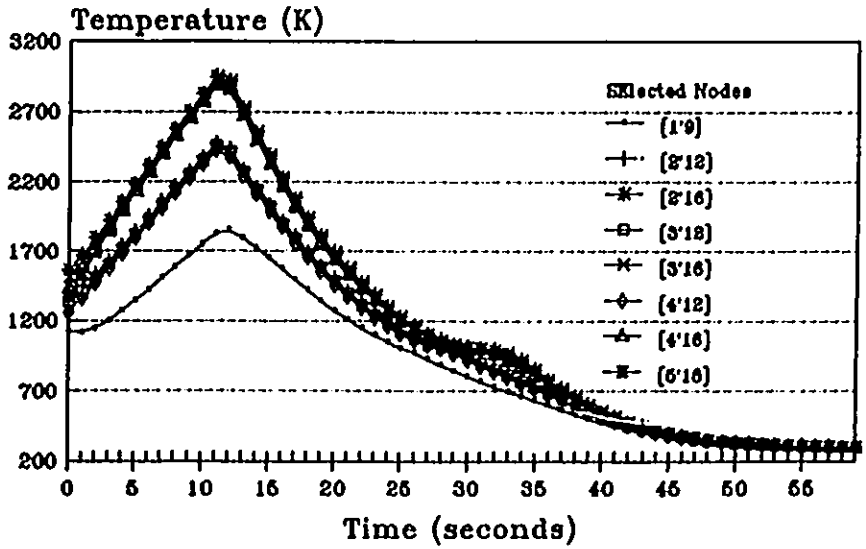

Selected nodes temperature distribution
(Post-current: 30%, cycles: 750)

(a)

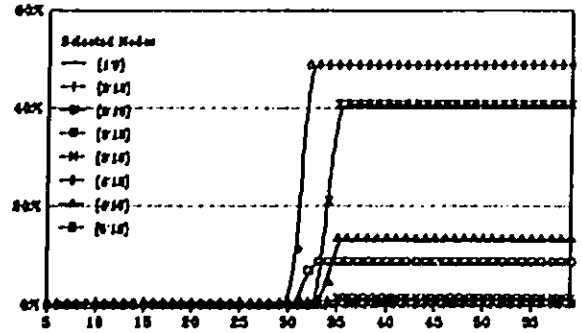

Pearlite distribution for selected nodes
(Post-current: 30%, cycles: 750)

(b)

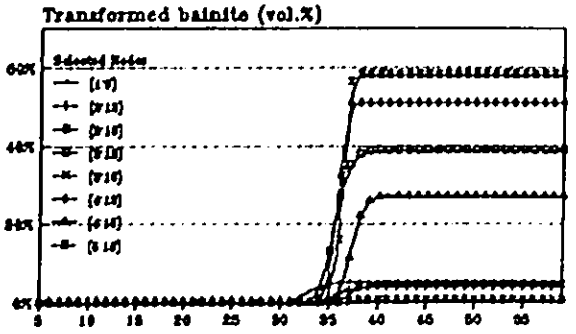

Bainite distribution for selected nodes
(Post-current: 30%, cycles: 750)

(c)

Fig.8-25 Diagrams for temperature distribution and microstructure development for selected nodes on cooling at post-weld heat: 30% of welding current, 750 cycles. (a) temperature vs time. (b) Transformed pearlite (vol.%) vs time. (c) Transformed bainite (vol.%) vs time.

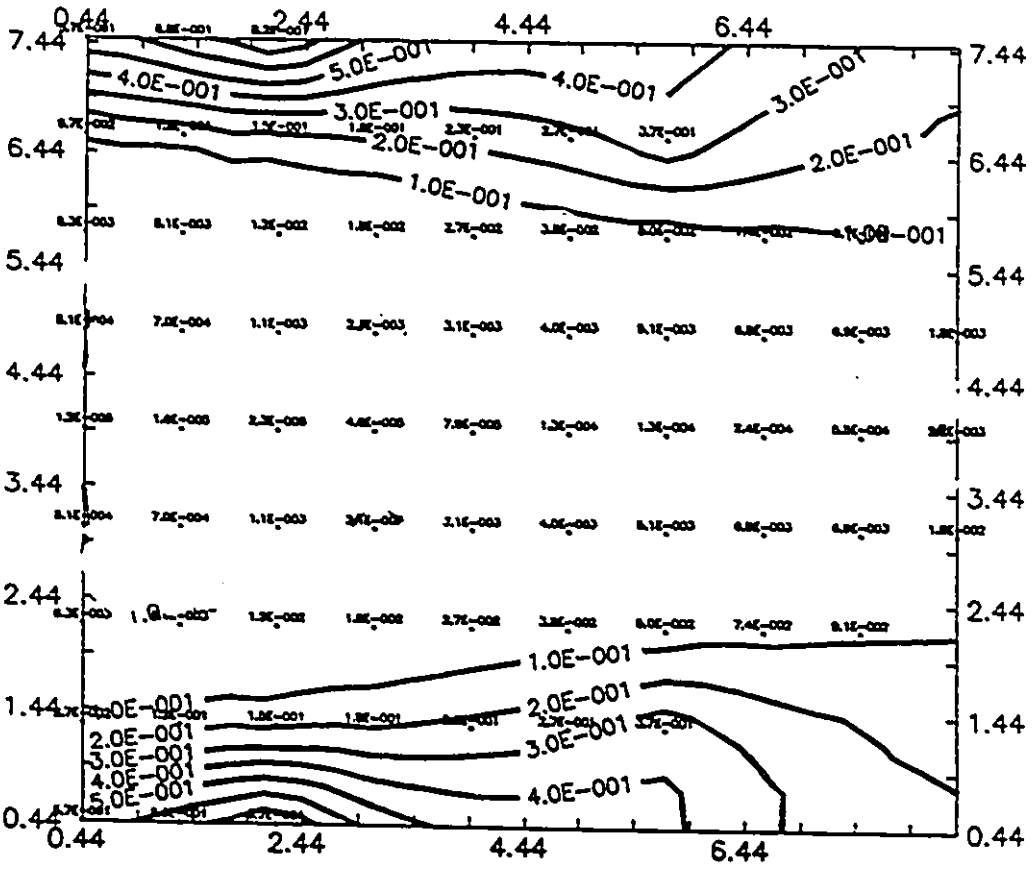

Fig.8-26 A map of pearlite distribution in the HAZ at the end of the welding. No post-weld heat. The x-coordinates n this figure is the mirror image of Fig. 8-3, and the y-coordinates are reflected about the faying surface across the horizontal centreline of this figure. Node 1,9 in the Fig.8-3 is on the right hand edge at the y-midpoint. Node 5,18 in the Fig.8-3 is at the lower left hand corner, and the upper left hand corner.

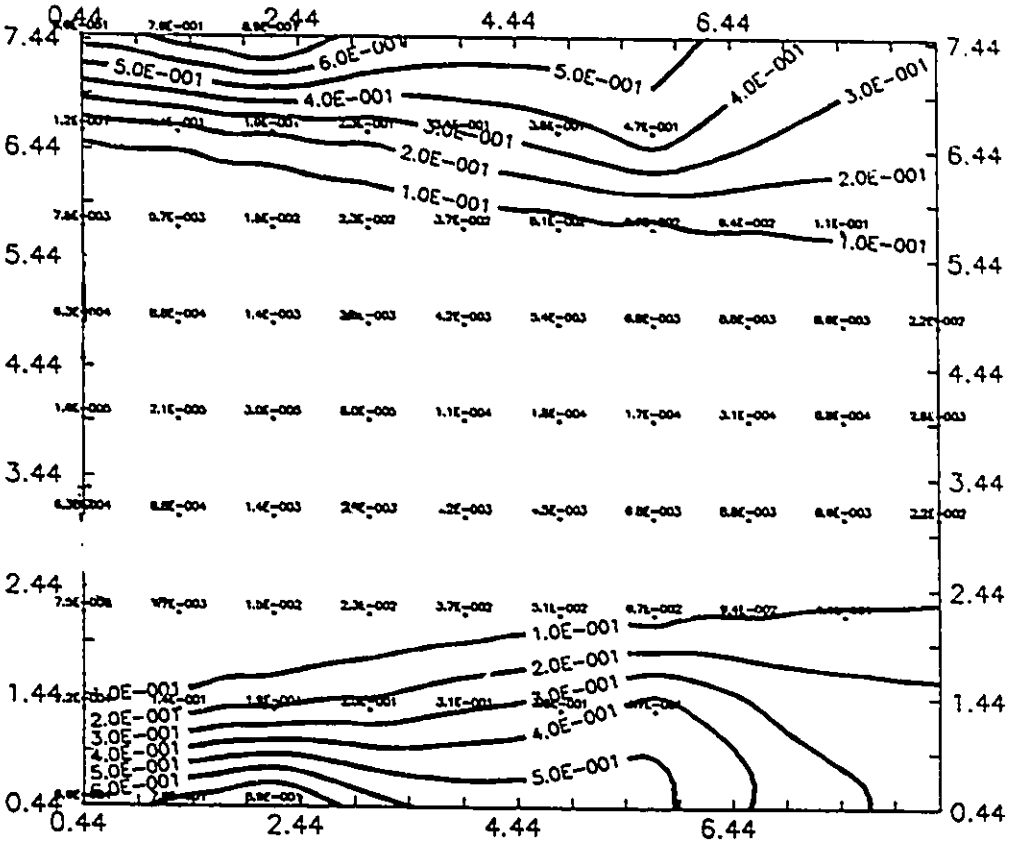

Fig.8-27 A map of pearlite distribution in the HAZ at the end of the welding. Post-weld heating: 5% of welding current, 720 cycles.

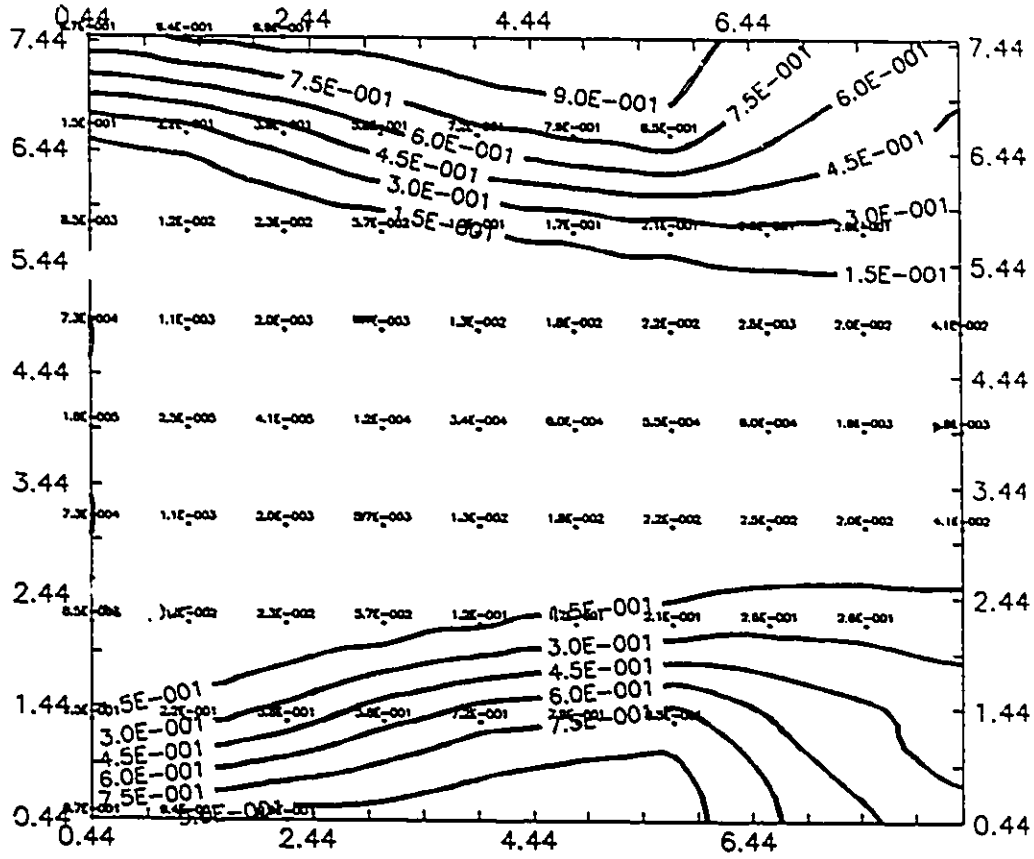

Fig.8-28 A map of pearlite distribution in the HAZ at the end of the welding. Post- weld heating: 10% of welding current, 720 cycles.

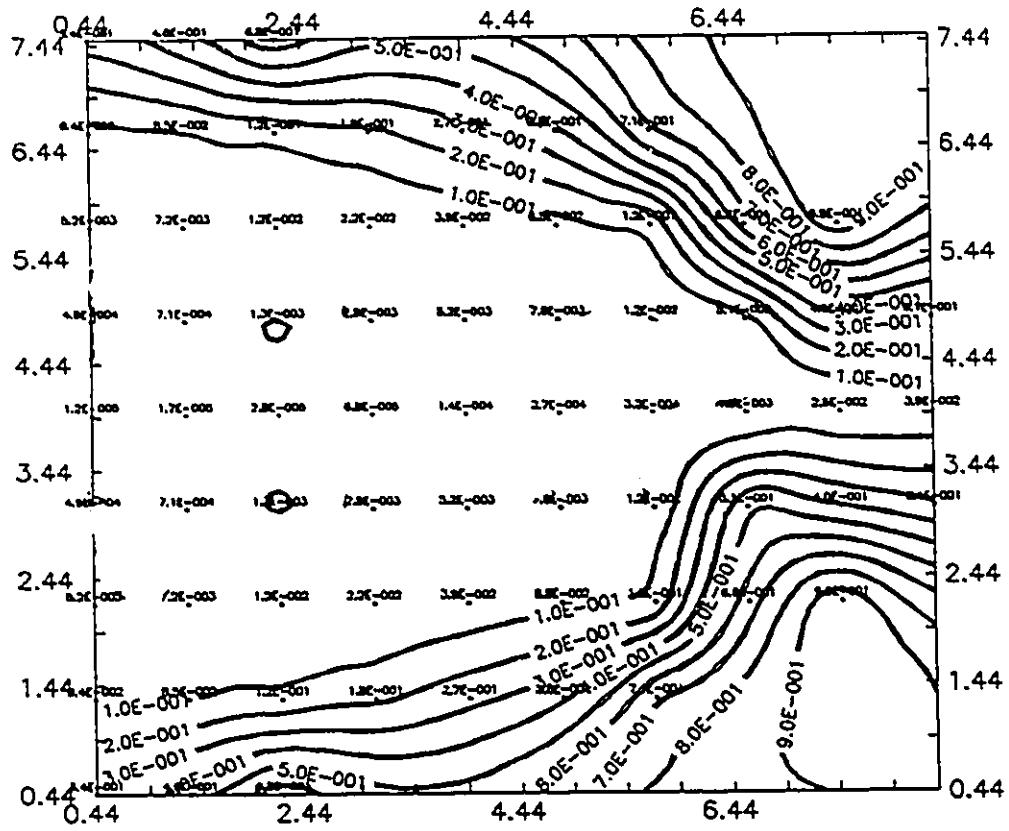

Fig.8-29 A map of pearlite distribution in the HAZ at the end of the welding. Post- weld heating: 15% of welding current, 720 cycles.

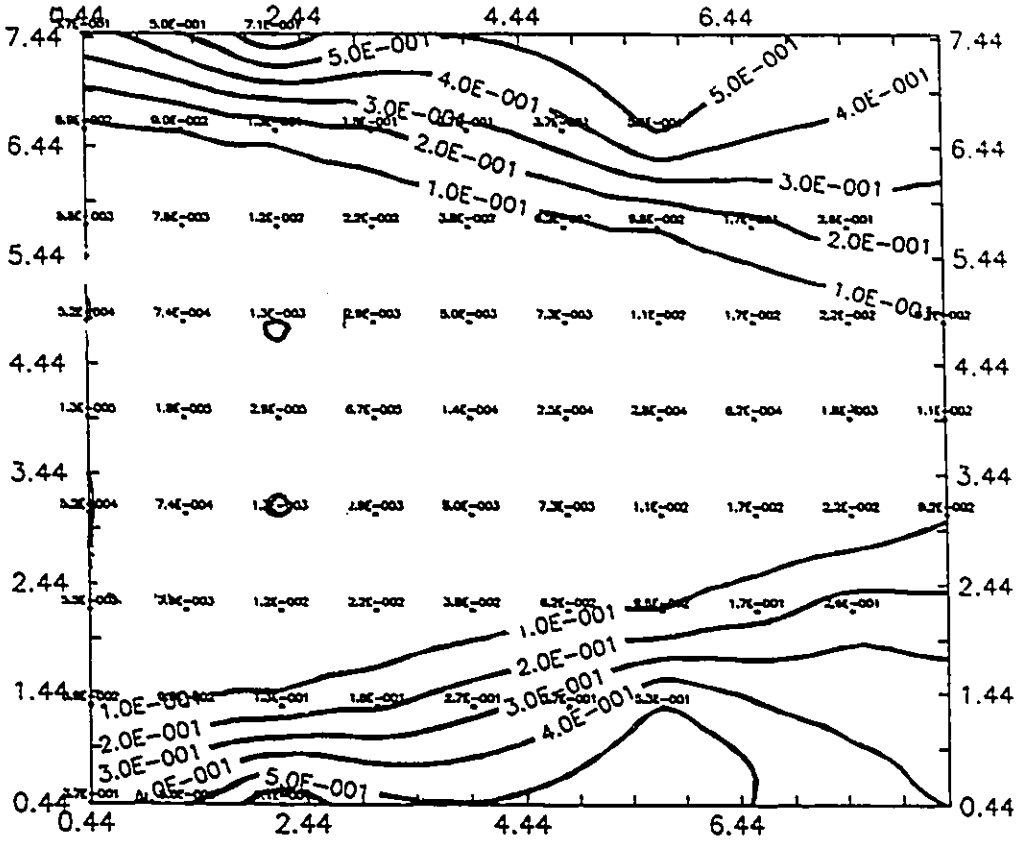

Fig. 8-30 A map of pearlite distribution in the HAZ at the end of the welding. Post-weld heating: Coschell standard welding cycles.

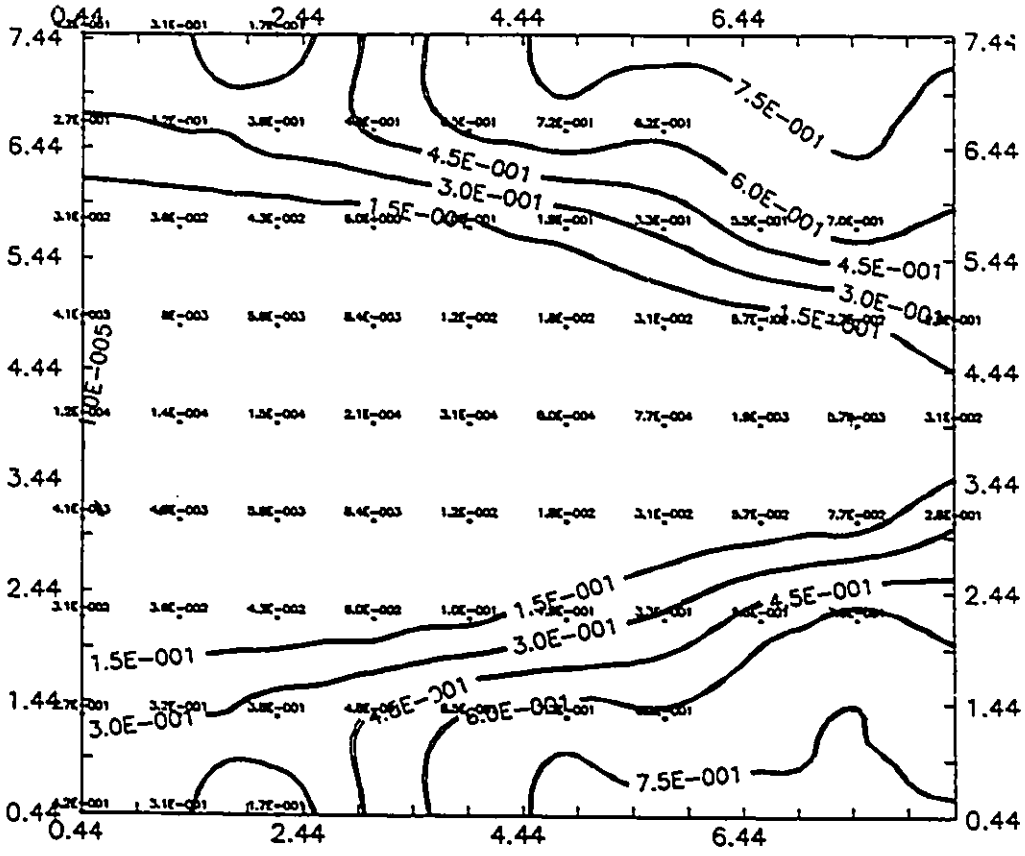

Fig.8-31 A map of bainite distribution in the HAZ at the end of the welding. No post-weld heat.

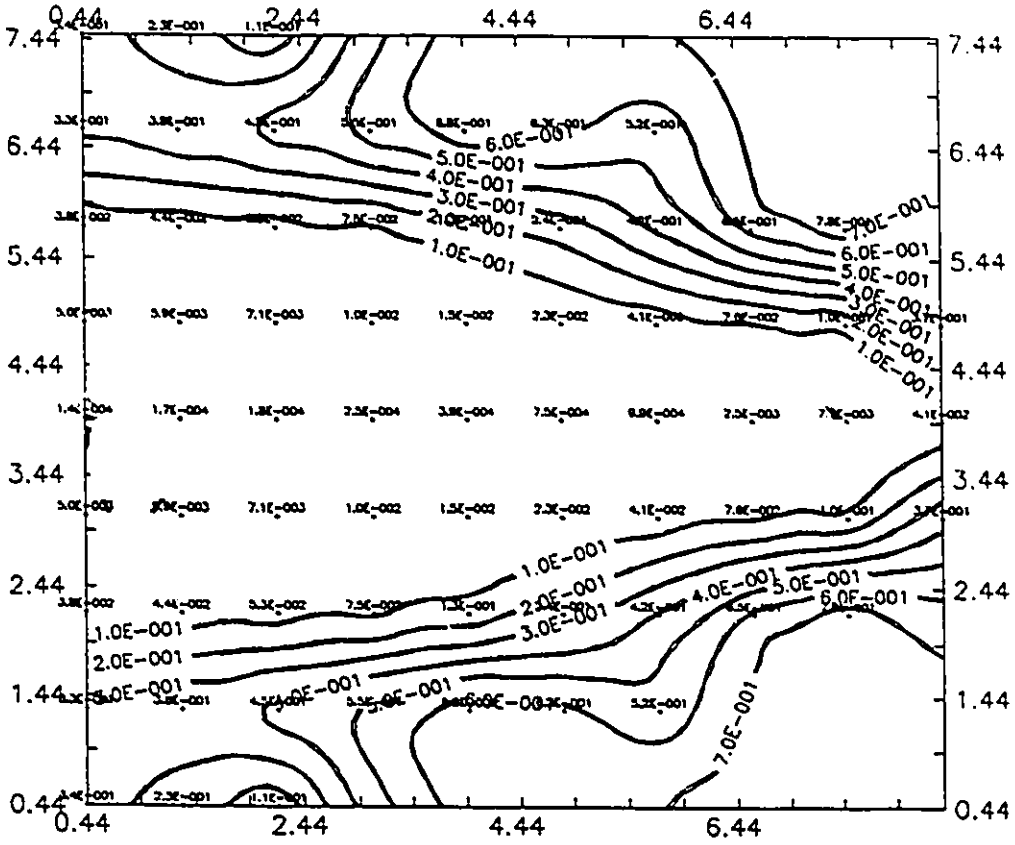

Fig. 8-32 A map of bainite distribution in the HAZ at the end of the welding. Post-weld heating: 5% of welding current, 720 cycles.

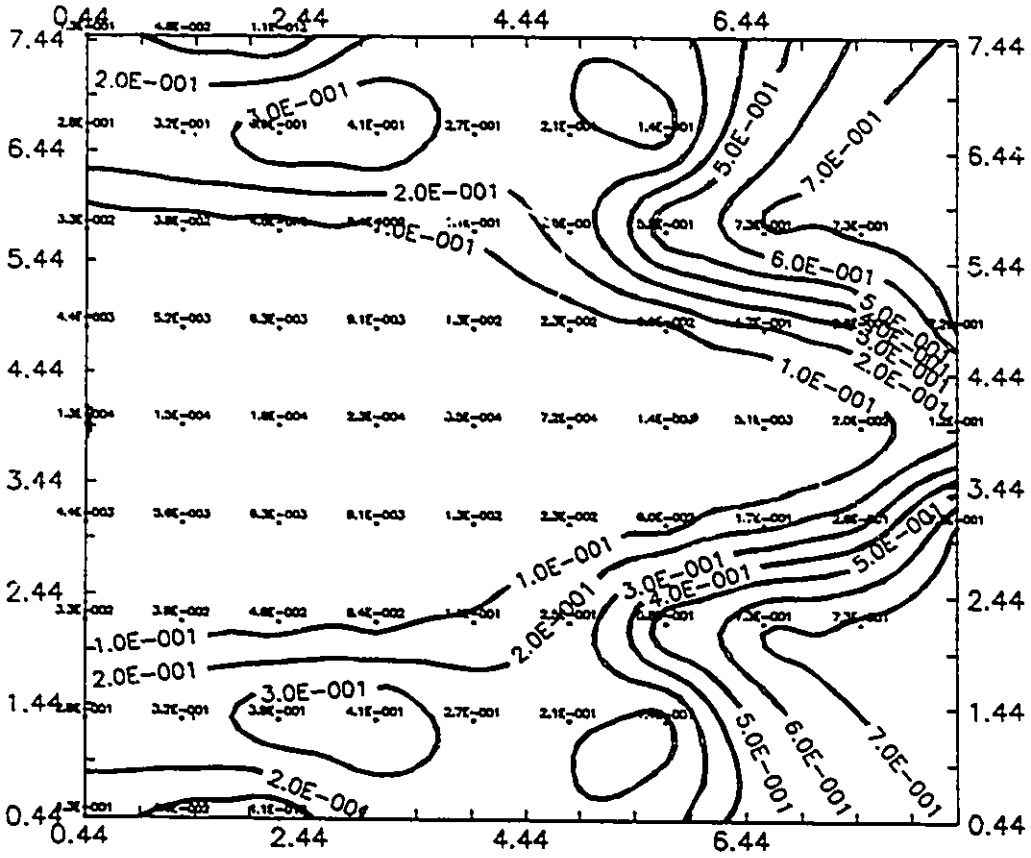

Fig. 8-33 A map of bainite distribution in the HAZ at the end of the welding. Post-weld heating: 10% of welding current, 720 cycles.

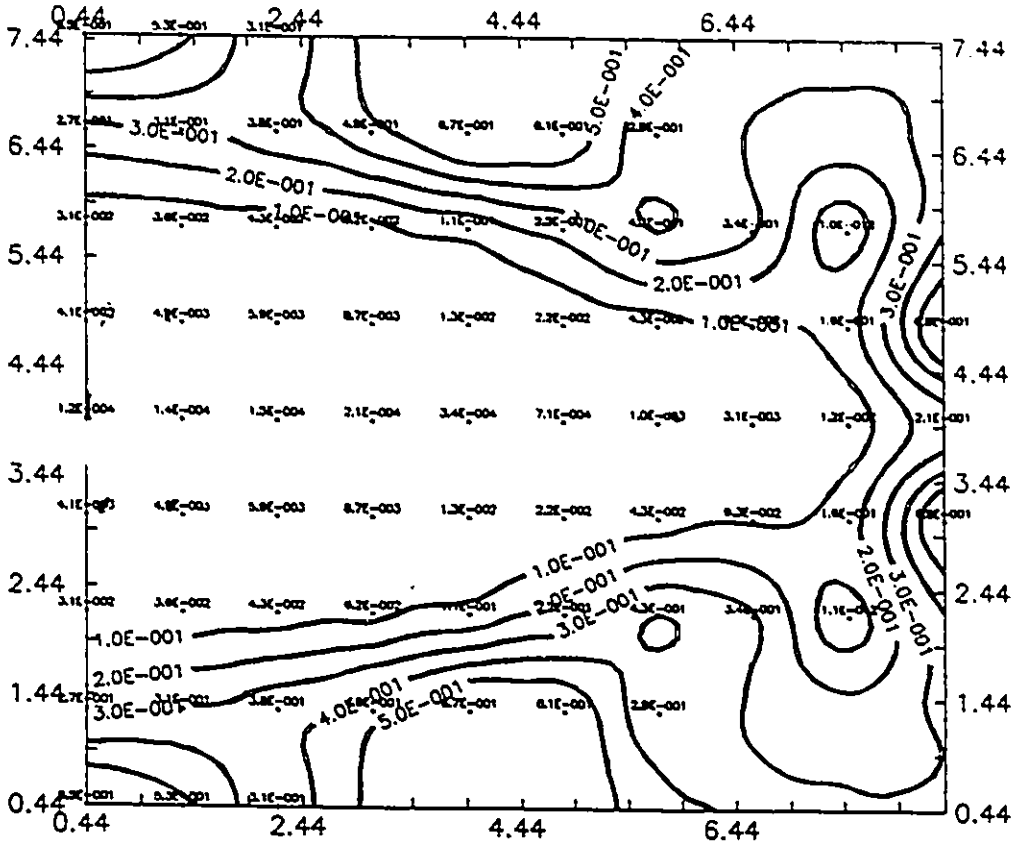

Fig. 8-34 A map of bainite distribution in the HAZ at the end of the welding. Post-weld heating: 15% of welding current, 720 cycles.

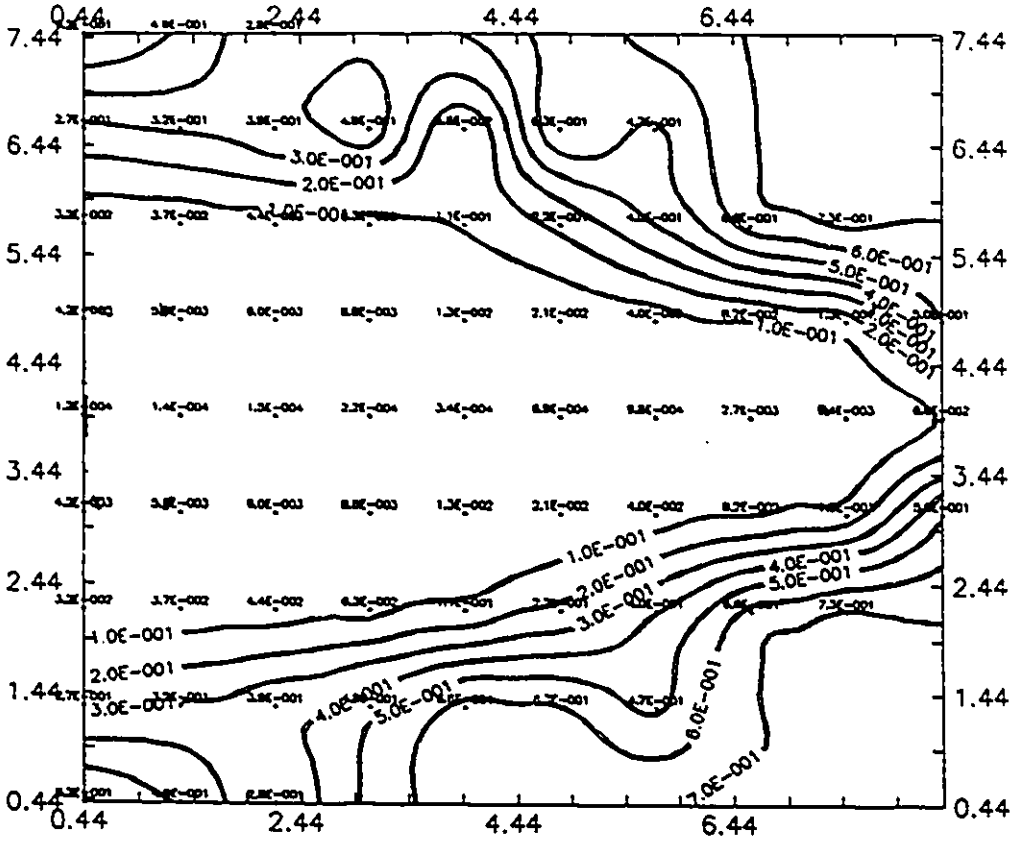

Fig. 8-35 A map of bainite distribution in the HAZ at the end of the welding. Post-weld heating: Coschell standard welding cycles.

APPENDICES

APPENDIX I

```
/*  ********************************************************
 * COMPUTER MODELLING MICROSTRUCTURE DEVELPOMENT          *
 *       IN RESISTANCE WEDLED CROSSED BARS                *
 *                SEPTEMBER, 1991                         *
 ********************************************************

#include <stdio.h>
#include <malloc.h>
#include <math.h>
#include <conio.h>
#include <graph.h>
#include <pgchart.h>
#include <time.h>
#include <stdlib.h>
#include <stddef.h>
typedef enum {FALSE, TRUE} boolean;
#define diam diain/39.37
#define second 60.

/************************************************/
/*          DECLARATION OF VABRIABLES           */
/************************************************/

main()
 {
   static float T[20][20][150], curr[10000]={0.};
   static float ms1[91]={0.},ms2[91]={0.},k[20][20];
   static float res[20][20],phi[20][20],Cp[20][20];
   static float xp[20][20],xb[20][20],G[20][20];
   static float xh[20][20]={0.}
   float R=1.987, tsum=0.0, rho=7854, alpha=17.7e-6;
   float Comp,Compb, Numer, curr_time,temp,joul=4.184;
   float diain, Ps, Bs, Ms, Ae3, Teut, delt, delx;
   float Xp,Xb,dX. d,D2,Fxc,dd,Xt[91],a,b,b1,b2,bs,Per;
   float Fo,qr,qhp,Qin, brack, c1, c2, c3, c4,c5,c6;
   int i, j, time,  numrow, numcol=18, totime=60, n=1, mm,
       step;
   int curr_index=0,length,flag,flag2, flagt;
   int cycle, cycle1, cycle2;
   char currs[81], day[9], month[9], year[9], name1[20];
        char steel[40], answer1[9], answer[5], name2[20];

   FILE *heat_in;
   FILE *Comp_steel;
   FILE *heat_transf_temp;
   FILE *heat_transf_nodes;
   FILE *heat_transf_pear;
   FILE *heat_transf_banit;
```

```
FILE *transf_pearf;
FILE *transf_banitf;
FILE *transf_tempf;

heat_in=fopen("heatchg6.dat","r+");
heat_transf_temp=fopen("heat_tmp.dat", "w+");
heat_transf_nodes=fopen("heat_nde.dat", "w+");
heat_transf_pear=fopen("heat_per.dat", "w+");
heat_transf_banit=fopen("heat_bnt.dat", "w+");
transf_pearf=fopen("last_per.dat", "w+");
transf_banitf=fopen("last_bnt.dat", "w+");
transf_tempf=fopen("last_tmp.dat", "w+");
Comp_steel=fopen("comp_stl.dat", "w+");

/*****************  **********************/
/***     Input initial Parameters     ***/
/*****************************************/

printf("\n\n      WELCOME TO COMPUTER PROGRAM OF\n"
 "MODELLING WELD MICROSTRUCTURE OF RESISTANCE
   WELDING\n\n");

printf("    Please enter Your Name!    ");
scanf ("%s%s", name1, name2);
printf("    Please enter the Month of today!    ");
scanf ("%s", month);
printf("    Please enter the Date of today!    ");
scanf ("%s", day);
printf("    Please enter the Year!    ");
scanf ("%s", year);

printf("\n Please enter the bar diameters in inches! ");
scanf ("%f", &diain);
printf("   The bar diameter in meter is:      %6.4f \n"
   " The number of nodes in the X direction is: %3i \n "
    "(X distance is the bar diameter)\n", diam, numcol);

numrow=numcol;
delx = diam/numcol;
delt = delx*delx/4.0/alpha;
length=1/delt;
printf("   The time increment is       %5.3f (seconds)\n"
"The calculation will be done in %2i(seconds)\n",
  delt,totime);

/*****************************************/
/***     Input steel composition     ***/
/*****************************************/

do
{
printf("\n   PLEASE ENTER THE STEEL NAME!    ");
```

```
    scanf( "      %s", steel);
    printf("\n      %%Carbon?    ");
    scanf( "      %f", &c1);
    printf("      %%Manganese? ");
    scanf( "      %f", &c2);
    printf("      %%Silicon?   ");
    scanf( "      %f", &c3);
    printf("      %%Nickel?    ");
    scanf( "      %f", &c4);
    printf("      %%Chromium?  ");
    scanf( "      %f", &c5);
    printf("      %%Molybdenum?");
    scanf( "      %f", &c6);

   printf("\nDo you want to change the input
     composition?\n"
          "Please enter YES or NO!        \n");
    scanf("%s", answer1);
    if( ! strcmp(answer1,"NO")){
    printf("\n***Please continue input parameters!!*** \n");
     };
     }
    while ( strcmp(answer1, "NO"));

    fprintf(Comp_steel,"Operator: %s  %s \n", name1, name2);
    fprintf(Comp_steel,"Running Date: %s  %s  %s \n", month,
            day, year);
    fprintf(Comp_steel,"Steel: %s\n%%C: %5.2f\n%%Mn:
      %5.2f\n%%Si: %5.2f\n" "%%Ni: %5.2f\n%%Cr: %5.2f\n%
      %Mo:%5.2f\n", steel,c1,c2,c3,c4,c5,c6);


/*************************************************************
/*                                                           */
/** Initial temperature distribution of surrounding bar     **/
/*                                                           */
/*************************************************************/

   for (j=0; j<110; j++) {
      for (i=0; i<19; i++) {
       T[i][0][j] = 293.0;
       T[18][i][j] = 293.0;
      }
   }

 /***      Initial nodes temperature distribution        ***/

     for (i=0; i<18; ++i) {
     printf("row[%2i]  ", i);
     for (j=1; j<19;++j){
     fscanf(heat_in,"%f",     &T[i][j][0]);
     if (j==11){
```

```
    printf("\n          ");
    }
    printf("%5.1f  ",   T[i][j][0]);
     }
     printf("\n");
     }

/***     Initial HAZ G.S# as temperature input      ***/

    for (i=0; i<9; ++i){
    printf("row[%2i]  ", i);
    for (j=9;j<19; ++j){
      temp=T[i][j][0];
      if (temp < 900)
         printf("      ");
      else if (temp>= 900 && temp <= 975){
         G[i][j]=14.3;
         printf("%6.1f", G[i][j]);
       }
      else{
         D2=2.247e7*exp(-28966/temp)+42.97*exp(-21892/temp);
         G[i][j]=log(0.06452/D2)/log(2.)+1;
         printf("%6.1f",     G[i][j]);
     };
    };
      printf("\n");
     };

/*************************************************/
/**           Input current functions           **/
/*************************************************/

printf("\n You will now enter a piecewise current
        function.\n"
          The function may last any length of time.
             It need not be continuous.\n"
  );
  do
  {
  printf("\nHow long for this section_(slope
          part)?(cycle1));
  scanf("%i", &cycle1);
  printf("\nHow long for this section_(flat part)?
          (cycle2)    ");
  scanf("%i", &cycle2);
  printf("\nEnter slope of current line!!   ");
  scanf(" %f",&a);
  printf("\nEnter y_axis intercept of current line_(sloping
                  part)!!");
  scanf(" %f",&b1);
  printf("Enter y_axis intercept of current
         line_(horizontal                part)!!   ");
```

```
 scanf(" %f",&b2);
 printf("\nDo you want to change the parameters?\n"
        "Please enter YES or NO!        \n");
 scanf("%s", answer);

if( ! strcmp(answer,"NO")){
 printf("\n** Calculation begins!! Please wait!! ** \n");
   };
 }

 while ( strcmp(answer, "NO"));
 cycle = cycle1+cycle2;
 bs=b1;
 b=b2;
 curr_time = cycle/(second*delt);
 for (i=0; i<n+curr_time; i++){
   if (a != 0) {
     curr[i]=a*(bs-b2)*second*delt/cycle1+b1;
     b1=curr[i];
     if (b1 <= b2){
        curr[i]=b2;
       }
     printf("curr[%4i]= %7.1f\n", i, curr[i]);
    }
   else{
     curr[i]=a*(i-n)+b;
     printf("curr[%4i]= %7.1f\n", i, curr[i]);
     }
    };
 fprintf(Comp_steel,"cycles: %4i\nslope: %3.1f\n
    post-current(Amp):%6.1f\n""post-current
    (slope part); %7.1f\n cycle1: %4i\n cycle2: %4i\n ",
    cycle, a, b, bs,cycle1, cycle2);

/*****************************************************/
/***    Transformation temperature calculation    ***/
/*****************************************************/

Comp=1.79+5.42*(c5+c6+4.0*c6*c4);
Numer=0.01*c5+0.52*c6;

Teut=995.8-13.89*c2+22.22*c3-14.44*c4+23.33*c5;
Ae3 =912.+273.-203.*sqrt(c1)-15.2*c4+44.7*c3
          +31.5*c6-30.0*c2-11.0*c5;
Bs =656.+273.-58.*c1-35.*c2-75.*c3-15.*c4-34.*c5-41.*c6;
Ms =561.+273.-474.*c1-33.*c2-17.*c4-17.*c5-21.*c6;

printf("\nThe transformation temperature of the steel bar
          are:     (K)\n"

   "   Ae3         Ps          Bs         Ms  \n"
   "  %5.1f       %5.1f       %5.1f      %5.1f\n",
```

```
        Ae3,      Teut,      Bs,       Ms);

 fprintf(Comp_steel,"\nThe transformation temperature of
       the steel bar are: (K)\n"
  "  Ae3         Ps        Bs         Ms  \n"
  " %5.1f        %5.1f      %5.1f      %5.1f\n",
     Ae3,        Teut,      Bs,         Ms);

    for (i=0; i<9; ++i){
       for (j=9; j<19;++j){
         xp[i][j]=1.e-12;
         xb[i][j]=1.e-12;
         printf("%7.1e", xp[i][j]);
      };
    };

 /************************************************/
 /**          Heat transfer calculation          **/
 /************************************************/

printf("\n The selected nodes temperature distribution \n");
   fprintf(heat_transf_banit,"Sec, [1'9],[2'12],[2'16],
   [3'12],[3'16],[4'12],[4'16],[5'18],[1'18]\n");
   fprintf(heat_transf_pear,"Sec,  [1'9],[2'12],[2'16],
              [3'12],[3'16],[4'12],[4'16],[5'18],[1'18]\n");
   fprintf(heat_transf_nodes,"Sec, [1'9],[2'12],[2'16],
              [3'12],[3'16],[4'12],[4'16],[5'18],[1'18]\n");

   for( step=0; step<60; ++step){
     for(time=1; time<length+1; ++time){
       curr_index +=1;
       flag=0;
       flag2=0;
       for(i=0;     i < numrow; ++i){
      for(j=1; j <numcol+1; ++j){
      temp=T[i][j][time-1];

  /*** Calculation Cp, resistivity, and conductivity ***/

  if (temp < 1000)
      Cp[i][j]=1.117e6/pow((1010-temp),2)+12622/(1010-temp)
                  +0.3485*temp+355.6;
  else

     Cp[i][j]=1.225e8/pow((temp-990),4)+0.1381*temp+585.7;

  if (temp > 973)
      k[i][j] = 27.83;
  else
      k[i][j] = 52.-0.031*temp;
```

```
  if (temp <= 473)
     phi[i][j]=7.13e-4*temp-3.07e-2;
  else if(temp>=1073)
     phi[i][j]=2.31e-4*temp+8.9e-1;
  else
     phi[i][j]=1.35e-3*temp-3.71e-1;
     phi[i][j]=phi[i][j]*1.e-6;

  res[i][j]=phi[i][j]*delx/(delx*diam);

  /*********************************************/
  /***      Finite difference heat transfer   ***/
  /*********************************************/

    alpha=k[i][j]/rho/Cp[i][j];
    Fo=alpha*delt/(delx*delx);
    qr=pow(curr[curr_index]/18, 2)*res[i][j];
    if (j < 10 ){
        qr=0.0;
        qhp=0.0;
    };
    if (ms1[flag]==0. && xh[i][j]>0.0){
       qhp=20.0*joul*rho*delx*delx*diam;
       qhp=qhp*xh[i][j];
    };
    Qin=(qr+qhp)*delt/(rho*delx*delx*diam*Cp[i][j]);

    if (i==0 && j==numcol) {
        brack=T[i+1][j][time-1]+T[i][j-1][time-1];
        T[i][j][time]=Fo*brack+(1-2*Fo)*T[i][j][time-1]+Qin;
    }
    else if (i==0 && j<numcol){

brack=T[i][j-1][time-1]+T[i][j+1][time-1]+T[i+1][j][time-1];
    T[i][j][time]=Fo*brack+(1-3*Fo)*T[i][j][time-1]+Qin;
    }
   else if (i<numrow && j==numcol) {

brack=T[i-1][j][time-1]+T[i+1][j][time-1]+T[i][j-1][time-1];
   T[i][j][time]=Fo*brack+(1-3*Fo)*T[i][j][time-1]+Qin;
   }
   else {

brack=T[i-1][j][time-1]+T[i+1][j][time-1]+T[i][j-1][time-1];
   brack=brack+T[i][j+1][time-1];
   T[i][j][time]=Fo*brack+(1-4*Fo)*T[i][j][time-1]+Qin;
   }

 /*********************************************/
 /***      Perlite formation calculation    ***/
 /*********************************************/
```

```
temp=T[i][j][time];
if (i <=8 && j>=9){
   flag +=1;
   flag2+=1;
if (temp <= Teut && temp >= Bs ){
  if (ms1[flag]==0.){
      Xp=xp[i][j];
   d=1.0/exp(-27500.0/R/temp)+ Numer/exp(-37000.0/R/temp);
   dX =pow(2.0, (G[i][j] - 1.0)/2.0)*pow((Teut-temp),
            3.0)*0.01/Comp/d;
   dX =dX*pow(Xp, 0.59*(1.0-Xp))*pow((1.0-Xp), 0.77*Xp);
   if (temp <= Bs){
   dX=0.0;
   ms1[flag]=1.0;
  }
  xh[i][j]=dX;
  Xp +=dX;
  xp[i][j]=Xp;
  if (Xp >= 0.999){
    dX=0.;
    ms1[flag]=1.0;
   }
  }
}

/*********************************************/
/***     Banite formation calculation      ***/
/*********************************************/

if (temp < Bs && temp >= Ms ){
   if ( ms2[flag2]==0.){
      Xb=xb[i][j];
      dd=exp(-27500.0/R/temp);
      Compb=(2.34+10.1*c1+3.8*c5+19.*c6)*1.e-4;

 Fxc=exp(Xb*Xb*(1.9*c1+2.5*c2+0.9*c4+1.7*c5+4.*c6-2.6));
   dX =pow(2.0, (G[i][j] - 1.0)/2.0)*pow((Bs-temp),
            2.0)*dd*delt/Compb/Fxc;
   dX =dX*pow(Xb, 0.59*(1.0-Xb))*pow((1.0-Xb), 0.77*Xb);
      if (temp < Ms){
         dX=0.;
         ms2[flag2]=1.0;
      }
      Xb +=dX;
      Per = xp[i][j];
      xb[i][j]=Xb;
      if (xb[i][j]+Per>=0.9999 ){
      dX=0.;
      ms2[flag2]=1.0;
      }
      flagt=flag=flag2;
       }
```

```
        }
       }
      };
/***-----------        loop j finished   -----------***/
    };
/***-----------    loop i finished  -------------***/

   mm=time;
   printf(" step; %i time: %i,T[time+1]: %5.1f\n", step, mm,
                T[0][18][time]);
    };
/***-----------    loop time finished     --------------***/

   fprintf(heat_transf_temp,"Temperature distribution after
     %i seconds\n", step);
     for(i=0; i<18; ++i){
     printf("row[%2i]:  ", i);
     fprintf(heat_transf_temp,"row[%2i]:  ", i);
     for (j=1; j<19; ++j){
        T[i][j][0]=T[i][j][mm];
        T[i][j][step]=T[i][j][mm];
        if(j==11){
           printf("\n          ");
           fprintf(heat_transf_temp, "\n          ");
        }
     printf("%5.1f  " , T[i][j][0]);
     fprintf(heat_transf_temp,"%5.1f  " , T[i][j][0]);
     }
     printf("\n");
     fprintf(heat_transf_temp, " \n");
     }

     fprintf(heat_transf_nodes, "%2i, %5.1f,  %5.1f,  %5.1f,
        %5.1f,"" %5.1f, %5.1f, %5.1f, %5.1f, %5.1f\n", step,
  T[0][9][step],[1][12][step],T[1][16][step],T[2][12][step],
  T[2][16][step],T[3][12][step],T[3][16][step],
  T[4][18][step], T[0][18][step]);

   fprintf(heat_transf_pear,"%3i, %7.3e, %7.3e, %7.3e,
    %7.3e, %7.3e, %7.3e," " %7.3e, %7.3e, %8.3e\n",
    step, xp[0][9], xp[1][12],xp[1][16],xp[2][12],
    xp[2][16], xp[3][12],xp[3][16],xp[4][18],xp[0][18]);

    fprintf(heat_transf_banit,"%3i, %7.3e, %7.3e, %7.3e,
      %7.3e, %7.3e, %7.3e,"" %7.3e, %7.3e, %8.3e\n", step,
      xb[0][9], xb[1][12],xb[1][16],xb[2][12],xb[2][16],
      xb[3][12],xb[3][16],xb[4][18],xb[0][18]);
    };

  /***------      loop step finished      --------***/

   fprintf(transf_pearf,"   The final pearlite of austenite
```

```
        decomposition fraction in selected nodes\n"
         "   col-9, col-10, col-11, col-12, col-13, col-14,
             col-15,col-16, col-17, col-18\n");

  fprintf(transf_banitf,"  The final banite of austenite
        decomposition fraction in selected nodes\n"
        "    col-9, col-10,col-11,col-12,col-13,col-14,
             col-15,col-16,col-17,col-18\n");

  for (i=0; i<10; ++i){
    fprintf(transf_pearf,"row%2i: ", i);
    fprintf(transf_banitf,"row%2i: ", i);
    for(j=9; j<19; ++j){
    fprintf(transf_pearf, "%7.3e, ", xp[i][j]);
    fprintf(transf_banitf,"%7.3e, ", xb[i][j]);
    fprintf(transf_tempf, "%6.1f,  ",T[i][j][0]);
    }
    fprintf(transf_pearf, "   \n");
    fprintf(transf_banitf,"   \n");
    fprintf(transf_tempf,"   \n");
    }

/***---------- Main program finished!!----------***/

     printf("\n  ***     The program is finished!!    ***\n"
        "       ***    Thank you enjoy it!!   ***\n ");
 }
```

APPENDIX II

```
/*************************************************************/
/*  MODIFIED KINETIC ALGORITHM FOR CALCULATION ISOTHERMAL */
/*   TRANSFORMATION FOR HIGH CARBON PLAIN CARBON STEEL    */
/*                    SEPTEMBER, 1991                      */
/*************************************************************

    #include <stdio.h>
    #include <conio.h>
    #include <string.h>
    #include <math.h>
    #include <graph.h>
    #include <pgchart.h>
    #include <time.h>
    #include <stdlib.h>
    #include <stddef.h>
    typedef enum {FALSE, TRUE} boolean;

    main()
    {
     float temp, c1, c2, c3, c4, c5, c6, G;
     double dX, dXf1, dXf, Numer, diff, dif1, bct,Temp;
     double Xp=1.e-12, Xf=1.e-12, d, R=1.9878, aa;
     float dNOM, TeutF, Ps ,Bs, Ms, Teut, Comp, dFT;
     float Ae3, Feq1,expnt1,expnt2;
     int J=0, nn=0, i, count1=1,count50=1,countf=1;
     int mode=_VRES16COLOR;
     char steel[50],answer1[9],year[9],month[10];
     char day[15],name1[15],name2[15];
     float  xvalue[450], Xfvalue[450];
     float  yvalue[450];
     FILE *in;
     FILE *ct1;
     FILE *ct5;
     FILE *ctf;
     in = fopen ("isthrmp2.dat", "w+");
     ct1= fopen ("cct1%.dat","w+");
     ct5= fopen ("cct50%.dat","w+");
     ctf= fopen ("cctf%.dat","w+");

  /*******************************************/
  /*       INPUT STEEL COMPOSITION           */
  /* *****************************************/

  printf("***THIS A PROGRAM TO CALCULATION
          ISOTHERMAL TRANSFORMATION!!***\n"
           "\n PLEASE PRESS BAR TO BEGIN THE PROGRAM!!\n");
  printf("    Please enter Your Name!    ");
  scanf ("%s%s", name1, name2);
```

```
printf("    Please enter the Month of today!    ");
scanf ("%s", month);
printf("    Please enter the Date of today!    ");
scanf ("%s", day);
printf("    Please enter the Year!    ");
scanf ("%s", year);
fprintf(in,"Operator: %s  %s   \n", name1, name2);
fprintf(in,"Program Running Date: %s %s %s \n",
            month, day, year);

do
{
printf("   PLEASE ENTER THE STEEL NAME!    ");
scanf( "%s", steel);
printf("\n      %%Carbon?    ");
scanf( "      %f", &c1);
printf("      %%Manganese? ");
scanf( "      %f", &c2);
printf("      %%Silicon?   ");
scanf( "      %f", &c3);
printf("      %%Nickel?    ");
scanf( "      %f", &c4);
printf("      %%Chromium?  ");
scanf( "      %f", &c5);
printf("      %%Molybdenum?");
scanf( "      %f", &c6);
printf("      PLEASE ENTER ASTM GRAIN SIZE NUMBER:  ");
scanf ("      %f", &G);
printf(" Please enter the exponent used in first part:");
scanf("     %f", &expnt1);
printf(" Please enter the exponent used in second part:");
scanf("       %f", &expnt2);
printf("\nDo you want to change che input
  composition parameters?\n""Please enter YES or NO! \n");
scanf("%s", answer1);
if( ! strcmp(answer1,"NO")){
printf("\n*** Please continue input parameters!! *** \n");
};
}
while ( strcmp(answer1, "NO"));
fprintf(in,"Exponent in first part:%5.2f\nExponent in
       second       part:%5.2f\n", expnt1, expnt2);
fprintf(in, "Steel calculated is:%s\n", steel);

fprintf(in,"C:%8.2f\nMn:%7.2f\nSi:%7.2f\nNi:%7.2f\n
         Cr:%7.2f\n" "Mo:%7.2f\n GS:%7.2f\n",
         c1,c2,c3,c4,c5,c6,G);

printf ("\n FERITE AND PERLITE FORMATION CALCULATION!\n");

Comp = 1.79+5.42*(c5+c6+4.0*c6*c4);
Numer=0.01*c5+0.52*c6;
```

```
 Feql=(0.77-c1)/(0.77-0.0218);
 Teut=995.8-13.98*c2+22.22*c3-14.44*c4+23.33*c5;
 Ae3 =912.+273.-203.*sqrt(c1)-15.2*c4+44.7*c3
           +31.5*c6-30.0*c2-11.0*c5;
  Bs =656.+273.-58.*c1-35.*c2-75.*c3-15.*c4-34.*c5-41.*c6;
 Ms =561.+273.-474.*c1-33.*c2-17.*c4-17.*c5-21.*c6;
 TeutF= (Teut-273.15)*9./5.+32.0;
 dNOM=59.6*c2+1.45*c4+67.7*c5+244.*c6;
 printf("\nThe transformation temperature of the steel bar
         are: (K)\n"
" Ae3         Ps       Bs       Ms         Feql\n"
" %5.1f     %5.1f     %5.1f    %5.1f     %5.1f\n",
      Ae3, Teut,     Bs,      Ms, F      eql);
 fprintf(in,"\nThe transformation temperature of
              the steel bar are: (K)\n"
    "   Ae3         Ps     Bs      Ms     Feql\n"
    "  %5.1f      %5.1f    %5.1f  %5.1f    %5.1f\n",
      Ae3, Teut,  Bs, Ms, Feql);
 printf("\n       ** Begin to calculate!!**\n\n ");
 printf("     'aa'            'Xp'          'Xf'\n ");
 fprintf(ct1," Temp(c) ,     'aa',         'Xp'\n ");
 fprintf(ct5," Temp(c),      'aa',         'Xp'\n ");
 fprintf(ctf," Temp(c),      'aa',         'Xp'\n ");

/*********************************************/
/***       Calculation  IT curve            ***/
/*********************************************/

 for ( Temp=Teut-10; Temp>=Bs-110; Temp -=25.){
 printf("Temp=%f\n",Temp);
 diff=exp(-37000.0/1.9878/Temp);
 dif1=exp(-27500.0/R/Temp);
 d=1.0/dif1+Numer/diff;
 dFT =Ae3-Temp;
 bct =exp(-23500.0/R/Temp);
 for (aa=0.01; aa<=10000.;   aa += 0.01)
   {
   if (Xp < 0.01 && Xf < Feql)
   {
  dXf1=pow(2.0,(G-1.0)/2.0)*pow(dFT, 3.0)*bct*0.01/dNOM;
  dXf=dXf1*pow(Xf,(2.0*(1.0-Xf))/3.0)*pow(1.0-Xf,
       2.0*Xf/3.0);
  Xf=Xf+dXf;
  };
  dX=pow(2.0,(G-1.0)/2.0)*pow((Teut-Temp),3.0)*0.01/Comp/d;
  dX =dX*pow(Xp, expnt1*(1.0-Xp))*pow((1.0-Xp), expnt2*Xp);
  Xp =Xp+dX;
  J++;
  if ( J == 25 ){
     ++nn;
  fprintf(in,"  %f  %f  %f  %f \n", aa, Xp, Xf, Temp-273);
  printf(   %f     %e     %e      %i \n", aa, Xp, Xf,nn);
```

```
J = 0;
};
if (Xp>=0.01 && count1 >0 ) {
printf("Temp:  %f,  aa:%f,  Xp: %f\n", Temp-273, aa, Xp);
fprintf(ct1,"  %f,     %f,       %f\n", Temp-273, aa, Xp);
count1=0;
}
if (Xp>=0.50 && count50 >0){
printf("Temp: %f,  aa:%f,  Xp:  %f\n", Temp-273, aa, Xp);
fprintf(ct5,"  %f,    %f,       %f\n", Temp-273, aa, Xp);
count50=0;
}
if((Xf+Xp) >= 9.9997e-1 && countf >0 ){
printf("Temp:  %f,  aa:%f,  Xp: %f\n", Temp-273, aa, Xp);
fprintf(ctf,"  %f,     %f,       %f\n", Temp-273, aa, Xp);
countf=0;
break;
}
};
Xp=Xf=1.e-12;
count1=count50=countf=nn=1;
}
```

APPENDIX III

```
*************************************************
*       STANDARD DEVIATION CALCULATION          *
*************************************************


      REAL X,YC,A,B, YHAT,SYSQ,SYS,YDSQ, YE
      INTEGER I,J,M,N
      PARAMETER (N=13)
      DIMENSION YE(20),YC(20)
*
      DATA (YE(J),J=1,N)/26.70,34.02, 48.12, 39.09, 68.05,
     C          89.81,65.74, 83.79, 114.46, 106.80, 136.12,
     C           179.61,127./
*
      PRINT*,'PLEASE INPUT THE CALCULATION DATA!'
      READ *, (YC(J), J=1,N)

      SYSQ=0.
      PRINT*,'THE INPUT OF EXPERIMENT DATA IS:'
      DO 5 M=1,N
 5      WRITE(6,10) YC(M),YE(M)
 10     FORMAT(4X,'YC=', F8.2, 7X, 'YE=', F8.2)
*
*     CALCULATING THE STANDARD ERROR OF ESTIMATE
*


       DO 200 J=1,N
         YDSQ=(YC(J)-YE(J))**2
        SYSQ=SYSQ+YDSQ
         PRINT 30, J,'(YC-YE)**2):', YDSQ
 30     FORMAT(4X,I2,':', A, 2X,F10.4)
 200 CONTINUE
*
      SSS=SYSQ/(N-2.0)
      SYS=SQRT(SSS)
*
      PRINT*,'                                    '
      PRINT*,'                                    '

     PRINT 35,'THE RESULT OF THE STANDARD ERROR OF ESTIMATE
```

```
C              IS:'
35  FORMAT(1X,A/1X,54('=')/)
    WRITE(6,40) SYSQ, SYS
40  FORMAT(1X,'SYSQ=Σ(YC(J)-YE(J))**2=',F9.4,4X,'SYS=',F10.6)
*
    STOP
    END
```

APPENDIX IV

```
************************************************************
*     GRAIN SIZE, GRAIN SIZE NUMBER VS TIME, TEMPERATURES
*     CALCULATTED USING EMPIRICAL GRAIN GROWTH EQUATION
************************************************************

      REAL GS,T,A,B,C,D2,TIME,D
      INTEGER I,J, L,M

      D2(T)=2.2471e7*EXP(-28966/T)+42.97*exp(-21897/T)*TIME
      OPEN(UNIT=13, FILE='GSdos.DAT',STATUS='NEW')

      L=0
      TIME=1
      T=1650.
      WRITE(13,10) 'T(K)', 'G.S.(μm)', 'G.S.#'
10    FORMAT(2X, 3(A, 8X))

      DO 20 I=1,34
          L=L+1
          GS=LOG(0.06452/D2(T))/LOG(2.)+1
          D=SQRT(D2(T))*1.E3
          WRITE(13,15) T,',', D,',',GS
15        FORMAT(1X, F6.1,A,5X,F8.2,A,5X,F7.3)
          PRINT 17,'T=',T, 'time=',TIME, 'D(μm)=',D, 'GS#=',GS
17        FORMAT(1X, 2(A, F6.1, 4X), A,F8.2,4x, A, F6.3)
          T=T-10
20    CONTINUE

      STOP
      END
```

VITA AUCTORIS

The author was born
in Bejiing, China on Aug. 1957.
She received her Bachelor of Science
in Engineering Materials from East China
University of Chemical Technology, Shanghai,
China, in 1982. After working more than seven years
as a material engineer in Shanghai Research Institute of
Building Sciences, China, she then started her Master's
in Engineering Materials program, Department of
Mechanical Engineering at the University
of Windsor, Canada, in 1989. She
received her M.A.Sc. degree
in Engineering Materials
in Fall, 1991.